Optical Pulse Shaping For Chirped Pulse Interferometry And Bio-Imaging

by

Kurt Schreiter

A thesis
presented to the University of Waterloo
in fulfillment of the
thesis requirement for the degree of
Master of Science
in
Physics

Waterloo, Ontario, Canada, 2011

I hereby declare that I am the sole author of this thesis. This is a true copy of the thesis, including any required final revisions, as accepted by my examiners.

I understand that my thesis may be made electronically available to the public.

Abstract

Biomedical imaging requires high resolution to see the fine features of a sample and fast acquisition to observe live cells that move. Optical coherence tomography (OCT) is a powerful technique which uses optical interference for non-invasive high resolution 3D imaging in biological samples.

The resolution of OCT is determined by the length over which the light used will interfere. Unfortunately, dispersion hurts the imaging resolution by broadening interference features. A technique called quantum-OCT (QOCT)[1] is immune to dispersion but requires entangled photon pairs. The need for entanglement drastically reduces the number of photons available for imaging, making QOCT too slow to be practical. Chirped-pulse interferometry (CPI) is also immune to dispersion. A chirped pulse is one where the frequency, or colour, of the light changes from red to blue from one end of the pulse to the other. CPI relies on frequency correlations created by applying different chirps to two separate pulses. This method had the disadvantage of being limited to a single predetermined chirp rate, and discarded 50% of the power. However CPI has better resolution than OCT, automatic dispersion cancellation, and 10,000,000 times the signal strength of QOCT [13].

A new, much more flexible and efficient method of CPI will be demonstrated by creating the frequency correlations entirely in a single pulse. This new method is referred to as non-linear chirped pulse interferometry (NL-CPI).

The non-linear chirp required in NCPI is very difficult to produce using only conventional optics. In this thesis we document the construction and characterization of a new method of creating the desired chirp using a programmable pulse-shaper (PS). We build a PPS and then demonstrated its functionality by compressing a $105nm$ FWHM bandwidth pulse to under $17fs$, near its transform limited time duration. We also show that the values given to the PPS for dispersion are accurate by calculating and then compensating the dispersion caused by various optical elements in the CPI interferometer.

Conventional OCT systems are immune to dispersion common to both arms of the interferometer. Non-linear interferometers experience broadening due to this dispersion, making them more difficult to use with fibre based interferometers common in conventional OCT. We show that NL-CPI can compensate for dispersion common to both arms of the interferometer, making NL-CPI more appealing as a replacement for conventional OCT.

In this thesis we experimentally implement and demonstrate a prototype setup using non-linear CPI for dispersion-cancelled imaging of a mirror, with a resolution comparable to conventional OCT systems. We then use the system to produce 2-D cross sectional images of a biological sample, an onion. Q-OCT has previously been used to image an onion[16], but required treating the onion with gold nano particles to achieve a useful signal. The onion we used had no special treatment. In addition our axial scanning rate is also 10000 times faster than Q-OCT.

Acknowledgements

I would like to thank my supervisor Kevin Resch for providing me with the opportunity to perform the research covered in this thesis, and for funding me while I completed this thesis. I would also like to thank my advisory committee members, Kostadinka Bizheva, and Michel Gingras, for their guidance and helpful discussions. I thank Donna Strickland for agreeing to be on my examining committee. I would like to thank my entire examining comittee Kevin, Kostadinka, and Donna, for their patience and understanding.

I thank the members of my research group Deny Hamel, Devon Biggerstaff, Jonathan Lavoie , Kent Fischer, Krister Shalm and Mike Mazurek for their friendship as well as helpful discussions and feedback. I would particularly like to thank Rainer Kaltenbaek and Robert Prevedel for their friendship, patience and help in all areas of this project.

Robert Hill gave me my first opportunity to do research, and provided a role model to aspire to. James Forrest encouraged me to pursue graduate studies and I will forever appreciate that. Frank Wilhelm-Mauch encouraged me when I was ready to give up, and helped me to keep things in perspective. I would not have made it this far without him.

I would like to acknowledge the Ontario Graduate Scholarship for funding the first year of my research.

Last I would like to thank my family, particularly my sister Krista and brother Devan for encouraging me to return to school and finish my bachelor degree.

Dedication

This thesis is dedicated to my wife Meredith and my sons Jack and Samuel. Your love and support have guided me through the most difficult period in my life. I love and thank all three of you. I would also like to dedicate this thesis to my dog Anna who stayed by my side or waited up for me on countless late nights working on this thesis.

Contents

List of Tables

List of Figures

Chapter 1

Introduction

Optical 3-D imaging of biological samples at is a challenge with many possible methods, each with it's strengths and weaknesses[7]. In this thesis we will discuss a method of high resolution biological imaging with potential advantages compared to one of the best methods currently in use,Optical coherence tomography (OCT).

OCT is a powerful technique which uses interference for non-invasive high resolution 3D imaging in biological samples. The resolution of OCT is determined by the coherence length of the light source used, that is the length over which the light used will interfere[23, pg. 409]. Unfortunately OCT image resolution (details/unit length) is negatively effected by dispersion, the frequency dependent velocity of light. Dispersion hurts the imaging resolution by broadening interference features and lowering interference contrast. Dispersion is caused by the light travelling through a medium, such as the material the biological sample is made of, optics used in the system, or cover glass over the sample. Because of this it is difficult to avoid dispersion. Dispersion increases as the bandwidth of the light increases, so high resolution OCT systems are even more sensitive to dispersion. An example OCT system[22] has a bandwidth of $135nm$ centred at $792nm$. The system is capable of resolving details as small as $2\mu m$ (resolution $=.5details/\mu m$). By simply adding only 7mm of BK7 glass (a common optical glass) in front of the sample the system will only be able to resolve details of $20\mu m$ (resolution $=.05details/\mu m$)! And as the bandwidth increase the resolution increases linearly, but the dispersion effect increases quadratically, so it only makes the problem worse. If the bandwidth is doubled, the resolution without glass improves to $1details/\mu m$, but with the 7mm of glass the resolution is now $0.025details/\mu m$, even worse than before!

A technique called quantum-OCT (QOCT)[1] is immune to second order dispersion. This is the dispersion order primarily responsible for decreasing regular OCT resolution. QOCT requires the strong frequency correlations present in entangled photon pairs. Entanglement is a property of quantum mechanical systems involving two or more particles that cannot be described separately. The need for entanglement drastically reduces the number of photons available for imaging, making QOCT too slow to be practical.

Chirped-pulse interferometry (CPI) is also immune to dispersion[11, 13]. A pulse is a short burst of laser light, lasting as little as a few femtoseconds. A chirped pulse is one where the frequency, or colour, of the light changes from red to blue from one end of the pulse to the other. CPI has automatic dispersion cancellation, and much higher signal strength than QOCT[13].

CPI has been demonstrated in the lab, but with insufficient resolution and power levels too high to use with living samples. The previous work on CPI used pairs of oppositely linear chirped pulses, combining them at a beam splitter to produce the required frequency correlations. This method had the disadvantage of being limited to a single predetermined chirp rate, and discarded 50% of the power. A new, much more flexible and efficient method will be demonstrated by creating the frequency correlations entirely in a single pulse. This new method is referred to as non-linear chirped pulse interferometry (NL-CPI).

The non-linear chirp required in NL-CPI is very difficult to produce using only conventional optics. In this thesis we document the construction and characterization of a new method of creating the desired chirp using a programmable pulse shaper (PPS). We build a PPS and then demonstrated its functionality by compressing a 106nm FWHM bandwidth pulse to under $17fs$, near its transform limited time duration. We also show that the values given to the PPS for dispersion are accurate by calculating and then compensating the dispersion caused by various optical elements in the CPI interferometer.

In this thesis we experimentally implement and demonstrate a prototype setup using non-linear CPI for dispersion-cancelled imaging of a mirror, with a resolution comparable to conventional OCT systems. We then use the system to produce 2-D cross sectional images of a biological sample, an onion. Q-OCT has previously been used to image an onion[16], but required treating the onion with gold nano particles to achieve a useful signal. The onion we used required no special treatment.

Chapter 2

Background

This chapter will discuss some of the relevant topics related to Chirped Pulse Interferometry (CPI). First we will discuss laser pulses and an effect of propagating these pulses through a dielectric material, known as dispersion. The signal recorded in a CPI experiment is produced by a non-linear optical effect, sum frequency generation (SFG). We will discuss this as well as one of the experimental constraints on creating SFG, phase matching.

The last few sections will discuss the two comparable imaging techniques. Optical Coherence Tomography (OCT) is the imaging technique that CPI may be able to enhance/replace. Quantum OCT is a technique with significant advantages over OCT that CPI attempts to emulate, but has critical shortcomings that CPI also alleviates.

Many of the theoretical models will make use of Gaussian functions so a few properties of these functions are presented in Appendix A.

2.1 Pulse Characteristics

2.1.1 Introduction

Often when we think of lasers we conjure images of continuous beams of light stretching from source to infinity (or a beam block, whichever comes first). However lasers can also produce packets containing many photons but lasting tiny fractions of a second. We call these packets "pulses. Many of the following experiment in this thesis involve the use of ultra-fast laser pulses. As an example of what ultra-fast means,our temporal pulse full width at half maximum (FWHM) has been recorded as short as 17fs ($fs = 10^{-15}s$).

2.1.2 Pulse Shape

We can speak about the"shape of a pulse when we refer to the amplitude envelope of the pulse in a graph of the electric field vs time or frequency . This envelope is the area enclosed by a curve joining all of the maxima of the pulse and a curve joining all of the minima. The instantaneous frequency of the pulse will not necessarily be constant in time or space. With the exception of vacuum, light of different frequencies travel at different velocities. This means that even if the pulse starts out with all of the frequencies in phase, they will soon develop relative phases to each other, potentially causing the shape of the pulse to change.

2.1.3 Mathematical Representation of the Electric Field

The following derivation is based on the [27, pg. 11-23] primarily and also on the derivation in [6, pg. 1-12].

An optical pulse can be described by its electric field in either time or frequency domain[6, pg. 1]. The Electric field is a 4 Dimensional Complex Vector $\vec{E}(x, y, z, t)$, but for our purposes we will only look at the time dependence using the 'scalar approximation'[27, pg. 11]. The Pulse envelop is described by an amplitude function $\sqrt{I}$ which can be almost anything, but in this section we will use a Gaussian. $I \propto |E|^2$ is the intensity commonly measured instead of the electric field. The time and frequency dependency of the pulse are described by a complex exponential so that the complete time domain electric field is written[27, pg. 11]:

$$\mathcal{E}(t) = \frac{1}{2}\sqrt{I(t)}e^{-i\omega_0 t}e^{-i\{(\omega-\omega_0)t+\phi(t)\}} + c.c. \tag{2.1}$$

Where the term inside the root is the temporal intensity and the exponential term is the phase. The complex phase is broken down into a term with a real carrier *angular* frequency ω_0, and a real time dependant phase $\phi(t)$. *c.c* refers to the complex conjugate, which will from here forward be neglected using the "analytic signal approximation"[27, pg. 12]. The field can then be written in terms of its complex amplitude[27, pg. 12]:

$$E(t) = \sqrt{I(t)}e^{-i\{\phi(t)\}} \tag{2.2}$$

Note that we also use the "slow varying signal approximation"[6, pg. 5][27, pg. 45] to drop the fast oscillating carrier frequency ω_0.

The spectral domain description $\tilde{E}(\omega)$ of the pulse can be found by taking the Fourier transform of the complex amplitude[27, pg. 13]

$$\tilde{E}(\omega) = \mathcal{F}(E(t)) = \int_{-\infty}^{\infty} E(t)e^{-i\omega t}dt \tag{2.3}$$

rewriting in terms of the spectral intensity $S(\omega)$ and spectral phase $e^{-i\phi(\omega)}$

$$\tilde{E}(\omega) = \sqrt{S(\omega)}e^{-i\phi(\omega)}, \tag{2.4}$$

$S(\omega)$ represents the signal that can be measured with a spectrometer.

2.1.4 Transform Limited Pulses

For the simulations in this thesis the time domain electric field is found by taking the inverse Fourier transform of $S(\omega)$ and assuming the phase is zero for all frequencies:

$$E(t) = \mathcal{F}^{-1}(S(\omega)) \tag{2.5}$$

The resulting electric field represents the shortest possible pulse for the given spectrum and is refereed to as the transform limited pulse [24, pg. 335]. The pulse in this form can be thought of as trying to approximate a delta function in time using a Fourier cosine series over a finite bandwidth of frequencies. Thus, the larger the spectral bandwidth, the better the approximation and the shorter the pulse can be.

2.1.5 Instantaneous Frequency

We can rewrite the true frequency in terms of the offset from the carrier frequency ω_0.

$$E(w) = \sqrt{S(\omega - \omega_0)}e^{-i\phi(\omega-\omega_0)} \tag{2.6}$$

Then the instantaneous frequency of the field can be written[27, pg. 12]:

$$\omega_{inst} = \omega_0 - \frac{d\phi}{dt} \tag{2.7}$$

2.2 Dispersion

When a laser pulse travels through a dielectric medium, the different frequency components of the pulse travel at different velocities. The result is that the different frequencies develop relative phase between each other. This effect is known as "dispersion". Dispersion can cause the temporal width of the pulse to change. It will be shown later that dispersion causes the signal from an optical coherence tomography system to broaden, hurting the performance of the system.

The spectral phase $\phi(\omega)$ can be expanded expanded as a Taylor series around the carrier frequency[27, pg. 17]:

$$\phi(\omega) = \phi_0 + (\omega - \omega_0)\frac{d\phi(\omega)}{d\omega} + \frac{(\omega - \omega_0)^2}{2}\frac{d^2\phi(\omega)}{d\omega^2} + \frac{(\omega - \omega_0)^3}{6}\frac{d^3\phi(\omega)}{d\omega^3} + ... \tag{2.8}$$

2.2.1 Group Delay

In the same way that we defined the instantaneous frequency in the time domain in the last section, we can define the group delay in the spectral domain[27, pg. 16]:

$$t_{group} = \frac{d\phi}{d\omega} \tag{2.9}$$

t_{group} tell us at what time in the pulse reference frame a particular frequency occurs[27, pg. 16]. We will use plots of group delay later to visualize the frequency correlations that the following experiments use.

2.2.2 Second and Third Order Dispersion

The next term in the Taylor series is the Group Delay Dispersion (GDD), from here on referred to as 2^{nd} Order Dispersion (D_2) [18]:

$$D_2 = \frac{1}{2}\frac{d^2\phi}{d\omega^2} \tag{2.10}$$

2^{nd} Order Dispersion causes relative phases to develop between the various frequencies in the pulse, causing the pulse duration to change. D_2 is positive in most optical materials. We refer to a TL pulse that has passed though a material with positive D_2 as having been "chirped". A pulse experiencing negative D_2 is referred to as "anti-chirped"[6, pg. 5].

Similarly D_3 refers to 3^{rd} order dispersion, the next term in the series:

$$D_3 = \frac{1}{6}\frac{d^3\phi}{d\omega^3} \tag{2.11}$$

The dispersion caused by propagating though a material is referred to as chromatic dispersion and is found though Taylor expansion of the wave number k [18][6, pg. 31-32][14, pg. 337]:

$$k = \frac{n(\omega)\omega}{c} \tag{2.12}$$

$$k(\omega) = k_0 + (\omega - \omega_0)\frac{dk(\omega)}{d\omega} + \frac{(\omega - \omega_0)^2}{2}\frac{d^2k(\omega)}{d\omega^2} + \frac{(\omega - \omega_0)^3}{6}\frac{d^3k(\omega)}{d\omega^3} + ... \tag{2.13}$$

Where $n(\omega)$ is the frequency dependant index of refraction, and c is the speed of light in vacuum.

The Group Velocity Dispersion (GVD) is the dispersion per unit length. Later in the text both 2^{nd} and 3^{rd} order GDD and GVD will be referred to as simply 2^{nd} and 3^{rd} dispersion, but it should be clear based on units which one is appropriate.

The index of refraction $n(\omega)$ for a given material can be calculated using the Sellmeier coefficients [23, pg. 179] and thus the dispersion for a pulse propagating though a material can be determined.

$$D_2(\omega, L) = \frac{1}{2}\frac{1}{6}\frac{d^2}{d\omega^2}\left(\frac{n(\omega)\omega}{c}\right) L \tag{2.14}$$

$$D_3(\omega, L) = \frac{d^3}{d\omega^3}\left(\frac{n(\omega)\omega}{c}\right) L \tag{2.15}$$

All that is needed then is knowledge of the material type and the beam path through the object, and its dispersion can be calculated.

2.3 Non-Linear Optics

2.3.1 Polarization

When light interacts with a dielectric material the time dependant polarization ($P(t)$) can be expressed in terms of the electric field[4, pg. 2]:

$$P(t) = \epsilon_0 \chi E(t) \tag{2.16}$$

where ϵ_0 is the permittivity of vacuum. χ is known as the linear susceptibility and is a measure of how strongly the polarization depends on the electric field. Polarization is the dipole moment per unit volume[4, pg. 1].

Eq. 2.16 is only an approximation applicable when the electric field intensity is low. To be able to consider larger field intensities a power series expansion is used[4, pg. 2]:

$$P(t) = \epsilon_0[\chi^{(1)}E(t) + \chi^{(2)}E^2(t) + \chi^{(3)}E^3(t) + ...] \tag{2.17}$$

When a laser pulse is sufficiently compressed, the instantaneous electric field intensity can become so high that effects attributed to the higher order terms can be detected.

2.3.2 Sum Frequency Generation

Many non-linear effects are possible with sufficient power. We are primarily concerned with a second order effect so we only need to look at the second order:

$$P^{(2)}(t) = \epsilon_0 \chi^{(2)} E^2(t) \tag{2.18}$$

$\chi^{(2)}$ is the second order non-linear susceptibility[4, pg. 2]. For simplicity we make the assumptions that the material is lossless, dispersionless. We will also assume that the $\chi^{(2)}$ for our dielectric material is "fast" or in other words $P^{(2)}(t)$ depends only on the instantaneous electric field strength [4, pg. 2].

Let us consider an electric field formed by adding two distinct fields:

$$E(t) = E_1 e^{-i\omega_1 t} + E_2 e^{-i\omega_2 t} + c.c. \tag{2.19}$$

Substituting this into Eq 2.18 we get [4, pg. 5]:

$$P^{(2)}(t) = \epsilon_0 \chi^{(2)} [E_1 e^{-i\omega_1 t} + E_2 e^{-i\omega_2 t} + c.c.][E_1 e^{-i\omega_1 t} + E_2 e^{-i\omega_2 t} + c.c.] \tag{2.20}$$

$$P^{(2)}(t) = \epsilon_0 \chi^{(2)} [E_1^2 e^{-2i\omega_1 t} + E_2^2 e^{-2i\omega_2 t} + 2E_1 E_2 e^{-i(\omega_1+\omega_2)t} + ...] \tag{2.21}$$

The first two terms are Second Harmonic Generation (SHG) because they represent light radiating at at $2\omega_1$ and $2\omega_2$ respectively[4, pg. 5-6]. SHG will be present in the signal produced by the experiments by this thesis, but will not be detected due to spatial considerations. The third term is Sum Frequency Generation (SFG) because the radiated light will have a frequency $\omega_2 + \omega_2$ that is the sum of the frequencies of the two input fields[4, pg. 6-7]. This SFG will be very important in the experiments discussed later. The rest of the terms not shown in the expanded product will not feature in the experiments either due to spatial considerations, or due to poor phase-matching efficiency, which will be discussed in the following section.

In order to achieve a detectable 2^{nd} order non-linear optical effect, one needs a material that possesses a large $\chi^{(2)}$. Also it should be noted that a full treatment of SFG will take into account the spatial aspects, which cause $\chi^{(2)}$ to become a third rank tensor[4, pg. 2], limiting the possible methods and materials for achieving SFG. For the experiments in this thesis these issues did not cause significant impact. For further reading see [4, Ch. 1.3].

2.4 Phase Matching

In order to achieve SFG the material must have a strong $\chi^{(2)}$, but that is not a sufficient condition. Let us look at Eq. 2.18 and 2.19. After re-introducing the spatial information contained in the wave number $\vec{k}$ the electric field becomes [4, pg. 74]

$$E(t,\vec{k}) = E_1 e^{-i\omega_1 t} e^{i(\vec{k}_1\cdot\vec{r})} + E_2 e^{-i\omega_2 t} e^{i(\vec{k}_2\cdot\vec{r})} + c.c., \tag{2.22}$$

where $\vec{r}$ is the direction of propagation of the electric field. The SFG term becomes

$$P^{(2)}_{SFG}(t,\vec{k}) = E_1 E_2 e^{-i(\omega_1+\omega_2)t} e^{i(\vec{k}_1+\vec{k}_2)\cdot\vec{r}} = E_3^2 e^{-i(\omega_3)t} e^{i(\vec{k}_3)\cdot\vec{r}}. \tag{2.23}$$

We can write the intensity in terms of the wave vector mismatch $\Delta\vec{k} = \vec{k}_1 + \vec{k}_2 - \vec{k}_3$. To remove the spatial dependance, the volume must be integrated over the interaction volume[23, pg. 890].

$$I_3 \propto |\int_V E_3^2 e^{-i(\omega_3)t} e^{i(\Delta\vec{k}\cdot\vec{r})} d\vec{r}|^2 \tag{2.24}$$

In the special case that the interaction is one dimensional extending along the beam axis for a length L this evaluates to[23, pg. 891]:

$$I_3 \propto |\int_0^L e^{-i(\omega_3)t} e^{i(\Delta\vec{k}\cdot\vec{r})} d\vec{r}|^2 = L^2 sinc^2(\Delta k L/2\pi) \tag{2.25}$$

Δk is no longer a vector, instead it is the scalar equivalent to the z component of the vector $\Delta\vec{k}$. The sinc function is maximum when the argument is 0. Since L is non-zero the phase matching intensity is maximum when $\Delta k = 0$. This means that two conditions must be met in order to have SFG:

$$\omega_3 = \omega_1 + \omega_2 \tag{2.26}$$

$$\vec{k}_3 = \vec{k}_1 + \vec{k}_2 \tag{2.27}$$

These are known as the phase matching conditions, and respectively correspond to energy and momentum conservation[27, pg. 50]. The reason they are known as phase matching is that when the conditions are met, the propagation of the polarization in the material will match the propagation of the emitted field, so that they stay in phase[27, pg. 49]. When this happens newly emitted field will interfere constructively with the field emitted previously in the propagation path, and the new field will grow proportional to the propagation distance squared[27, pg. 49]. Otherwise the beams will begin to get out of phase, and the field will interfere destructively, ruining the SFG signal.

For SFG $\vec{k_1}$ and $\vec{k_2}$ do not need to be parallel, and a consequence is that SFG is not constrained to occur only in the same direction as the input beams[27, pg. 51]. By interacting two beams with different direction, the SFG caused by cross-interaction will be emitted between the input beams. This is very useful to us because it means we can spatially filter out the SFG due solely to either of the beams.

2.4.1 Phase Matching Efficiency

The efficiency of phase matching is described by the following equation[27, pg. 49]:

$$I(L,t) = \frac{c\mu_0\omega_0^2}{4}|P|^2L^2sinc^2(\Delta k\, L/2) \tag{2.28}$$

Where L is the length of the material, and $\Delta k = k_1 + k_2 - k_3$ [27, pg. 49]. μ_0 is the magnetic permeability , c is the speed of light in vacuum P is the polarization and ω is the angular frequency. The value of the sinc function is 1 when the argument is 0, and quickly drops away as the magnitude of the argument increases. So it is important that the argument is as close to zero as possible to get a strong signal. This can be accomplished by making L very small (using a thin crystal), but this decreases the interaction region and so it also decreases the signal. The other option is to try and make Δk small. k is actually a function of wavelength, $k = \frac{n(\omega)\omega}{c} = \frac{2\pi n(\lambda)}{\lambda}$, so in the case of SHG Δk reduces to[27, pg. 53]:

$$\Delta k = 2k_1 - k_3 \propto \frac{2n(\lambda_0)}{\lambda_0} - \frac{n(\lambda_0/2)}{\lambda_0/2} \tag{2.29}$$

This implies that we want $n(\lambda_0) = n(\lambda_0/2)$, this is not common in most materials. The solution is to use a *birefringent* material[27, pg. 51][9, pg. 336]. A birefringent material has 2 indices of refraction, depending on the polarization. The birefringent material will define an axis such that light polarized perpendicular (ordinary) to that axis will have a different index of refraction then light polarized parallel to that axis (extraordinary)[9, pg. 340]. This axis is known as the optic axis [9, pg. 336]. By adjusting the angle of the optic axis relative to the beams the index of refraction for the extraordinary beam can be tuned so that the $n_{o,e}(\lambda_0, \phi) = ne, o(\lambda_0/2, \phi)$, and SFG can occur using the formula [4, pg. 83]:

$$n_e(\lambda, \phi) = \frac{1}{\sqrt{\frac{cos^2(\phi)]}{n_o(\lambda^2} + \frac{sin^2(\phi)]}{n_e(\lambda)^2}}} \tag{2.30}$$

2.4.2 Phase Matching Bandwidth

This subsection is closely based on the derivation in [27, pg. 53].

Once again, because the index of refraction is dependant on wavelength, the phase matching condition will not be equally satisfied for all the entire spectrum of input light. As a measure of the bandwidth that can be phase-matched efficiently at the same time we can calculate the SFG efficiency from equation 2.28 as a function of the crystal length L ,

the angle to the optic axis ϕ, and the wavelength of the input[27, pg. 53]. First we define our Δk for SFG as

$$\Delta k = k_1 + k_2 - k_3 \tag{2.31}$$

and write Eq2.26 in terms of wavelength

$$\frac{1}{\lambda_3} = \frac{1}{\lambda_2} + \frac{1}{\lambda_1}, \tag{2.32}$$

so by equation 2.31, we have

$$\Delta k(\lambda_1, \lambda_2, \lambda_3) = 2\pi \left(\frac{n(\lambda_1)}{\lambda_1} + \frac{n(\lambda_2)}{\lambda_2} - \frac{n(\lambda_3)}{\lambda_3} \right). \tag{2.33}$$

where the index of refraction depends on the polarization, and in the case of e-polarization, the index of refraction also depends on the angle ϕ to the optic axis.

2.4.3 Type I vs Type II

The phase matching conditions do no require the input beams to be the same polarization, just the the indices of refraction of the three beams minimize Δk. One possible combination of polarization between the three beams is type I where the input beams share the same polarization and the output beam is the opposite polarization.

$$\Delta k(\lambda_1, \lambda_2, \lambda_3) = 2\pi \left(\frac{n_o(\lambda_1)}{\lambda_1} + \frac{n_o(\lambda_2)}{\lambda_2} - \frac{n_e(\lambda_3, \phi)}{\lambda_3} \right). \tag{2.34}$$

Note the alternate case where the input beams are e-polarized and the output beam is o-polarized is also possible. We then use the Sellmeier coefficients to calculate $n(\lambda_{1\,2})$ and $n(\lambda_{3,\phi})$ and plot the efficiency for a given output wavelength λ_3. We pick a suitable λ_3 and ϕ and plot the $sinc^2$ portion of Eq 2.28 as a function of λ_1.

β-barium borate (BBO), is a common non-linear crystal in our lab. An example is given in Fig 2.1 for BBO, with a thickness of 2mm.

We see that the phase-matching is above 50% for over 100nm, so this has suitable phase matching bandwidth for our experiments

It may provide advantage to use phase match such that the two input beams have different polarizations. This is known as type II. Unfortunately type II phase matching typically has significantly reduced phase matching bandwidth compared to type I. A plot similar to Fig 2.1, but using type II phase matching is shown in Fig 2.2. The phase matching bandwidth is much narrower, and unsuitable for the experiments in this thesis.

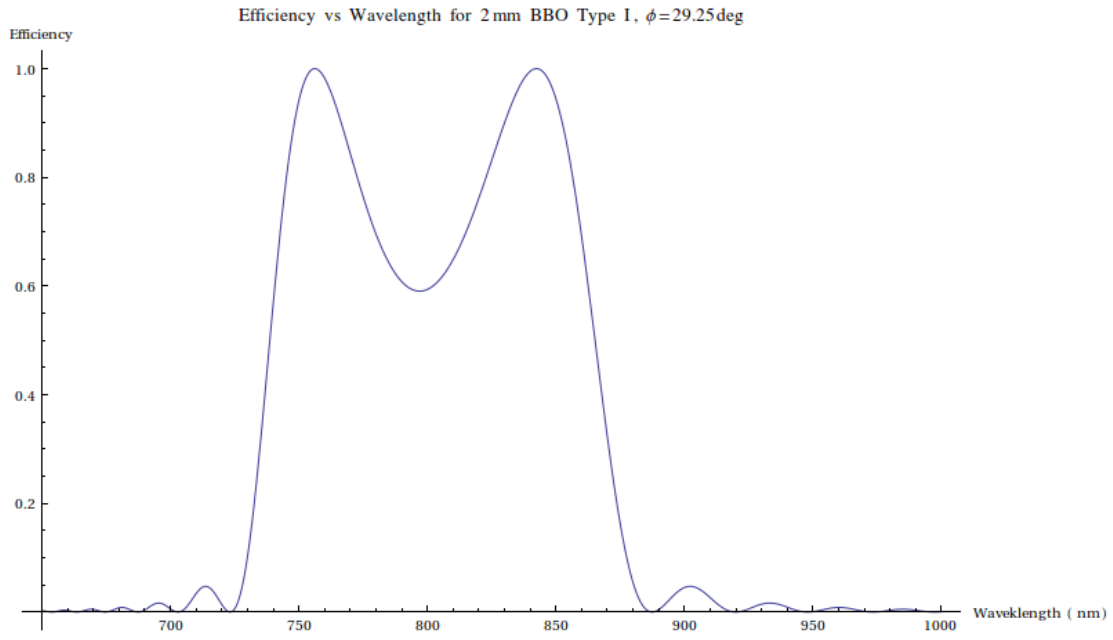

Figure 2.1: Plot Of Efficiency vs wavelength for 2mm BBO Type I
The phase-matching is above 50% for over 100nm.

2.5 Optical Coherence Tomography

Optical coherence tomography (OCT) is an interferometric imaging technique that uses broad bandwidth light to achieve high axial resolution. Because the bandwidth is broad, we some times refer to it as white light interferometry (WLI). The detected signal of a white light interferometer for an intensity (square law) detector is [12, pg. 14]:

$$I = \int |E_1 + E_2|^2 d\omega \tag{2.35}$$

Where E_1 and E_2 are the electric field components of the light from the two arms of the interferometer. It is easy to see that common phases between E_1 and E_2 has no effect on the signal.

For fields with Gaussian spectra and spectral bandwidth σ, and a path difference such that $E_1 = E_1(t - \Delta\tau)$ and $E_2 = E_2(t)$, it can be shown that Eq 2.35 becomes[5, pg. 111]:

$$I(\Delta\tau) = \int |E_1(t - \Delta\tau) + E_2(t)|^2 d\omega = \frac{1}{2} + \frac{1}{2} e^{-\frac{\Delta\tau^2}{8\sigma^2}} cos[\omega\Delta\tau] \tag{2.36}$$

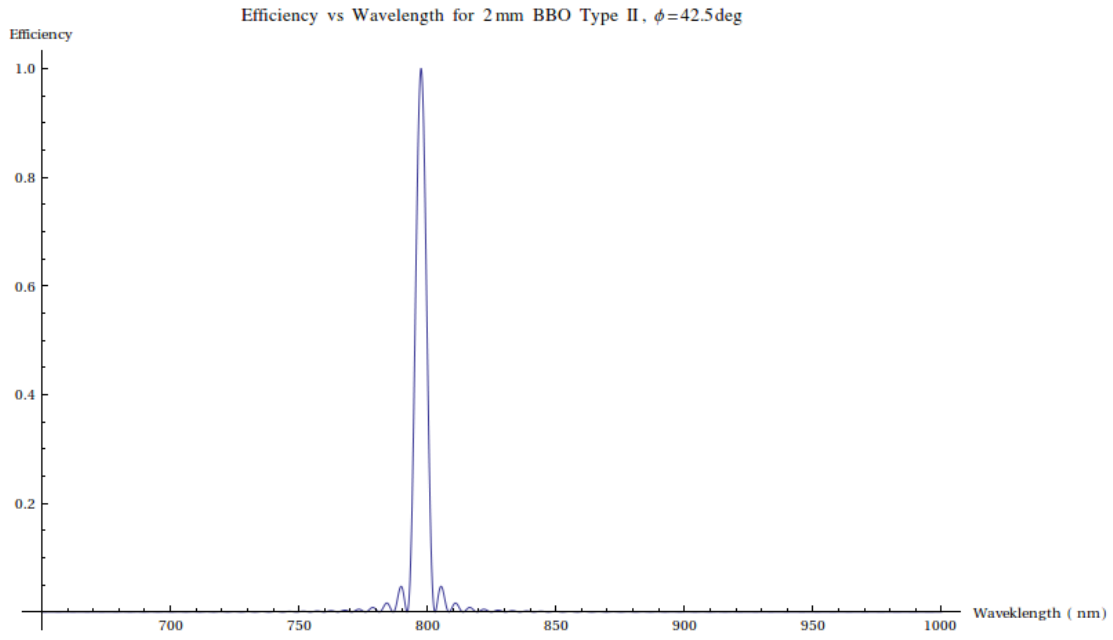

Figure 2.2: Plot Of Efficiency vs wavelength for 2mm BBO Type II
The phase matching is much narrower than type I in the previous figure.

2.5.1 Coherence Length

As the name suggest, the axial imaging resolution of OCT is related to the coherence length of the light source being used. The coherence of a light source is the time or distance over which the light will interfere with a copy of itself. It is defined in terms of the auto-correlation $G(\tau)$ at some time delay time τ divided by the auto-correlation $G(0)$ at zero delay[23, pg. 408]

$$G(\tau, f(t)) = \int f^*(t) f(t+\tau) dt \tag{2.37}$$

and

$$g(\tau) = \frac{G(\tau)}{G(0)}. \tag{2.38}$$

The coherence time usually refers to the time delay τ_c where the coherence drops to a certain fraction of the maximum, usually $\frac{1}{2}$ [23, pg.408]. The coherence length then $l_c = v\tau_c$ where v is the speed of light in the medium. For Eq 2.36 the FWHM coherence length for a Gaussian source can be shown to be[5, pg. 111]

$$\Delta l_c = \frac{2v\ ln(2)}{\Delta\omega} \tag{2.39}$$

where $\Delta\omega$ is the FWHM bandwidth of the light source.

2.5.2 Optical Coherence Tomography Set-up

To perform OCT the light is sent into a Michelson interferometer with the sample in place of one of the end mirrors. Each interface in the sample will produce interference with the reference beam, with the duration of the interference pattern determine by the coherence of the light source used.

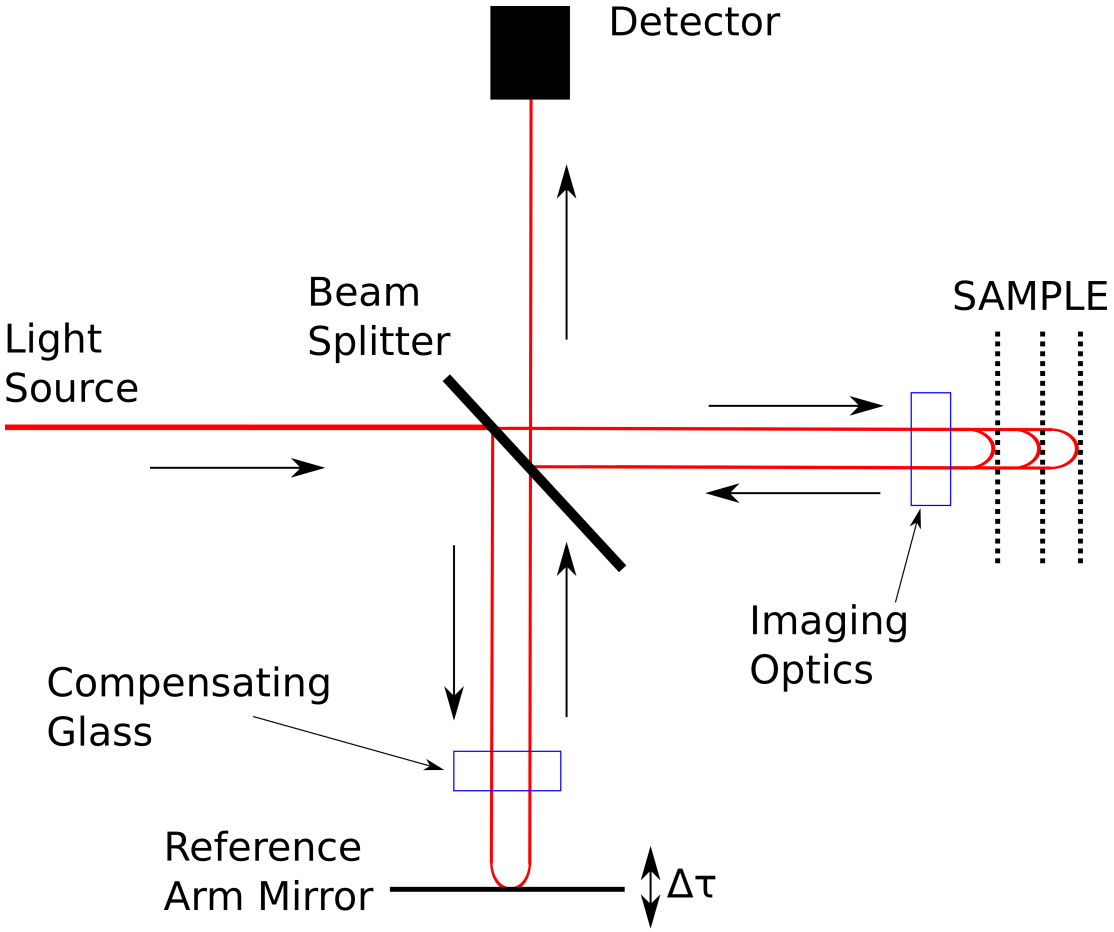

Figure 2.3: Diagram of an OCT set-up
The reference arm is adjustable for path delay $\Delta\tau$. The optics used to image the sample create dispersion which must be compensated in the reference arm.

The maximum axial resolution $1/\Delta l_c$ of the system is then related to the FWHM bandwidth of the source $\Delta\omega$ and the pulse duration $\Delta\tau$ by[3]

$$\Delta l_c = c\Delta\tau \tag{2.40}$$

$$\Delta\tau = \frac{4\pi c ln(2)}{\Delta\omega}. \tag{2.41}$$

We can also write this in terms of wavelength [5, pg. 112]

$$\Delta L = \frac{2ln(2)}{\pi}\frac{\lambda^2}{\Delta\lambda} \tag{2.42}$$

where λ is the center wavelength and $\Delta\lambda$ is the FWHM bandwidth of the light source in wavelength.

The optics used to image the sample, as well as the sample itself, create dispersion. 2^{nd} order dispersion causes the temporal duration of the pulse to increase by the following relation[24, pg. 356,Eq. 66][12, pg. 16]:

$$\Delta\tau(\beta) = \frac{2ln(2)}{\Delta\omega}\sqrt{1+\beta^2 L^2 \Delta\omega^2} \tag{2.43}$$

Where β is the 2^{nd} order dispersion and L is the single pass length through the dispersive material. This causes the axial resolution to decrease by Eq. 2.40. Another way of undertanding this is that dispersion causes the interference pattern to broaden, making interfaces that are close together indistinguishable, which is undesirable. The dispersion therefore must be compensated in the reference arm by adding glass. Interestingly, dispersion common to both arms has no effect on an OCT set-up because the interference is 1st order. It is easy to see this from Eq. 2.36 because phases common to E_1 and E_2 are cancelled by the magnitude of the electric field.

2.6 Quantum OCT

An alternative method of OCT using pairs of correlated photons has been demonstrated, known as Quantum OCT (Q-OCT) [1]. Q-OCT makes use of a phenomenon know as the Hong-Ou-Mandel dip. The main advantage of this method is that it is immune to the broadening caused by even order dispersion in regular OCT [21]. Q-OCT has been used to image a biological sample, an onion [16]. The onion was treated with gold nano-particles, to increase the signal reflected from it. This highlights the major disadvantage of Q-OCT, sources of strongly correlated photon pairs are not capable of producing the intensities required for quick scanning [13].

2.6.1 Hong Ou Mandel Dip

The Hong-Ou-Mandel (HOM) dip is a phenomenon that occurs in an HOM interferometer. The ideal HOM interferometer is an interferometer in which a pair of correlated photons interfere at a 50/50 beam splitter [17][10].

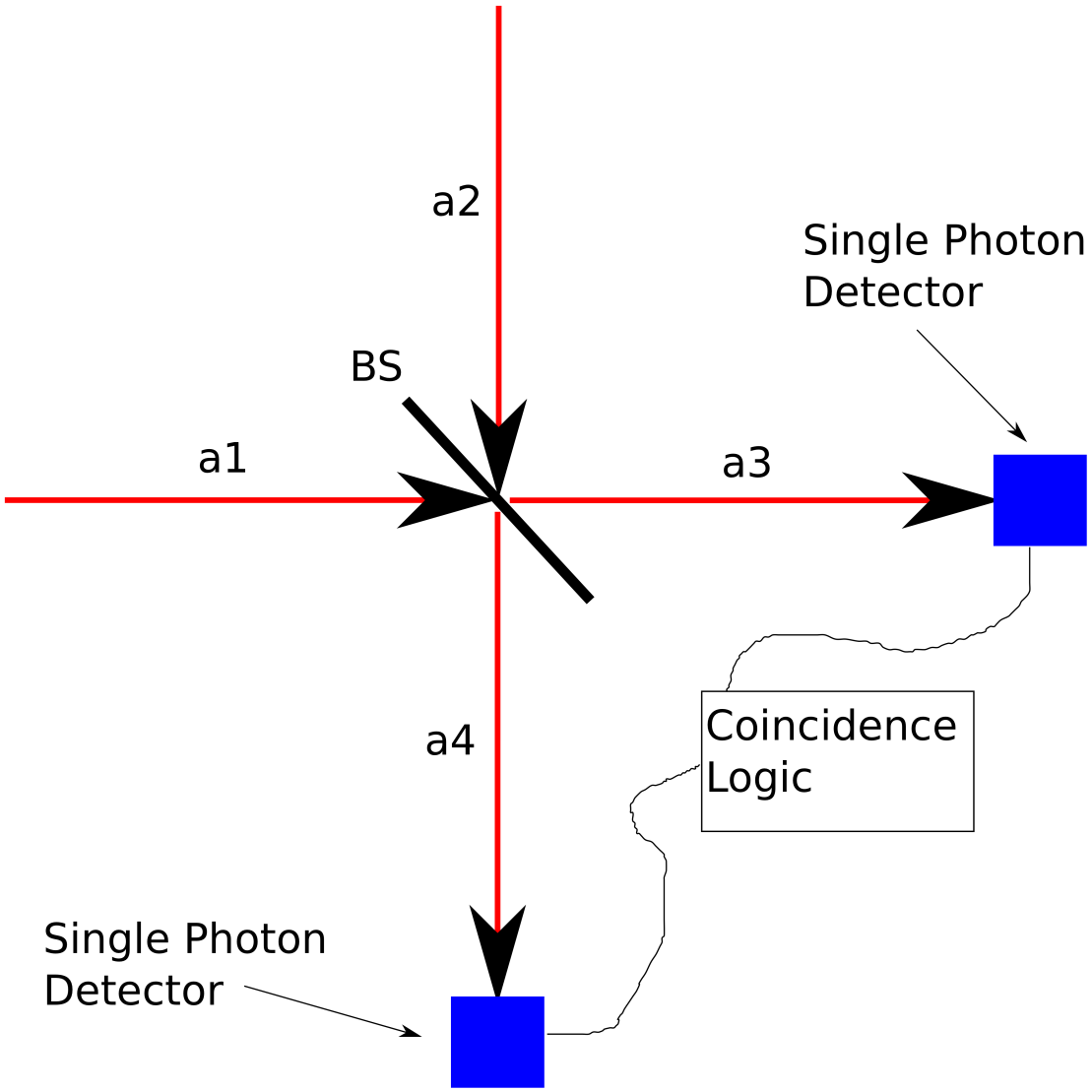

Figure 2.4: Diagram of Beam Splitter Modes
The single photon detectors produce a "click" when a photon arrives. The coincidence logic produces a click when a photon arrives at each single photon detector within a specific time window.

The photons exiting the BS are detected using single photon detectors, which produce a "click" each time a photon is detected. The clicks are sent through logic that only outputs

true if a click is detected in each output mode within a specified time window. Each time the logic evaluates true the coincidence count increases by one.

The quantum description of a 50/50 BS is represented by the unitary matrix equation [8, pgs. 239,248-49]

$$\begin{bmatrix} a_1 \\ a_2 \end{bmatrix} = \frac{1}{\sqrt{2}} \begin{bmatrix} 1 & 1 \\ 1 & -1 \end{bmatrix} \begin{bmatrix} a_3 \\ a_4 \end{bmatrix} \tag{2.44}$$

where a_1 and a_2 represent the input modes and a_3 and a_4 output modes of the beams splitter. We can then rewrite the input modes in terms of the output modes:

$$a_1 = \frac{a_3 + a_4}{\sqrt{2}} \quad , \quad a_2 = \frac{a_3 - a_4}{\sqrt{2}} \tag{2.45}$$

The difference in sign represents the phase difference required to preserve the unitarity in the BS matrix [8, pg. 248].

The state describing a photon in each input mode of the BS can be written in terms of the creation operators $a_n^\dagger$ operating on the vacuum state $\mid 0\rangle$, which is a short form for the state with zero photons in each of every possible mode $\mid 0\rangle_1 \mid 0\rangle_2 ... \mid 0\rangle_n$ [8, pg. 317]:

$$\mid \Psi\rangle = a_1^\dagger a_2^\dagger \mid 0\rangle \tag{2.46}$$

Which is then rewritten in terms of the output modes:

$$\mid \Psi\rangle = \frac{1}{2}(a_3^\dagger + a_4^\dagger)(a_3^\dagger - a_4^\dagger) \mid 0\rangle_3 \mid 0\rangle_4 = \frac{1}{2}((a_3^\dagger)^2 + (a_4^\dagger)^2) \mid 0\rangle_3 \mid 0\rangle_4 \tag{2.47}$$

where we have dropped all modes from the vacuum that aren't represented by the raising operators. The resulting state is then:

$$\mid \Psi\rangle = \frac{1}{2}(\mid 2\rangle_3 \mid 0\rangle_4 + \mid 0\rangle_3 \mid 2\rangle_4) \tag{2.48}$$

This means both photons will leave the BS in the same port every time so no coincidences will be recorded. This is known as the "HOM Effect"[8, pg. 317].

To further understand the HOM effect, the requirement that the photons are identical must be relaxed. Instead the photons must be correlated such that the *paths* to the BS are indistinguishable[26][12, pg. 19]. If this is the case the paths can then interfere, and the path difference between the photons need not be zero. The coherence length of the photons will limit the range of path delay over which the HOM effect can be observed though. Outside of this range the coincidences will be the same as if the photons have no correlation. This is known as the HOM Dip[8, pg. 323] and is described by the equation[10]:

$$N_c(\tau) = C(T^2 + R^2)\left[1 - \frac{2RT}{R^2 + T^2} g(\tau^2)\right] \tag{2.49}$$

Where R and T are the reflection and transmission coefficients and are 1/2 each for a 50:50 BS. C is simply a constant relating the efficiency of the BS and can be set to 1. $g(\tau)$ is related to the Fourier transform of the photon spectrum. It is assumed the spectrum is Gaussian with FWHM $\Delta\omega$, giving[10]:

$$g(\tau) = e^{-(\Delta\omega\,\delta\tau)^2}/2 \tag{2.50}$$

Substituting this into Eq 2.49 and assuming a 50:50 BS we get:

$$N_c(\tau) = \frac{1}{2}\left[1 - e^{-(\Delta\omega\,\delta\tau)^2}\right] \tag{2.51}$$

So the FWHM of the dip is then only dependent on the spectral bandwidth:

$$\sigma_{FWHM,HOM} = \frac{1}{\sqrt{2}\,\Delta\omega} \tag{2.52}$$

The interference between the paths cannot occur if the paths are distinguishable. As the path delay becomes large the paths become distinguishable, and the interference cannot occur. Another interesting thing to note is that $N_c(0) = 0$, meaning the HOM dip has perfect visibility for an ideal 50:50 BS.

2.6.2 Dispersion Cancellation in HOM

In 1992 Steinberg, Kwiat and Chiao [26] showed that the HOM dip was immune to even order dispersive broadening observed in optical coherence tomography. The method relied on frequency anti-correlated photons described by[21]:

$$\mid \Psi\rangle = \int d\omega' f(\omega') \mid \omega_0 - \omega'\rangle \mid \omega' + \omega_0\rangle \tag{2.53}$$

The coincidence rate was then shown to be[26]

$$N_c \propto \int d\omega' |f(\omega')|^2 \left(1 - cos\left[2\omega'(L_2/c - \alpha L_1)\right]\right) \tag{2.54}$$

Where $f(\omega')$ is related to the spectrum of the photons, L_1 and L_2 are the length of the dispersive medium and the adjustable reference arm. α is group velocity and is related to the wave number. When the wave number for light in a dielectric medium $k(\omega) = \frac{n(\omega)\omega}{c}$

is expanded in a Taylor series around the center frequency of the photons up to second order[26]:

$$k(\omega) = k_0 + \alpha(\omega - \omega_0) + \beta(\omega - \omega_0)^2 \tag{2.55}$$

The group velocity dispersion due to travelling length L_1 will then cause broadening in a WLI signal $\Delta\tau \propto 2\Delta\omega\beta L_1$ [26]. Steinberg et al show that the HOM dip is shifted proportional to 1^{st} order disperion α, but is not affected by the 2^{nd} order disperion β [26].

The state described by Eq. 2.53 implies infinite (perfect) correlation between the photons. Further analysis by Resch et al [21] modified the input state to account for finite (imperfect) correlations:

$$\mid \Psi\rangle = \int d\omega_1 \int d\omega_2 f(\omega_1, \omega_2) \mid \omega_1\rangle \mid \omega_2\rangle \tag{2.56}$$

And $f(\omega_1, \omega_2)$ is the spectrum of the photons, relating the bandwidth of the photons σ to the bandwidth of the pump σ_c [21]. If $\sigma_c \to \infty$ the photons have no frequency correlations. Conversely if $\sigma_c \to 0$ the photons are perfectly correlated and $\omega_1 + \omega_2 = 2\omega_0$ [21].

If the dispersion is purely 2nd order [i.e. $k(\omega) = \beta(\omega - \omega_0)$] it can then be shown that the coincidence rate given the above state is[21]:

$$N_c(\tau) \propto 1 - V(\sigma, \sigma_c, \epsilon) e^{-\frac{\sigma^2(2\sigma^2+\sigma_c^2)\tau^2}{2(2\sigma^2+\sigma_c^2+\epsilon^2\sigma^4\sigma_c^2}} \tag{2.57}$$

Where $V(\sigma, \sigma_c, \epsilon)$ relates the visibiltiy of the dip and is reduced slightly from 1 in the presence of dispersion. When $\sigma_c << \sigma$ it can be shown the FWHM of the HOM dip is[21]:

$$\tau_{FWHM,HOM} = \frac{\sqrt{ln(256)}}{\sigma} \sqrt{1 + \epsilon^2\sigma^4 \frac{\sigma_c^2}{2\sigma^2}} \tag{2.58}$$

So the effect of the 2nd order dispersion is essentially reduced by a factor $\frac{\sigma_c^2}{\sigma^2}$[21]. As $\frac{\sigma_c}{\sigma} \to 0$ the dispersion has no effect.

2.6.3 Biological Q-OCT

In 2009 Nasr, Goode et al [16] demonstrated a Q-OCT set-up imaging an onion. The set-up used pairs of photons created by Spontaneous Parametric Down Conversion (SPDC), which is roughly the time reversal of SFG. The system generated only $0.5pW$ of optical power. This may have been the reason why the system required $5s$ integrating time at each $1\mu m$ axial step in their scans [16]. For comparison the experimental set-up used in this

thesis is capable of scanning at a speed of $200mm/s$ corresponding to $5\mu s$ for every $1\mu m$ step without any special coatings. Also the visibility of the HOM dip from the sample was only 0.11 [16], whereas the ideal HOM dip has a visibility of 1.00, so the technique is not yet perfected.

2.7 Chirped Pulse Interferometry

This section follows the derivation given in [21].

A new method of combating 2nd order dispersion broadening in classical OCT was recently developed[11]. This method is known as chirped pulse interferometry(CPI). CPI is essentially the time reversal of Q-OCT. Instead of generating 2 red frequency-correlated photons from a narrow bandwidth blue laser, CPI generates a narrow bandwidth blue signal from two red frequency correlated pulses. The original method for CPI relied on applying positive (negative) second order dispersion $+A(-A)$ to a pair of identical transform-limited pulses [21]with RMS bandwidth σ.

$$E(\omega; A) = E_0 e^{\frac{-(\omega-\omega_0)^2}{2\sigma^2}} e^{iA(\omega-\omega_0)^2} \tag{2.59}$$

The positive and negative dispersed pulses are combined at a BS, creating two new pulses, one a sum of the fields and the other a difference due to the phase picked up at the BS [12, pg. 27] according to Eq 2.44. The first pulse is subjected to a time delay τ:

$$E_1(\omega, \tau) = [E(\omega; A) + E(\omega; -A)]e^{i\tau\omega} \tag{2.60}$$

The second term is subjected to a dispersive material producing purely 2^{nd} order dispersion, ϵ:

$$E_2(\omega, \tau) = [E(\omega; A) - E(\omega; -A)]e^{i\epsilon(\omega-\omega_0)^2} \tag{2.61}$$

The fields are combined at a non-linear crystal suitable for SFG .We assume that the phase matching efficiency is perfect for all frequencies combinations present in the pulse [21]. We also assume that the non-linearity is fast so $\chi^{(2)}$ is constant, and that the pump beams are not depleted [21]. We make the slow-varying amplitude approximation [21][27, pg. 45]. We then re-write Eq.2.18 making the approximation that the radiated field is proportional to the polarization[21]. The SFG field is then [21]:

$$E_{SFG}(\omega, \tau) \approx \int d\omega' E_1(\omega', \tau) E_2(\omega - \omega', \tau) \tag{2.62}$$

E_3 can then be broken down into 2 types of fields. The first are the terms with the same chirp sign. The signal produced by these will be broadband [21] because they are

no different than performing auto-correlation on a pulse with chirp A. The second type of field is effectively the cross correlation between fields with opposite chirp sign. Pulses with strong oppositely chirped pulses have been shown previously to have very narrow bandwidth [20]. Because of this if we assume that the chirp rate is large enough to produce this narrow bandwidth signal, we can filter out the auto-correlation signal and only observe the cross correlation signal by use of a simple narrow-band filter [21]. We can then rewrite the filtered field as [21]:

$$E_{SFG}(\omega,\tau) \approx \int d\omega'[E(\omega';-A)E(\omega-\omega';A) - E(\omega';A)E(\omega-\omega';-A)]e^{i\tau\omega}e^{i\epsilon(\omega-\omega_0)^2} \quad (2.63)$$

What we really want is the signal measured in terms of the time delay τ. Or in other words the intensity[21]:

$$I_{SFG}(\tau) \propto \int d\omega |E_{SFG}(\omega,\tau)|^2 \quad (2.64)$$

The SFG intensity can then be broken down into two parts, a longer duration, broad bandwidth background term $I_{background}$ and a narrow bandwidth term I_{CPI} [21]:

$$I_{SFG}(\tau) \propto I_{background} - I_{CPI} \quad (2.65)$$

When the time delay τ is much less than the time duration of the pulse σ_{rms}, $I_{background}$ is proximately 1 [21]. At the same delay, if the chirp is larger than the dispersion, the CPI term becomes [21]:

$$I_{CPI}(\tau) \propto e^{-\frac{\tau^2}{\tau_{CPI}^2}}. \quad (2.66)$$

The RMS width of the CPI signal is then τ_{CPI}. This term can be simplified if the chirp is larger than the dispersion, $A >> \epsilon$ [21]:

$$\tau_{CPI} = \frac{1}{\sigma}\sqrt{1+\epsilon^2\sigma^4\left(\frac{2+4\epsilon^2\sigma^4}{1+4A^2\sigma^4}\right)} \quad (2.67)$$

Comparing this to the duration for a WLI, Eq 2.43, we see the increase in τ due to the dispersion is reduced by the factor $\frac{2+4\epsilon^2\sigma^4}{1+4A^2\sigma^4}$ [21]. In the limit of no chirp, this factor is approximately 1, so there is no reduction in the time duration, as expected. In the limit of infinite chirp, the factor is zero and there is no increase in time duration due to the dispersion.

For parameters in the area of our experiment ($\sigma \approx 10^-1, \epsilon \approx 10^2, A \approx 10^3$), the increase in duration of the dip is predicted to be proportional to $\frac{\epsilon}{A}$. So a chirp that is ten times larger than the dispersion will reduce the effect of the dispersion by ten times.

2.7.1 Non-Linear CPI

The previous CPI experiments recorded used separate chirped and anti-chirped pulses, and combined them at a BS to produce the necessary frequency correlations [11]. This required discarding 50% of the power. A different chirp that creates similar correlations using only one pulse would correct this.

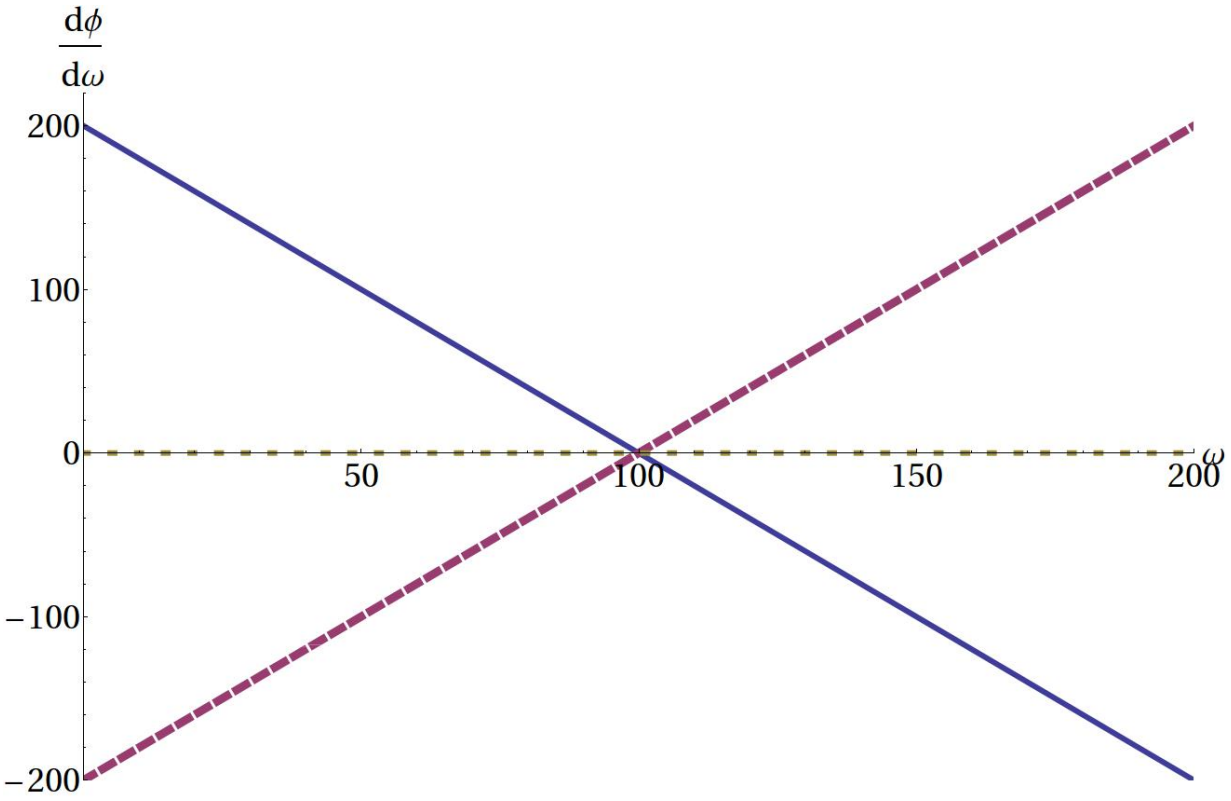

Figure 2.5: Group Delay vs Frequency for Chirped, Anti Chirped and TL (Dotted) Pulses. The Chirped pulse (Dashed) and Anti-Chirped Pulse (Solid) form an"X" when combined at a Beam Splitter. For comparison, a TL pulse (Dotted) is shown and is simply a flat line. In this example, the magnitude of the chirp is $2t^2$ and the center frequency is $100t^-1$.

To better see the effect of CPI chirp, let us look at a plot of group delay vs frequency for chirped and anti chirped pulses as well as a transform limited (TL) pulse . We see in Fig 2.5 that a TL pulse is a flat line, a chirp produces a positive linear slope, and an anti chirp produces a negative linear slope. If we combine the pulses for the chirp and anti-chirp, with zero delay between them, we get an "X" with the intersection centred at the central frequency of the pulse. Because the arms of the "X" have the same magnitude of slope, the two frequencies present at each time delay (one from the chirp, one from the

anti chirp) always add up to twice the central frequency of the pulse. We can translate the "X" to be centred at zero time delay, since this only represents looking at the pulse at a different point in time. Since group delay is just a time, this means for a given frequency in the chirped portion of the pulse, only a few frequencies in the anti-chirped portion of the pulse will be present in the non-linear crystal at the same time. This is the basis for the high degree of frequency correlation.

However, the upper half of the "X" has all of the structure necessary to create the required correlations, so the bottom half may be discarded. The resulting "V" is the group delay function with the minimum degree of correlation.

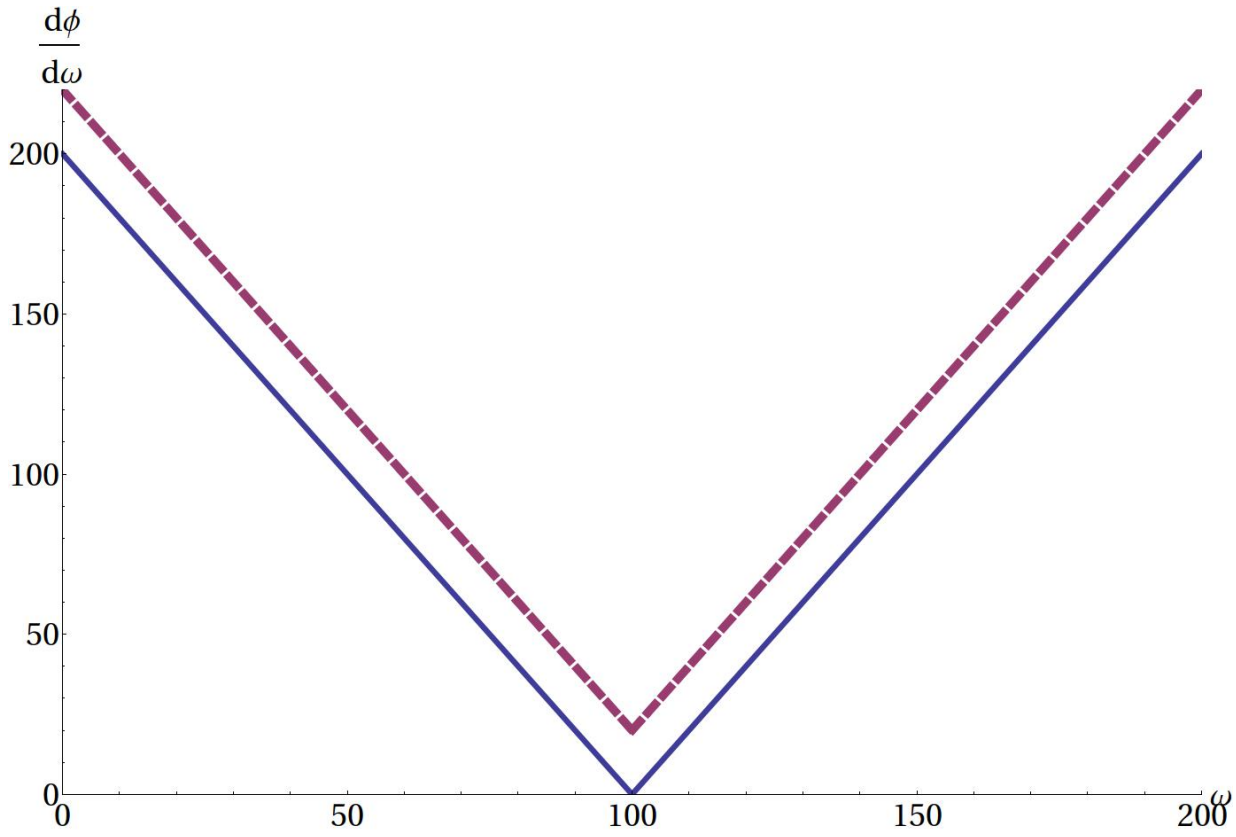

Figure 2.6: Group Delay vs Frequency for the Non-linear Chirped Pulse.
Two pulses are shown with a time delay between them. As the time delay decreases the sum of all the cross correlations at each group delay will become closer and closer to the central frequency.

This function corresponds to quadratic dispersion that switches sign at the center frequency, making the function non-linear:

$$A_{NL} = \{A, \omega < \omega_0; -A, \omega > \omega_0\} \tag{2.68}$$

For this reason we refer to this chirp as the “non-linear” chirp, and CPI using this chirp is referred to as “non-linear CPI” (NL-CPI).

2.7.2 Spectral Filtering

A simulation of the NL-CPI spectrum over a range of time delays shows two peaks that converge to a single peak at $2\omega_0$ (See fig 2.7. If the signal is integrated over all wavelengths, the resulting trace over time will feature a broad background signal due to the double peaked spectrum away from zero time delay (See fig 2.8). However, if the spectrum is filtered to only accept signal near $2\omega_0$, the true CPI signal can be detected without the background (See fig 2.9). Filtering can be accomplished through the use of a monochrometer, or if a spectrometer is used, the data can be ”virtually filtered” by only looking at the data for a narrow band of the spectrum.

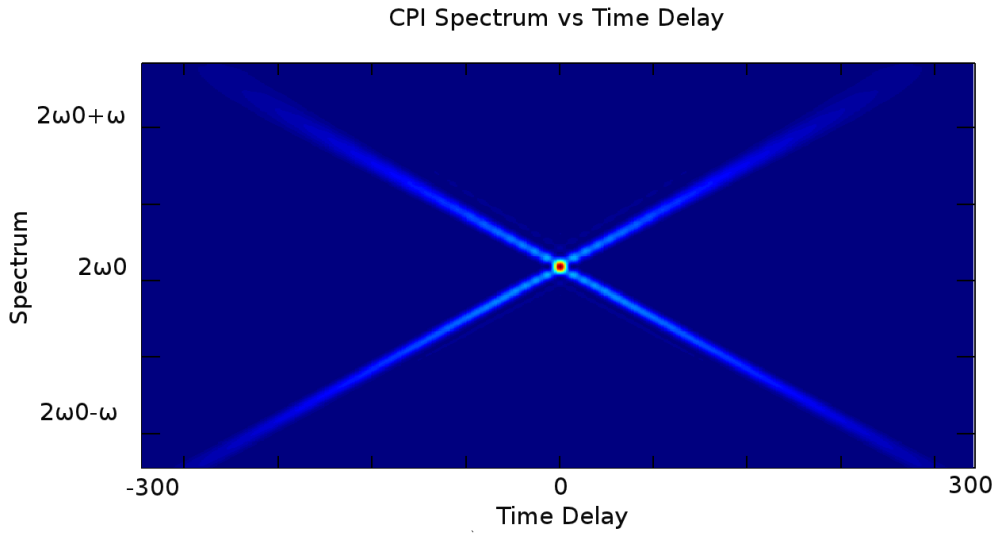

Figure 2.7: Spectrum vs Time Delay
As the time delay in the interferometer decreases the arms of the “X” merge into a single peak at $2\omega_0$.

2.8 Theoretical Model Based on Spectrum Fit

A theoretical model has been developed for CPI with finite chirps[21]. Eq 2.67 is based on this model, and can be used to estimate the pulse duration based on the chirp and second

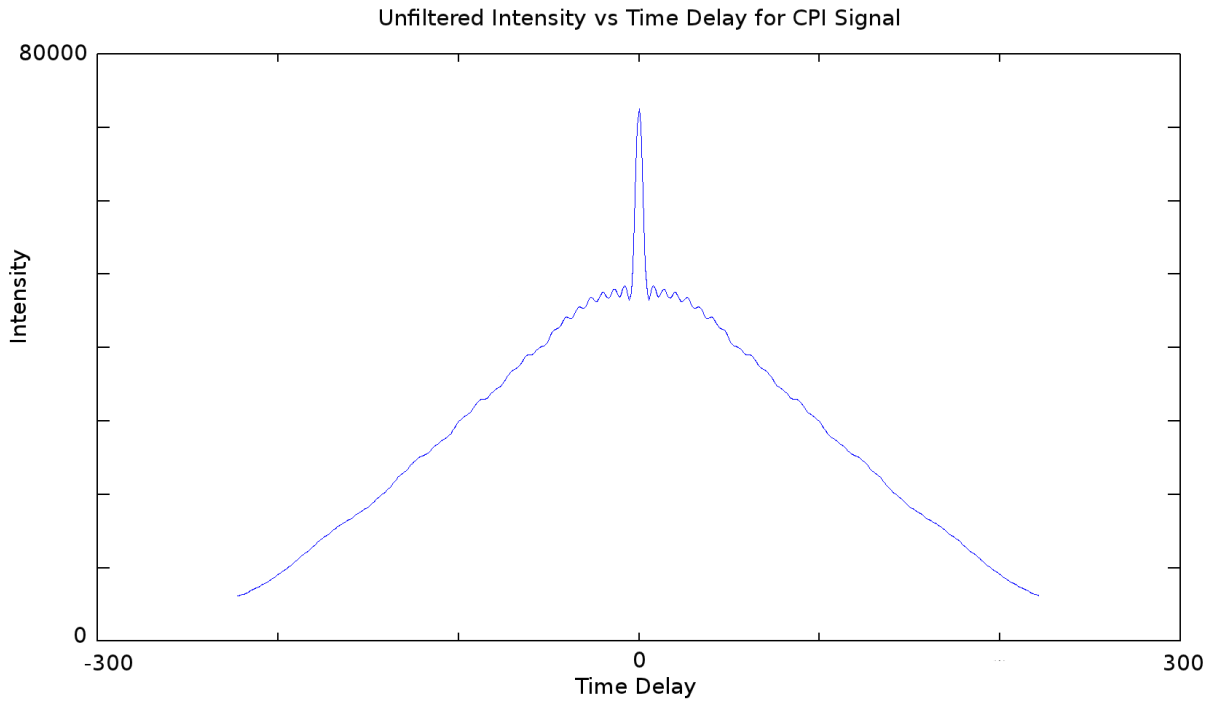

Figure 2.8: Unfiltered CPI Signal vs Time Delay
When the intensity is integrated over all frequencies a large background signal is present. The CPI peak is partially obscured by the background.

order dispersion values. The spectrum data is recorded in the experiment and used to determine the rms width of the spectrum, and the dispersion values are calculated based on the physical parameters of the material used. This is very useful for checking if the CPI system is working as expected, but the method has it's limitations. The model makes the assumption that the chirp parameter is much larger than the dispersion, $A >> \epsilon$. It also assumes a Gaussian spectrum. The model tells us nothing about the spectrum of the CPI signal, and it can only account for dispersion in one arm of the interferometer. Because of this a numerical simulation was also developed, which avoids these limitations.

2.9 Numerical Simulation using Spectrum

The spectrum data was analyzed using a numerical simulation primarily written by Mike Mazurek and Dr. Robert Prevedel in gnu-OCTAVE. The simulation code reads the spectral intensity data in terms of wavelength from a file into an $N \times 2$ array where the first column is the wavelength and the second column is the intensity. The wavelengths are converted to frequencies and the data is interpolated so that the frequencies are evenly spaced. The

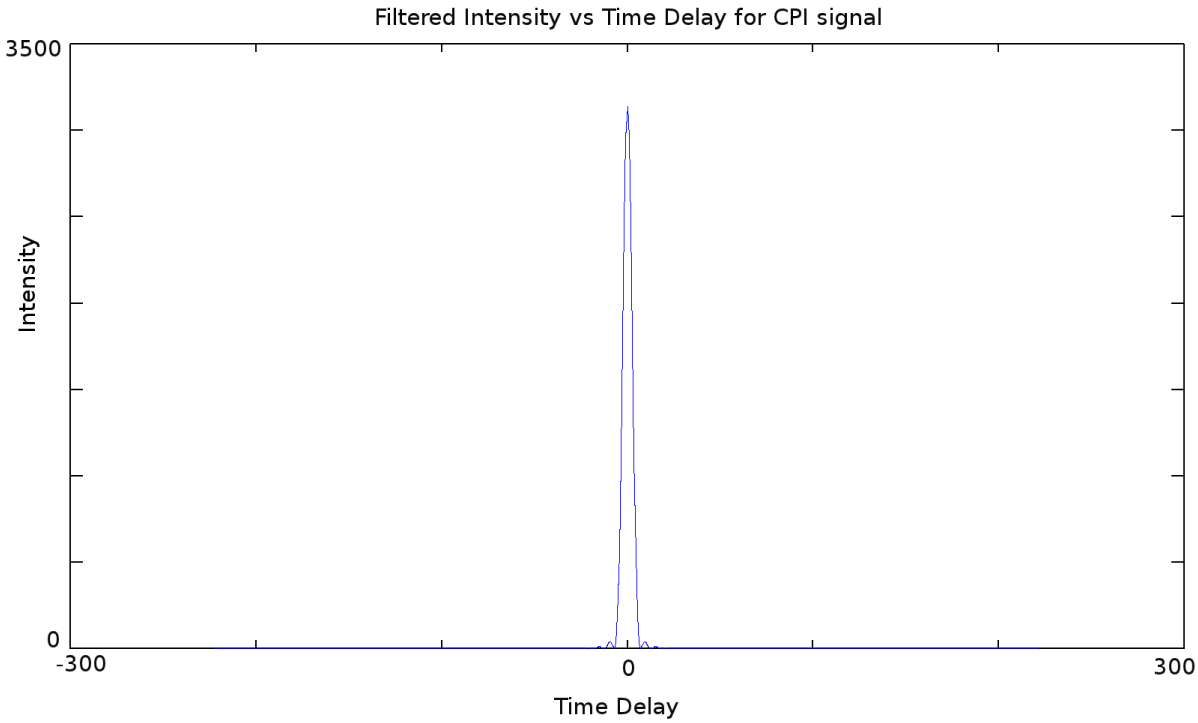

Figure 2.9: Filtered CPI Signal vs Time Delay
When the intensity is filtered over a small frequency range centred at $2\omega_0$ no background signal is present. The CPI peak is clear.

intensity data is converted to electric field amplitude data by taking the square root. It is assumed that we are starting with a TL pulse so all of the phases are zero, and therefore all of the numbers are still real. Two copies of the data are made , representing the pulse in the sample (E_1) and reference arms (E_2). for use by the The phases caused by the NL chirp (with amplitude 'Chirp') are applied to each copy of the pulse:

$$E_m(\omega_n)_{new} = E_m(\omega_n) \cdot Exp\left[i\ Chirp(\omega_n - \omega_0)^3 / Abs(\omega_n - \omega_0)\right] \tag{2.69}$$

where $E_m(\omega_n)$ represents the amplitude at ω_n. The second and third order dispersion caused by material in each arm can then be applied in the form:

$$E_m(\omega_n)_{new} = E_m(\omega_n) \cdot Exp\left[A_m(\omega_n - \omega_0)^3 + B_m(\omega_n - \omega_0)^3\right] \tag{2.70}$$

where A and B are the second and third order dispersion amplitudes in fs^2 and fs^3. To simulate the SFG process, the convolution in frequency of the two pulses is used [21]. However the direct numerical integral takes too long, so the convolution theorem [19, pg. p492] is used to replace the numerical integral with fast Fourier transforms (fft)

$$\int f(\omega)g(\omega-\omega')d\omega' = \mathcal{F}^{-1}(\mathcal{F}\{f\}\cdot\mathcal{F}\{g\}). \tag{2.71}$$

To accommodate the fft algorithm the arrays must be padded out to double the original size[19, pg. 533]. The amplitudes are set to zero and the frequency padding is done in the positive direction from the largest frequency to avoid negative frequencies for simplicity. In order to simulate the time delay between the pulses, the Fourier transform shift theorem is used [19, pg. 491][15][25, pg. 149]:

$$\mathcal{F}(\{x_n\})_k = X_k \tag{2.72}$$

$$\mathcal{F}(\{x_n\cdot e^{\frac{2\pi i}{N}n\cdot m}\})_k = X_{k-m} \tag{2.73}$$

$$\mathcal{F}(\{x_{n-m}\})_k = X_k\cdot e^{-\frac{2\pi i}{N}km} \tag{2.74}$$

which says that adding a linear phase $e^{\frac{2\pi i}{N}nm}$ (equivalent to a time delay between the pulses) causes the data to shift such by m, with data shifted off the back of the array moving to the front. It was confirmed using gnu-Octave that m need not be an integer. The shift by m array units is converted to a real time unit shift t by the following relation[19, pg. 496] used when the data is sampled in time:

$$f_n = \frac{n}{N\Delta t} \tag{2.75}$$

where f_n is the nth frequency in the spectrum array of the data, N is the total number of data points in the sample, and Δt is the value we want, the time spacing. First we convert this to angular frequency, which corresponds to the rest of our models

$$\omega_n = \frac{2\pi n}{N\Delta t}. \tag{2.76}$$

We can then write the next frequency ω_{n+1}

$$\omega_{n+1} = \frac{2\pi(n+1)}{N\Delta t}. \tag{2.77}$$

Then the frequency difference Δf is

$$\Delta f = \omega_{n+1} - \omega_n = \frac{2\pi}{N\Delta t}. \tag{2.78}$$

We then rewrite this to find that the time spacing between consecutive array points is

$$\Delta t = \omega_{n+1} - \omega_n = \frac{2\pi}{N\Delta f}. \tag{2.79}$$

So to shift by m array elements we simply multiply the above equation by m an we can calculate the total time shift

$$t = \frac{2\pi \cdot m}{(N) \cdot spacing} \tag{2.80}$$

where 'N' is the number of elements in the *padded* array and 'spacing' is the frequency difference between array elements used in the actual program.

A loop over multiple shifts ranging from $-z \cdot m$ to $+z \cdot m$ where z the is loop iterator calculates the SFG electric signal at each time delay, squares it to get the intensity and records the data to a 2-d array, where one axis is the spectrum and the other axis is the time delay. The maximum SFG intensity is found in terms of frequency and the row corresponding to that frequency is used as the CPI trace. The frequency is also recorded as the center frequency of the peak. The CPI data is recorded to a .csv file in motor position units and also fit to a Gaussian with a least squares algorithm, written by Mike Mazurek. The parameters of the fit (FWHM in time and space, center position) are converted to motor position units and recorded as well. The output of the simulation was compared to the theoretical predictions for a variety of chirp and dispersion values to confirm it worked as expected.

Chapter 3

Experimental Pulse Shaping and Pulse Compression

3.1 Introduction

The pulse shaper (PS) is the critical element of all the following experiments because CPI depends on shaped pulses. Because of this it is important to make sure the system is well characterized. Our pulse shaper is similar to previous designs using spherical mirrors (Edmund Optics NT43-586, 8 inch focal length, protected gold coated) as lenses[28].

The PS begins as a folded 1 to 1 telescope using two spherical mirrors as the lenses (see Fig 3.2). A Spatial Light Modulator (SLM) is placed at the focal point between the two lenses. A reflective diffraction grating is placed at the outer focal points of each lens. A prism mirror used in between each grating-mirror pair assists in obtaining the optimum geometry. The total distance travelled by the beam is then 4 times the focal length of the mirrors. For this reason we alternatively refer to the rest of the PS minus the SLM as the "4-f".

A laser beam entering the PS is diffracted at the first grating. The first spherical mirror then collimates the diverging colours of the spectrum into parallel beams forming a long thin line of light varying linearly in wavelength from one end of the line to the other. At the same time each individual colour in the beam becomes focused at SLM, meaning that each colour has a well defined position when it reaches the SLM. After travelling through the SLM the second half of the 4-f undoes the spatial separation caused by the first half, combining all of the colours back into a single roughly circular beam.

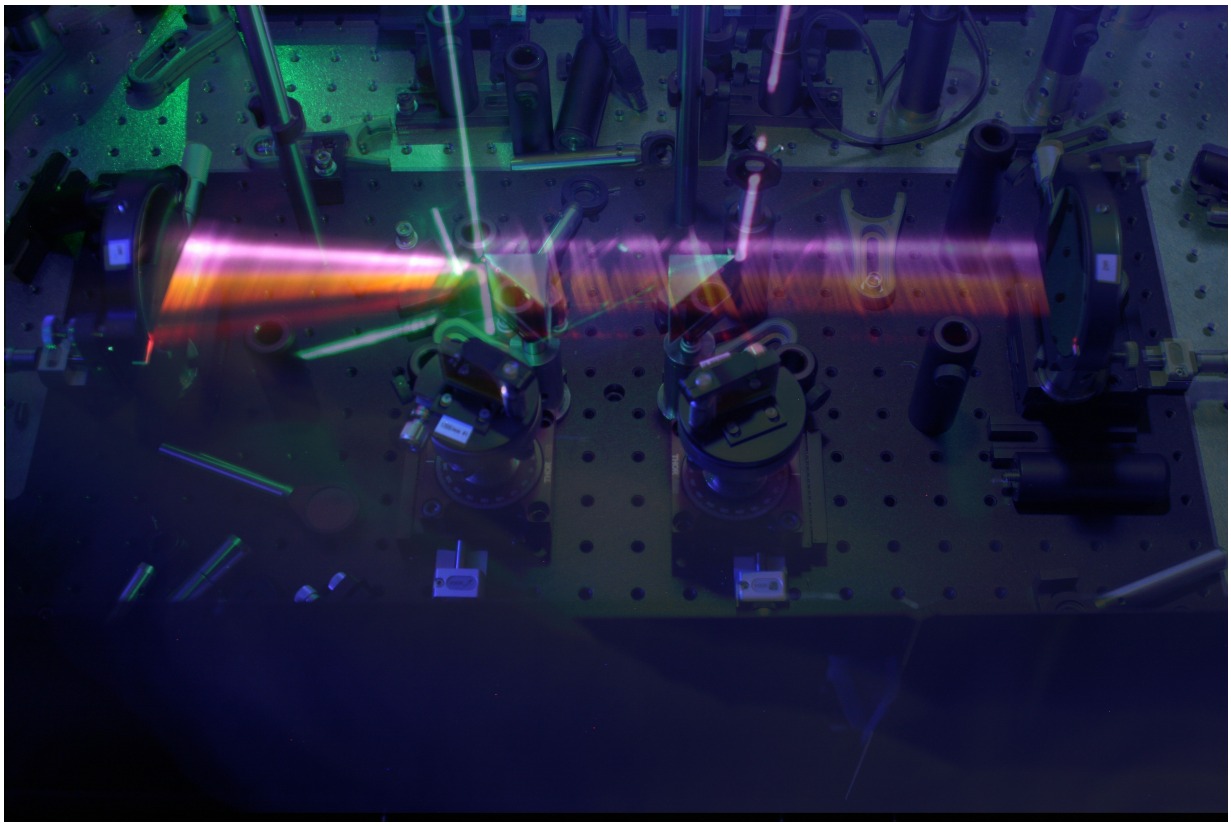

Figure 3.1: Photo of the Pulse Shaper with the SLM removed.
The diffraction and collimation of the light is recorder by tracing the beam path with a white card during a long exposure photo.

3.2 Pulsed Laser

The source of optical pulses for this experiment is a model-locked (ML) titanium-doped sapphire laser (KM-Labs Griffin-10). The laser is capable of producing upto 1000mW of power at 120nm bandwidth centred near 800nm. The bandwidth is adjustable and for many experiments the bandwidth was reduced to 80-100nm for increased stability. The laser mode is roughly a Gaussian profile in both vertical and horizontal profile. The polarization of the laser is linear and horizontal (parallel to the table). In order to achieve a large bandwidth the laser cavity has prisms inside of it. Theses prisms cause dispersion so the pulse exiting the laser is not transform limited, and must be compensated. The PS is used to provide this compensation as well as the the NL chirp.

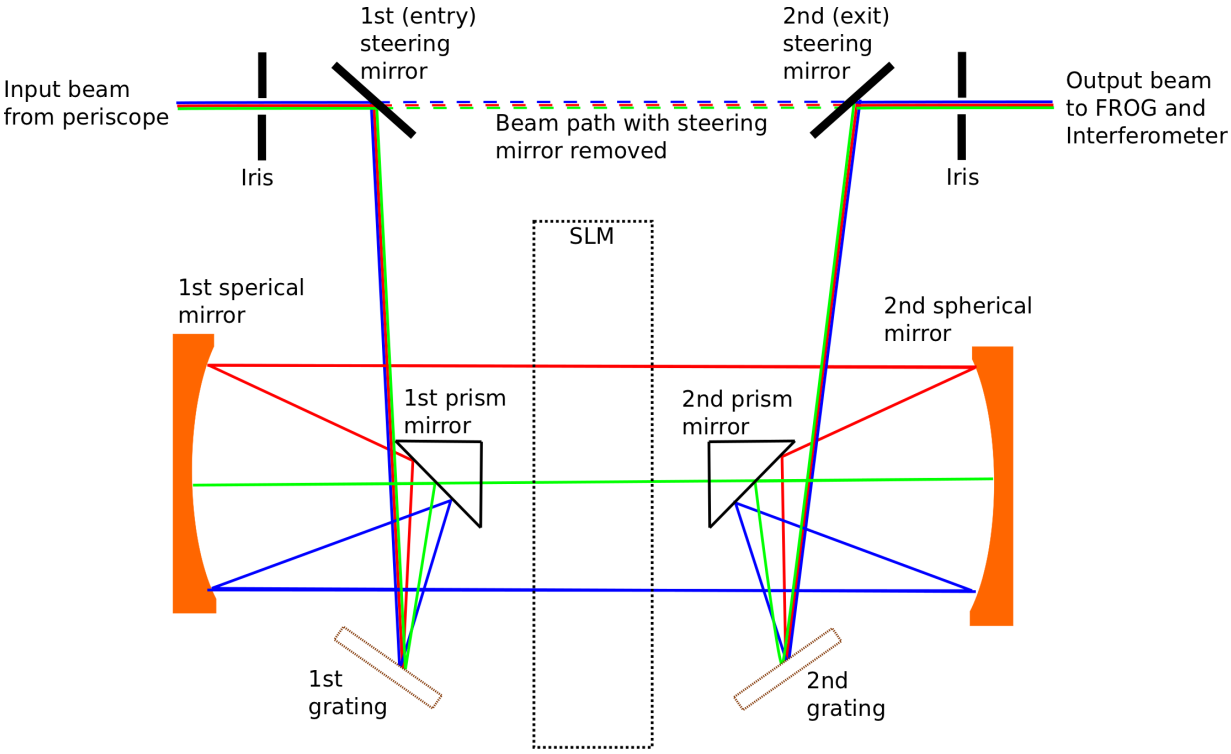

Figure 3.2: Diagram of the Pulse Shaper
The optics are aligned so that the second(right) half of the system exactly cancels the diffraction and focusing of the first(right) half of the system.

3.3 Spatial Light Modulator

The SLM (Cambridge Research Inc. Model SLM-640-D-VN) is the main component of the pulse shaper. Unlike the rest of the components, which are simple static optical devices, the SLM is a dynamic electro-optical device. Therefore it requires much more involved testing to characterize it sufficiently.

The main feature of the SLM is a window consisting of two arrays of 640 liquid crystal pixels called masks. The masks are arranged sequentially in the beam bath so that light travelling perpendicular to the SLM passes through the same pixel in both masks. A USB connection provides an interface to set the voltage value at each pixel. By varying the voltage to a pixel, the birefringence (polarization dependant indices of refraction) of the pixel changes. This has an effect on the light similar to an adjustable wave-plate. When the same pixels in each mask have identical values the effect is a simple phase retardation. When the pixels have different values the effect is rotation of the polarization. When combined with a linear polarizer the rotation can be used to modulate the amplitude. Ultra-fast laser laboratories can exploit both cases to achieve maximum pulse compression.

Because CPI depends on applying a specific phase function to the pulse our PS operates only in the first case during CPI runs. The second case however is useful during the periodic recalibration of the PS so it is characterized as well.

3.4 SLM Characterization

3.4.1 Attenuation Measurement

For the first test a collimated CW laser is used. A multi-mode optical fiber and adjustable fiber collimator are set-up to send the beam through the SLM window perpendicular to the plane of the window. After the SLM the beam is collected at a either a power meter (Thorlabs PM-100) or photo-diode (New Focus Model-2107) depending on the position of a linear translation stage. The power meter provided calibrated results, but had slow acquisition times due to the use of an RS-232 serial connection. The photo-diode provides an analog output for fast, but uncalibrated results. By varying the voltage to one mask while holding the other mask constant, the polarization of the light could be changed. Because the SLM was equipped with horizontal polarizers on both sides the light could be attenuated in this way.

A LabVIEW program was designed to automatically cycle through through a sequence of voltages with configurable start, end and step size for the two masks, and record the results in a 2-D array. The intensity will then change primarily as a function of the difference between the mask values but also slightly as function of the individual mask values. The array is displayed as a 3-D map in real time to assist in troubleshooting. The x and y axis of the map represent the voltage values at mask 1 and mask 2 respectively, while the z axis is the intensity of the signal. The program then outputs the data to a comma-separated variable (csv) text file for easy import and analysis by programs such as Mathematica and MATLAB.

Initially a He-Ne laser (Thorlabs Model HRP050-1) is used to test the equipment set-up and functionality of the LabVIEW program because it is visible to the naked eye, simplifying troubleshooting. Once the set-up and program are sufficiently tested, a diode laser is used with a wavelength of $808nm$. The data was presented in real time by the LabVIEW program. Fig 3.4 clearly shows mirror symmetry along the mask 1 value = mask 2 value line. It is also apparent that the data varies quickly between mask values of 500 and 1500. Because of this it is advisable to avoid having both mask values between 500 and 1500 when attenuating.

3.4.2 Measuring Phase Modulation of a CW laser

For the second test a CW diode laser was used at a wavelength of $808nm$. The beam was configured to pass through a polarizer turned to 45 deg producing diagonally polarized light

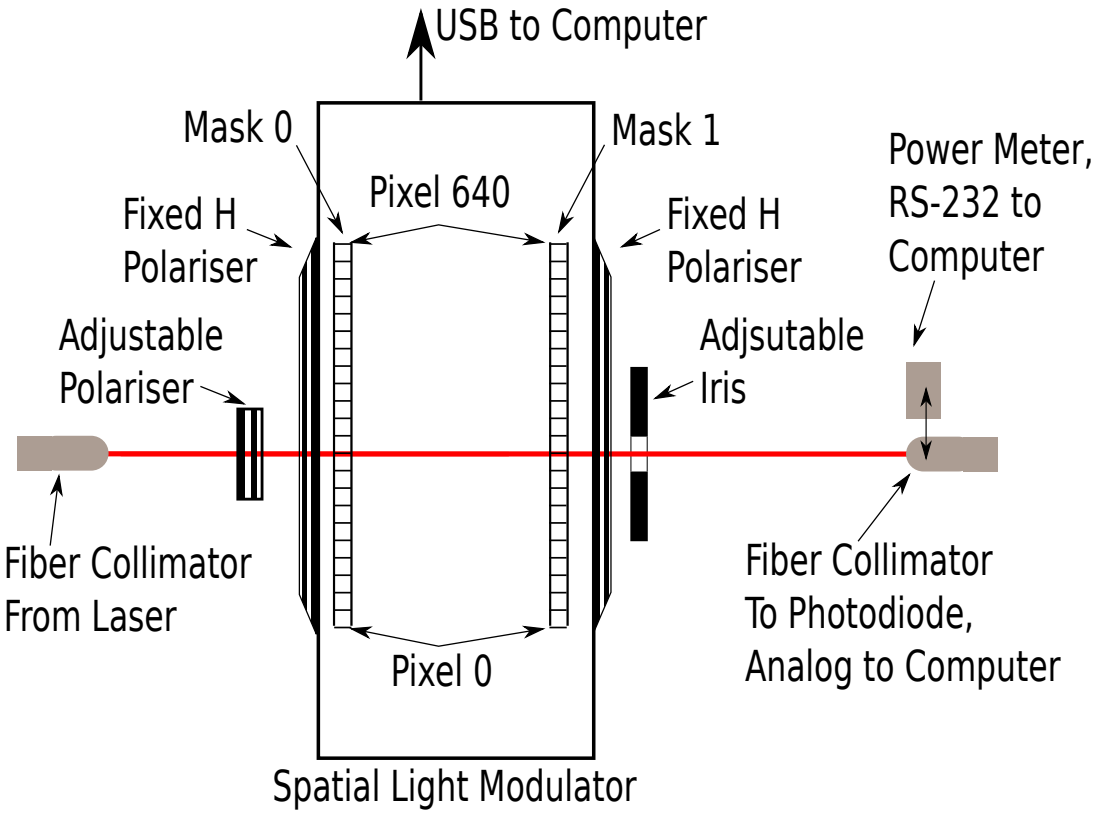

Figure 3.3: Diagram of the Attenuation Measurement Setup.

Fig.3.5. The beam then passes through a calcite beam displacer, spatially separating the horizontal (beam 1) and vertical (beam 2) components of the beam into parallel beams, a few millimeters apart. The second, vertical beam was sent through a half-wave-plate to rotate it to horizontal, then both beams were sent through the SLM. After the SLM the first beam was then rotated to vertical and the beams were recombined with a second identical beam displacer. The displacer was set to the same angle so that the beam paths formed a parallelogram (rather than a trapezoid if it were rotated 180 deg) and both beams travelled the same optical path distance.

The data was collected using a photo-diode and the 808nm diode laser. Multiple runs were completed and averaged over to reduce noise. The phase map (Fig 3.6) appears similar to the attenuation map. This similarity makes sense since both attenuation and phase effects rely on the different applications of the same variable index of refraction in the pixels. Based on the shape of a single line in the data (representing a cross section of the surface), it was decided that a good candidate for fitting the data would be a sinusoidal

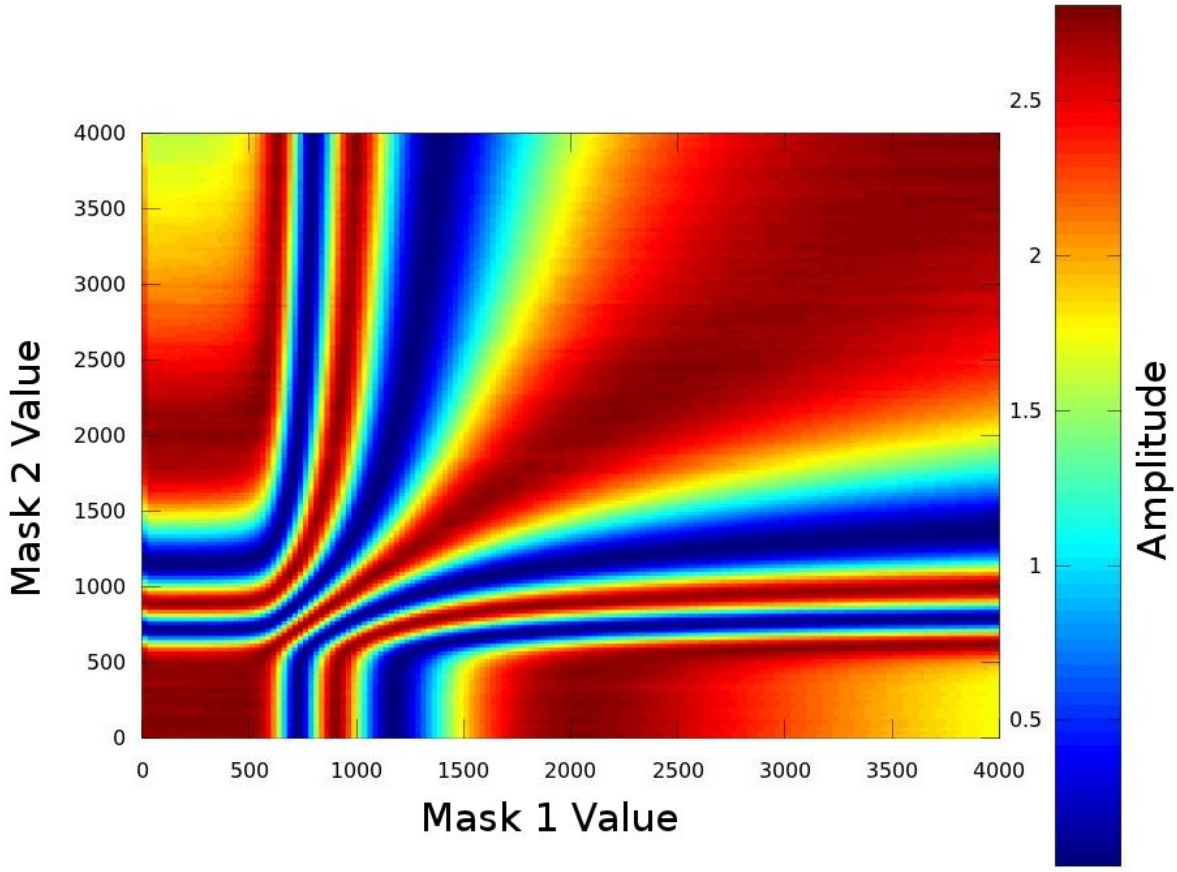

Figure 3.4: Attenuation Map
The dark blue areas are where the attenuation is strongest, approaching zero. Completely blocking the beam is achievable, which has uses in various set-up and calibration procedures. Symmetry along the X=Y line is apparent and expected since the masks are identical.

function of a polynomial (see Fig 3.8 for a similar curve shape).

$$y = cos[ax + bx^2] \tag{3.1}$$

The recombined beams were then sent through a diagonal polarizer, allowing the two beams' interference to be detected. The combined beam is sent to the same power meter/photo-diode combination as the previous experiment. A LabVIEW program blocks all light from passing through the SLM. The program then allows light to pass through one pixel pair at a time, and records the data for signal vs. pixel number. The resulting graph is used to determine the position of the two beams in the pixel array. Based on this information two "windows" in the arrays can be set up. The rest of the array is set

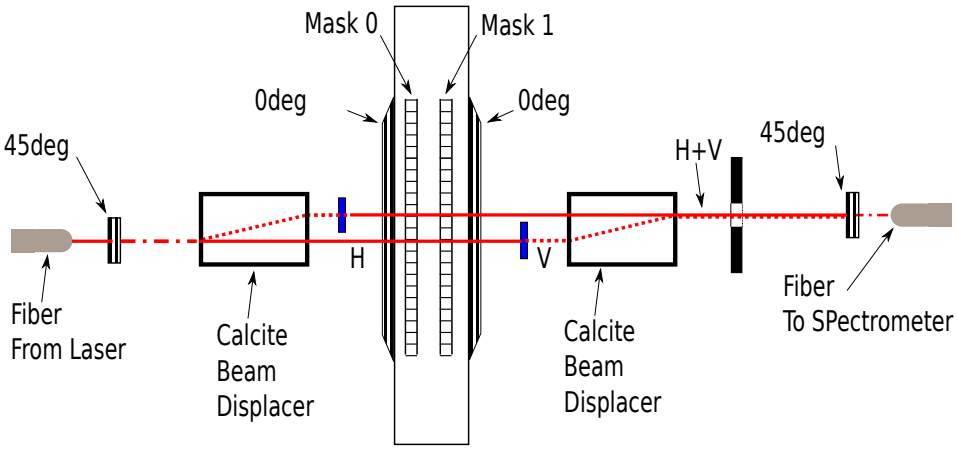

Figure 3.5: Setup For Phase Measurement With 808nm Diode Laser.

to maximum attenuation (different pixel values in mask 1 and 2) while the windows are individually set to a single value for both masks. The LabVIEW program then cycles through sequence of window voltage values with configurable start, end and step size. The intensity will then change primarily as a function of the difference between the window values but also slightly as function of the individual window values. The program records the data to a 2-D array and to a csv file. The array is displayed as a 3-D map in real time to assist in troubleshooting. The x- and y-axes of the map represent the pixel values at window 1 and 2 respectively, while the z-axis is the intensity of the signal.

3.4.3 Measuring Phase Modulation of a Pulsed laser

The third experiment is similar to the second experiment except that the monochromatic CW laser is replaced with broad bandwidth, pulsed, beam from the ML laser. To accommodate the larger intensity of this laser the adjustable linear polarizers are replaced with achromatic half wave-plates and polarizing beam splitters. The fiber connected to

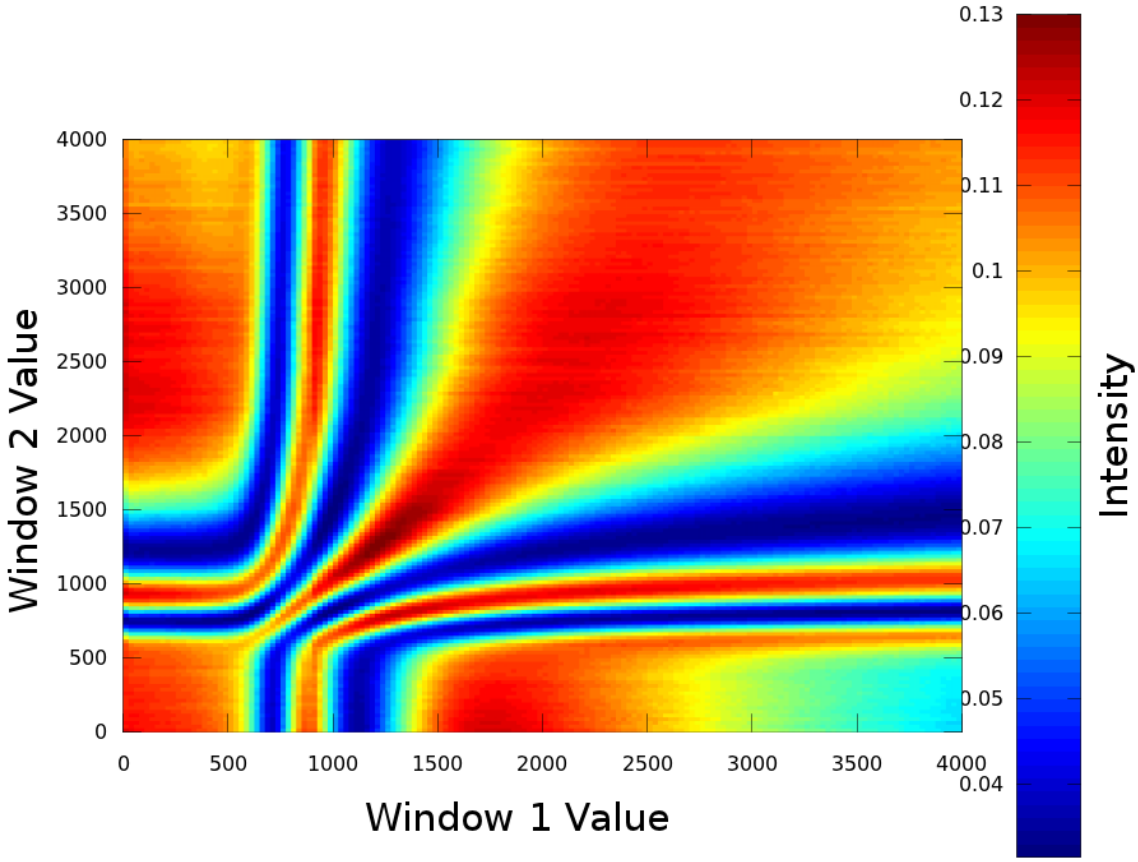

Figure 3.6: Monochromatic Phase Map For 808nm Diode
The phase map has a nearly identical shape to the attenuation map, but is slightly asymmetric. The troughs extending all the way to the extreme ends of the map suggest that phase modulation may be accomplished over a wide variety of settings.

the photo-diode in the second experiment is connected to a spectrometer (Ocean Optics USB4000). A peak-finding program is used to determine the pixel position of the two beams in the array. Using the the data from the second experiment, a suitable voltage value for the first window is determined, and the second window is cycled through a sequence of voltages with configurable start, end and step size. Fig 3.7 shows a sequence starting at 300, ending at 2499, with a step size of 3 voltage units. A LabVIEW program interfaces to and collects data from the spectrometer at each pixel value. The program records the data to a 2-D array and to a csv file. The array is displayed as false colour map in real time to assist in troubleshooting. The x axis of the map represents the voltage values at the varying window and the y axis represents the wavelength of light, while the z axis is the intensity of the signal. Results are discussed after the rest of the experiment

descriptions.

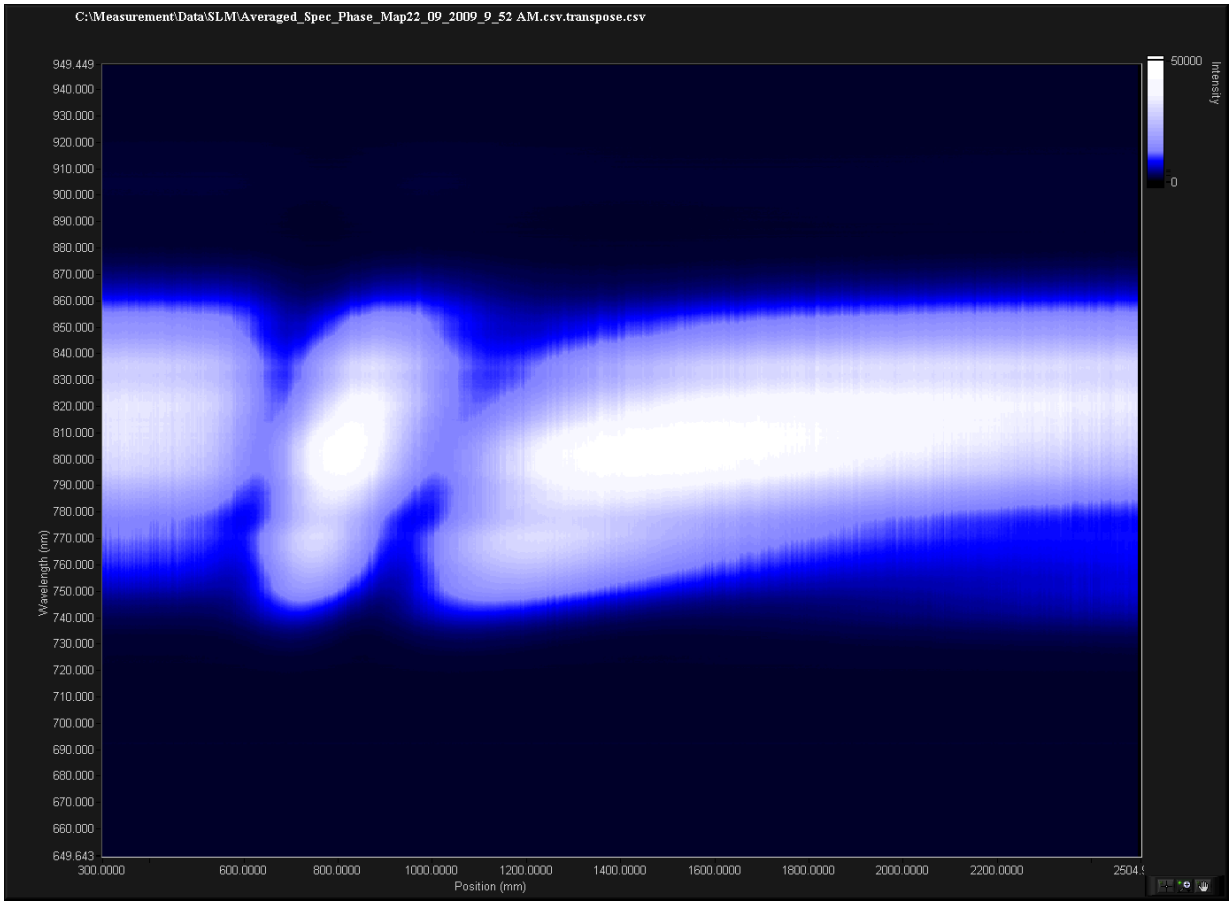

Figure 3.7: Phase Map For Broad Bandwidth ML laser
The slope of the minima troughs near pixel amplitudes 600 and 1000 shows that the phase modulation is wavelength dependent. The phase modulation varies more slowly at 860nm than at 760nm because the distance between the troughs is farther apart. The spectrometer was not sensitive enough to capture data at edges of the spectrum. The reduced visibility meant the fitting was less effective at the edges of the spectrum.

3.4.4 Phase Curve Fitting

The data for each wavelength was fit using an automated process because there were around 1500 curves to fit. A Mathematica notebook (co-written with Dr. R. Kaltenbaek, with guidance from Dr. K. Resch) first smoothed the data with a custom filter. The notebook then used a custom algorithm to find the maximum and minimum slope. The peak in between these was set as phase $\Phi = \pi$. An example of one of the curves with the

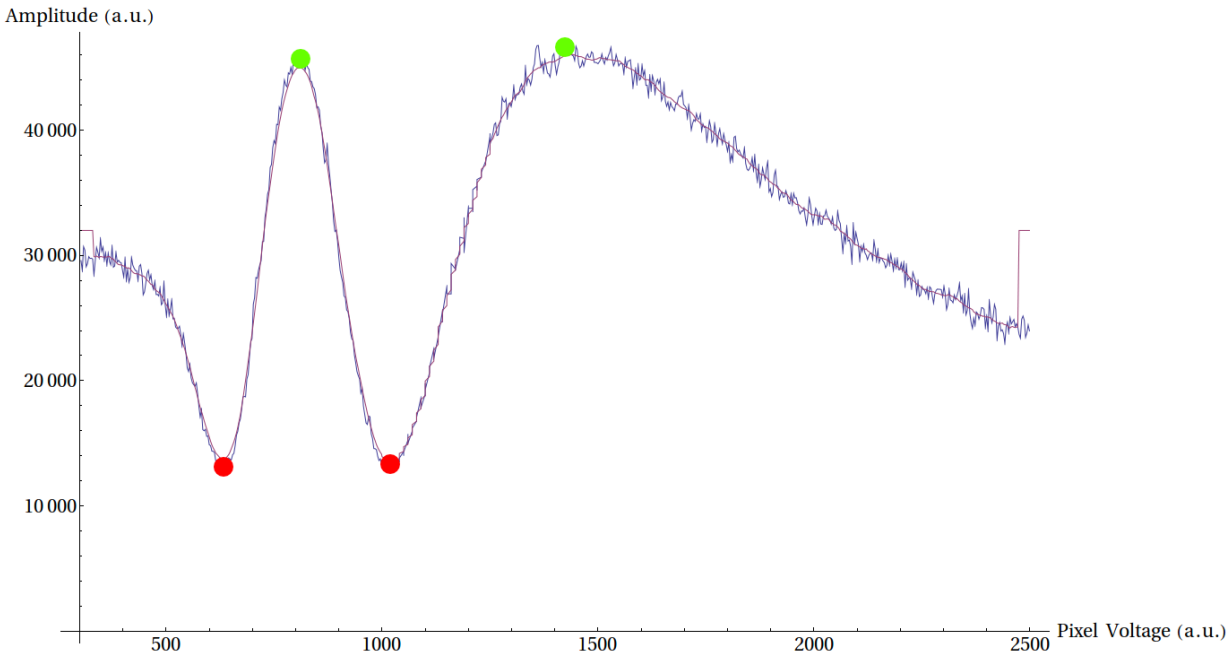

Figure 3.8: Example data with key points for fitting identified
The dots represent the maximums (green) and minimums (red). Based on those points the phase, amplitude, and offset can be estimated and used as starting points for the fitting routine. In this case the left maximum would be used set as $\pi - phase$ making the left minimum $0 - phase$

maximums and minimums identified is given in Fig 3.8. The raw data was then fit to the equation:

$$y = A + Bcos[Cx + Dx^2 + \Phi] \tag{3.2}$$

The LabVIEW program could then use the fitting parameters to determine "x", the voltage value needed to produce Φ phase in radians.

3.5 4-f Construction and Characterization

The ideal pulse shaper should not cause any additional modulation of the pulse other than what it is programmed to do. However the 4-f set-up used to separate the colours for insertion through the SLM is really just a pulse compressor set for zero dispersion. Small misalignment in the components of the 4-f can create unwanted dispersion and/or create wavelength dependent exit direction from the set-up, also know as spatial-chirp. For these reasons it is absolutely critical that the construction of the 4-f is done correctly.

3.5.1 Reference Beams and Periscope

The laser requires periodic maintenance, and this causes deflection of the beam exiting the laser. Steering mirrors placed several inches apart are used directly after the laser to align the beam to the optical table grid. We will refer to beams that travel directly along the lines of the grid as "reference beams" and use these extensively for alignment of the various components in the experiment. The beam exiting the laser is too low to enter the window of the SLM. It is possible to use the steering mirrors to correct this by deflecting the beam upwards but that would also potentially rotate the polarization of the beam, which is undesirable. Instead a periscope is used to raise the height or the beam. The beam enters and exits the periscope in the same direction, and only travels vertically in between the mirrors. This preserves the polarization of the beam, which is necessary to maximizes the efficiency of the system. The beam is aligned so that after exiting the periscope it passes though three irises, one directly after the periscope, one near the middle of the table, after the point where the beam exits the pulse shaper, and one at the far end of the table. Any time the beam becomes misaligned any 2 of these irises form the reference for realignment.

3.5.2 Entry and Exit Steering Mirrors

The PS requires the beam to enter and exit in mirror-symmetry at a specific, calculated angle. To establish this angle an optical rail is set up aligned to the beam exiting the periscope (Fig 3.9 A). Two carts are mirror-symmetrically constructed with mirrors place on horizontal rotary mounts. The mirror posts are actually mounted off center so that the front face of the mirror is at the center of rotation. Each mirror is placed at the far end of the optical rail and back reflected to the iris directly after the periscope (Fig 3.9 B). The scale on the rotary mount is adjusted so that this becomes "0 deg" (Fig 3.9 C). The input and output mirrors can now be adjusted to the precise angle required for the PS design, 51 deg and 129 deg respectively (Fig 3.9 D).

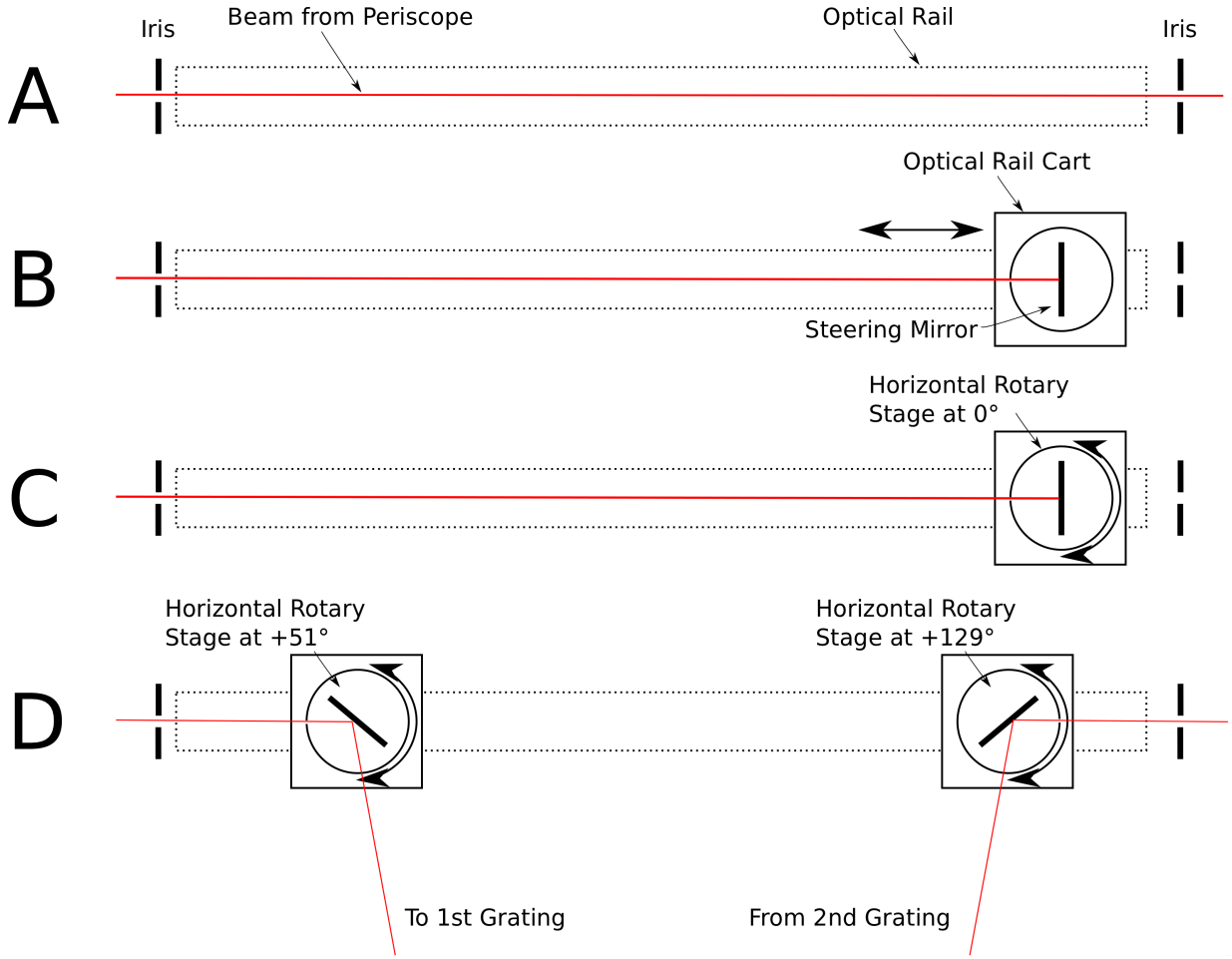

Figure 3.9: Steering Mirror Alignment
A) The optical rail is aligned to the beam. B) Each mirror is mounted on a rotary mount and cart and placed at the far end of the rail from the periscope. C) The mirror is aligned to back-reflect onto the iris. The rotary angle is set to 0 deg. D) The mirrors are adjusted to have mirror-symmetric angles and translated along the rail to align the input and output beams.

3.5.3 Prism Mirror Alignment

The prism mirrors form the basis for aligning the left and right halves of the pulse shaper in perfect mirror symmetry. This symmetry is important to remove unwanted dispersion and beam deformation from the pulse shaper. The prism mirrors are aligned by first back-reflecting a reference beam (aligned to the table grid) to an iris to ensure the mirror plane is orthogonal to the table plane (Fig 3.10 A).

The reference beam is back-reflected off the back faces of the prisms to ensure the top

of the mirrors are parallel to the table plane. The first mirror is then positioned so that a beam striking the center of the mirror is reflected at 90 deg along the same table grid line (Fig 3.10 B) as the first spherical mirror (which has been removed).

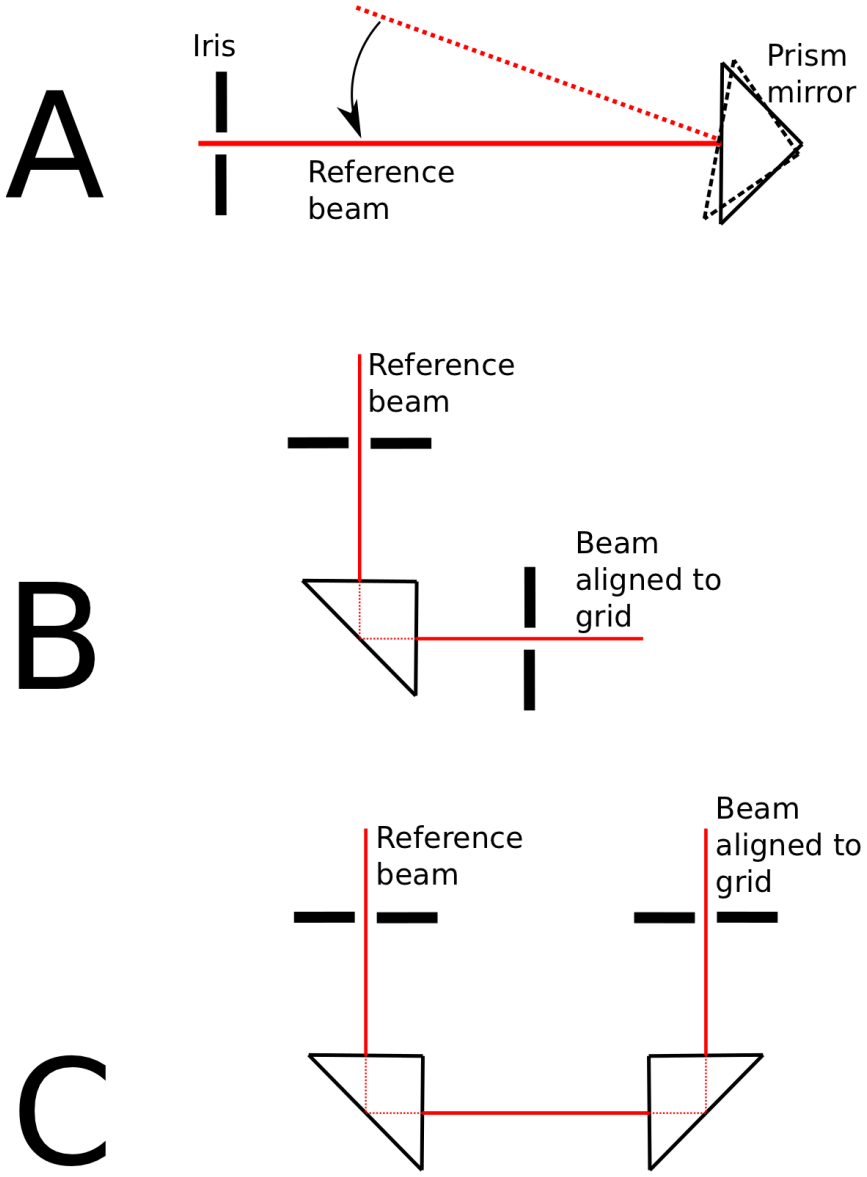

Figure 3.10: Prism Mirror Alignment
A) A reference beam is back-reflected off the face of the mirror, then the back faces. B) The first mirror is aligned so that a beam transmitted through the back of the mirror is aligned to the grid as well. C) The second mirror is positioned so that the transmitted beam is also aligned to the grid.

A reference beam is transmitted through the prism and reflected off of the back side of the mirror(Fig 3.10 C). The transmitted beam is aligned to the grid line and can be used to align the second prism mirror. The mirror is aligned so that the beam transmitted through the prism and striking the center of the back face of the mirror is aligned to the grid using two irises. The two mirrors are now aligned in perfect mirror symmetry.

3.5.4 Construction of the 1:1 telescope

The first step in telescope construction is aligning the mirrors to be parallel to each other and aligned to the reference grid on the optical table. A beam is aligned parallel to the plane of the optical table and at the center height of the SLM window. The first mirror is aligned for height and vertical tilt by reflecting the beam off of it at positions along the horizontal center line of the mirror. When the mirror is properly aligned the reflected beam will always be parallel to the plane of the table as well. Marking the mirror mount with the mirror center height on either side helps with alignment. The horizontal position and tilt are aligned in the same manner using a beam that is aligned along one of the reference grid lines on the table, and varying the angle vertically. It is usually uncommon to have beams travelling vertically due to safety concerns so great care should be taken to limit the propagation of the reflected beam.

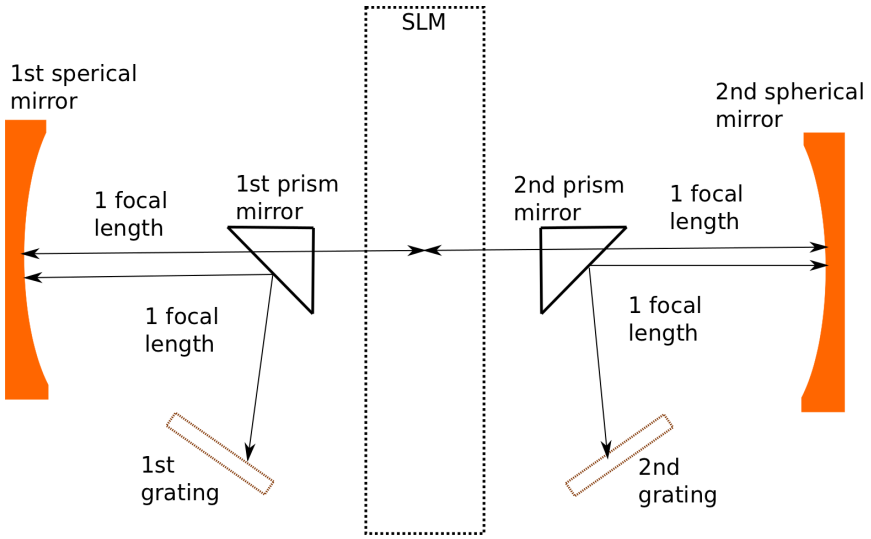

Figure 3.11: Prism Mirror Alignment
The grating→prism mirror→spherical mirror distance is 1 focal length. The spherical mirrors are aligned to the same central axis and are 1 focal length away from the center of the PS.

Once the first mirror is aligned it is positioned using translation stages so that the focal point of the mirror is centred on the SLM window. The second mirror is then aligned to

the table using a similar technique. The second mirror is then aligned to be exactly 2 focal lengths away from the first mirror. To check that the mirrors are correctly aligned a beam is reflected off of the first mirror and onto the second mirror. The reflection from the second mirror is then propagated over a few meters and the size of the beam is compare to the size of the beam not passing through the 4-f and propagating the same distance. When the mirrors are correctly aligned they form a 1:1 telescope so the two spots should be the same size with no focus in between. Equally important, the spots should be the same shape. If the two mirrors are not aligned to a common central axis the telescope will not be 1:1 in both axis and the spot shape will visibly deform after suitable propagation distance. Reference blocks are bolted to the table marking the position of the translation stages for the spherical mirror so they can be removed and replaced as required during construction of the rest of the 4-f.

3.5.5 Characterizing and Optimizing the Gratings

As discussed in the theory section, diffraction gratings are usually most efficient at the Littrow condition, and this angle is wavelength dependant. Efficiency curves for gratings are often quoted at Littrow, however the PS configuration requires the grating to be angled off of Littrow, and so it is important to characterize the effect of grating rotation. Ideally this would be done for all wavelengths present in our spectrum but this is complicated by the very diffraction we need the gratings for. The rapid divergence of the spectrum makes it difficult to collect all of the light in one sample for the spectrometer, but the power-meter has a larger aperture so it is possible to collect all of the diffracted light if the sensor is placed close to the grating. Let us define the relative angular efficiency as the efficiency for the whole spectrum at some angle θ relative to Littrow for the central wavelength in the spectrum. We make the assumption that while the absolute efficiency is a function of λ and θ the relative efficiency will vary primarily in θ.

The beam is put in CW mode and is sent though an iris to the grating. The grating is set up on rotary stages and rotated to back reflect onto the iris for the glass back face of the grating (effectively a mirror). This is used as the reference 180 deg position. The grating is then rotated to back the first order on the iris and this angle is the Littrow angle.

Table 3.1: Grating Efficiency vs Deflection Angle from Littrow condition (28 deg

Grating 1 Angle (Deg)	Efficiency	Grating 2 Angle (Deg)	Efficiency
3.5	95	3.5	94.5
7	95	7	91.6
9	90.9	9	89
10.5	88	10	88.4
15	72.73	15	77.27

Table 3.1 shows the grating efficiency drops as the angle of deflection from Littrow

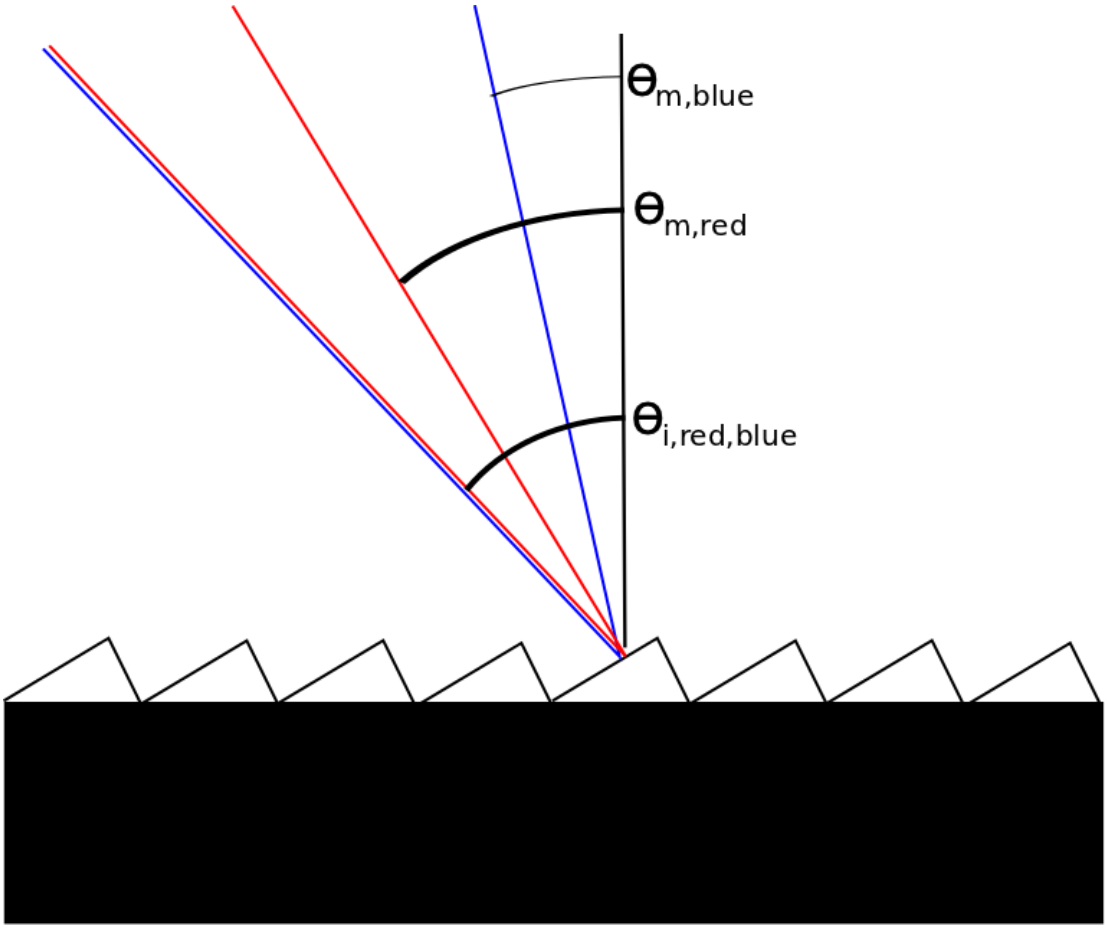

Figure 3.12: Diffraction Of a Multicoloured Beam.
The red end of the spectrum has a smaller angle of deflection from Littrow, and so will be closer to the maximum efficiency condition.

increases, so it is important to minimize this angle when deciding the grating and prism mirror locations.

Because the red (longer wavelength) end of the spectrum is diffracted at a larger angle than the blue end, it is deflected less from Littrow (Fig 3.12). Because of this we expect the red end to be more efficient, and when looking at the spectrum before and after the 4-f it is obvious that the blue end of the spectrum is attenuated compared to the red end.

3.5.6 Grating Placement and Alignment

Once the gratings have been characterized and the optimum angle determined, the gratings are placed into the 4-f setup. Initially the layout was planned to only use the grating,

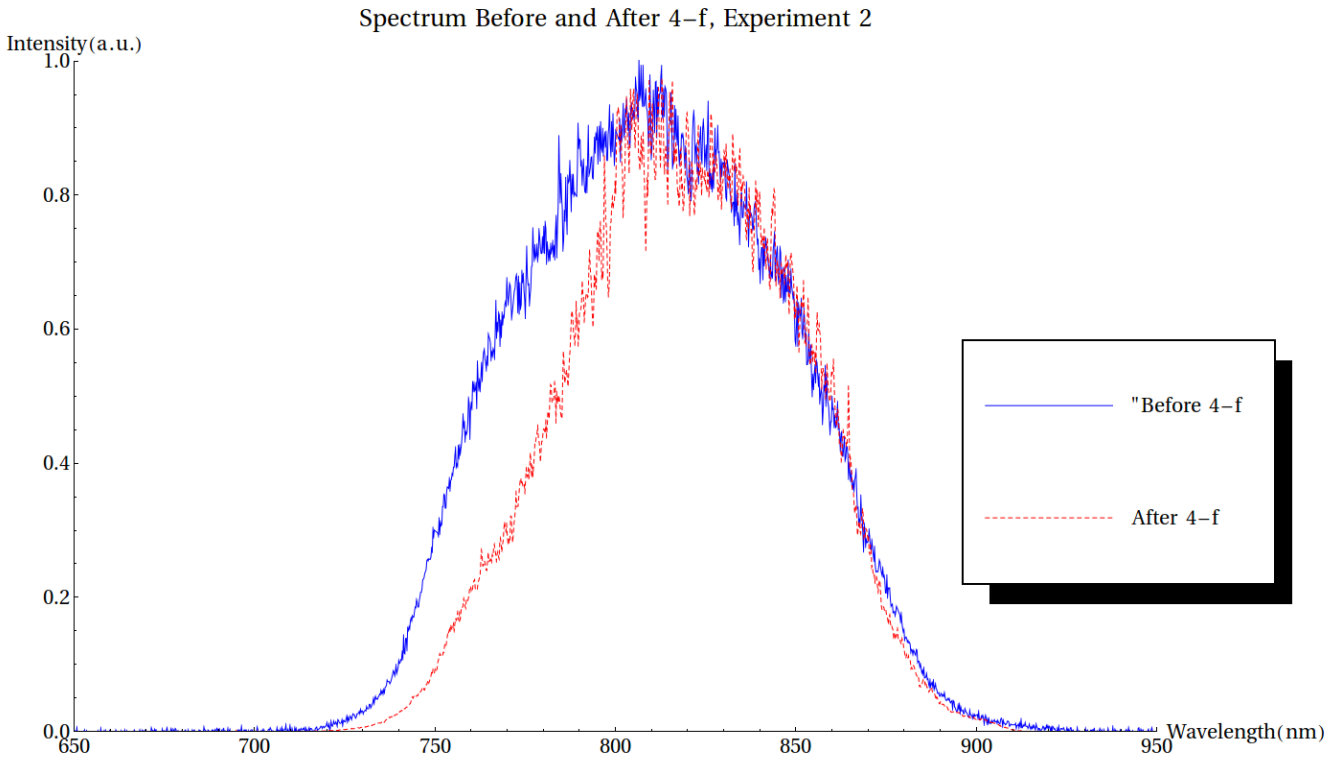

Figure 3.13: Spectrum before and after the Pulse Shaper.
Spectrum before and after the Pulse Shaper. The bandwidth is clipped at the low end of the spectrum due to the wavelength dependant efficiency of the gratings. The spectrum before the PS is centred near 800nm while the spectrum after the 4-f is centred near 810nm.

placing them outside the area between the mirrors (see figure). However this method created asymmetries in the beam and had poor efficiency. The layout was changed to include the addition of a prism mirror between each grating and spherical mirror pair. This layout is similar to previous designs[28].

The goal in positioning the grating and prism mirror is to choose a beam angle that places the input beam as close to the side of the prism mirror without clipping, then rotate the grating to place the edge of diffracted beam as close to the same edge of the mirror, while maintaining that the center of the diffracted beam is transmitted to the center of the spherical mirror at a 90 deg angle. This gets the red side of the beam as close to Littrow configuration as possible, maximizes the efficiency, and minimizes the bandwidth clipping due to the grating (see Fig 3.2).

Once the correct angles for the input beam are established, the next goal is to place the grating so that the optical path length from the grating to the prism mirror to the

spherical mirror is 8 inches, 1 focal length (See Fig 3.11). The beam must also be deflected upwards so that the beam reflected from the spherical mirror can pass over the prism mirror without clipping. The upward deflection must be as small as possible because this changes the effective focal length of the spherical mirror. This means the prism mirror should be placed as far as possible from the spherical mirror. The limiting factor is the prism mirrors must have room between them for the SLM. This was taken into account when placing the prism mirrors. The beam entering the 4-f is slightly lower than the center of the spherical mirrors, and the grating is tilted to direct the beam up so that it is at the center height of the SLM window when it reaches the first spherical mirror.

The first spherical mirror must then be tilted downward so that the reflected beam travels parallel to the plane of the table. The grating skew is then adjusted to make sure the diffracted beam produces a horizontal line after it is reflected from the spherical mirror. The grating is first translated laterally so that the beam is horizontally centred on a clean area of the grating. Next the grating is translated closer and closer to the prism mirror until the grating is at the focal point of the mirror. The entry mirror may need to be translated on the optical rail to maintain the alignment of the central wavelength to the center of the spherical mirror. A narrow bandwidth filter at the central wavelength is used to check that the beam is centred on the first spherical mirror.

The Second Mirror is removed and two sets of irises are placed at the center of the PS and further down the table. The grating is translated so that the light passing through the first set of irises forms two spots centred on the second set of irises. This means that the two beams are parallel and so the grating is correctly positioned at the focal point of the spherical mirror. The second mirror is replaced and tilted down by the same amount as the first spherical mirror. The second grating is placed laterally so that the spot is formed on a clean spot on the grating. The grating is tilted so that the beam reflected off of it is parallel to the table.

Next the grating is rotated so the entire spectrum is collinear after diffraction, undoing the diffraction from the first grating (See Figs 3.2 and 3.15). The grating is translated closer to the second prism mirror until the beam is re-collimated. The beam collimation is checked by propagating over a long distance and comparing the size and shape to a beam not passing through the PS. The exit mirror is translated along the rail so that the reflected beam is realigned to the irises which were previously used to align the beam out of the periscope.

3.5.7 Grating Fine Alignment

The gratings must be aligned in perfect mirror symmetry otherwise the beam will develop spatial chirp and/or angular chirp. Spatial chirp is characterized by unequal distribution of the spectrum in the beam; different wavelengths will be centred at different locations in the spot formed by the beam. Spatial chirp is caused by the gratings not being the

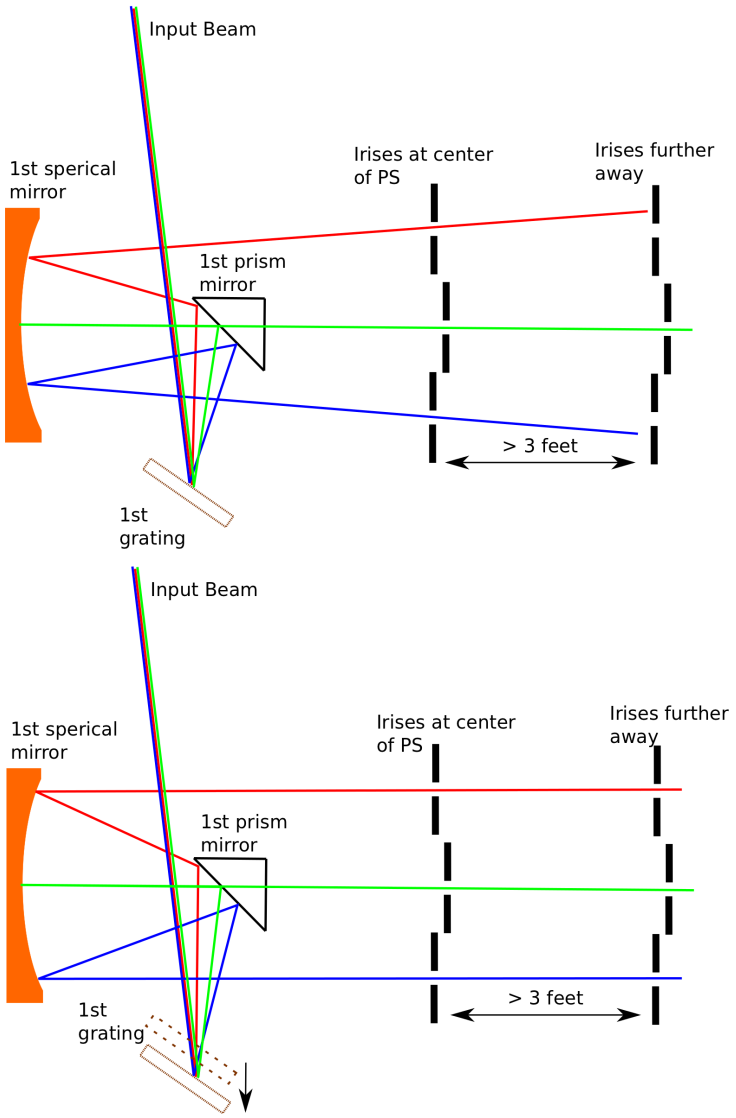

Figure 3.14: Focusing the first spherical mirror.
The upper diagram has the grating too close to the mirror. So all three beams cannot be centred on the far irises simultaneously. In the lower diagram the grating is moved out until all three beams are centred.

same distance from the spherical mirrors as the first. Angular chirp is when the different wavelengths in the beam are not collinear. Angular chirp is caused by the gratings having different rotation, tilt or skew.

It is not possible to detect whether the beam has angular or spatial chirp by looking at the beam at only one location. The beam must be analysed at two locations. Again a set of irises is placed at the center PS at opposite ends of the spectrum and the rest of the

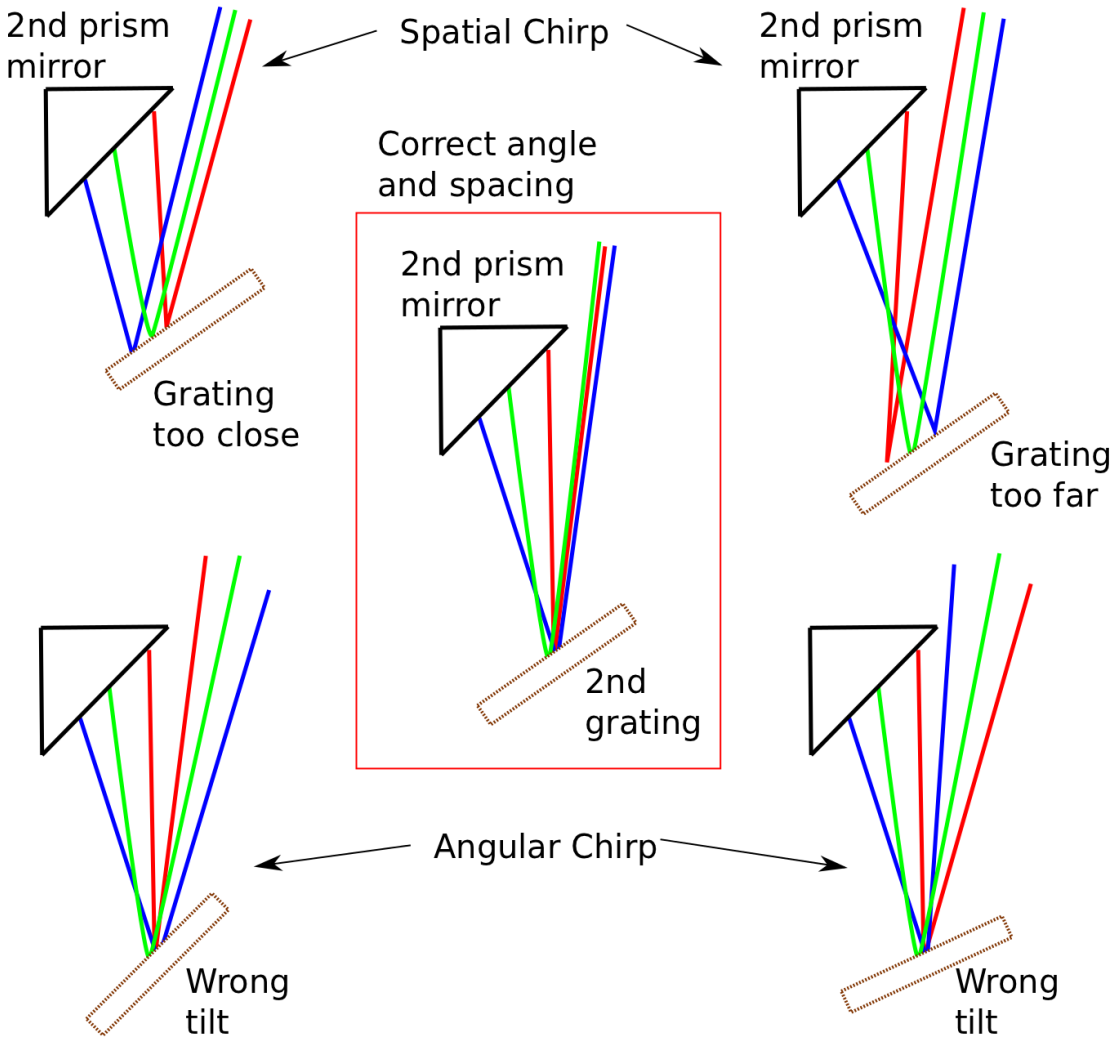

Figure 3.15: Grating Fine Alignment.
Incorrect grating spacing causes spatial chirp. Incorrect grating angle causes angular chirp.

spectrum is blocked, effectively forming a "band block" filter. A beam camera is mounted just after the exit mirror and two spots are observed, corresponding to the two ends of the spectrum. The camera mount is bolted down and the camera is removed to a second camera mount placed further away. The beam is reflected twice across the length of the table to provide a suitable propagation distance without leaving the table.

The spots produced by the beam at the further location will be larger and less intense, so the attenuation of the beam will need to be reduced. A filter wheel is mounted after the exit mirror before the first camera mount to simplify the switch between attenuation levels. The grating rotation is adjusted until the spacing between the spots is the same

at both camera locations. The camera is moved back and forth between the two positions between adjustments. The grating is then moved closer or further from the prism mirror until the two spots are overlapped horizontally, and the the grating skew is adjusted until the beams overlap vertically. Several rounds of adjustment may be required. When the two beams are overlapped at both camera locations the gratings are correctly aligned and the PS is ready for dispersion alignment.

3.5.8 Dispersion Alignment

The final step in aligning the PS is removing any dispersion caused by slight differences in alignment between the first and second halves of the PS that are too small to be corrected by the previous methods. To measure the dispersion an interferometer is built with one arm travelling through the PS (Fig 3.16). The SLM is placed into the PS and back reflected to the iris in front of the periscope. A 50/50 BS is placed between the periscope and the entry mirror. A second 50/50 BS is placed after the exit mirror. The BS are mounted on flip mounts so that they can be removed and replaced when required. The beams are recombined on the second beam splitter and sent to a spectrometer. Initially the spectrum recorded at the spectrometer will have a large number of fringes due to the dispersion caused by PS. By making small adjustment to the spacing of the mirrors, and the position of the gratings, the number of fringes are reduced. Eventually when the system is fully aligned, there are no more fringes in the spectrum. Placing a finger on the spherical mirror mount or the reference arm will cause a very small change in the path length and the entire spectrum will rise and fall as one.

3.5.9 Wavelength Calibration

Once the PS is mechanically aligned the software controlling the PS must be calibrated to determine which wavelengths are present at each pixel. The beam is sent through the PS to the Ocean Optics spectrometer. Using data from the previous experiments, a pattern is developed to provide maximum attenuation of the spectrum. A LabVIEW program records the spectrum with the attenuation masks and subtracts this background. The program then steps through the pixels one by one, changing the pattern at that pixel to maximum transmission. The spectrum forms a sharp peak at the center wavelength for that pixel, and is recorded at each step. Multiple runs are averaged to reduce noise. The data collected is processed by a separate LabVIEW program which detects the peak in each spectrum and creates a graph of pixel vs peak wavelength. After removing the noisy data from the outer edges of the spectrum, a clear trend in the data becomes visible. The data is fit with a simple equation $y = ax + b$ and the values are extrapolated to all 640 pixels. A LabVIEW program takes the array of phase modulation data generated earlier and makes a new array with the specific values for each pixel wavelength. The new array is recorded to a .csv file for use by the SLM control program.

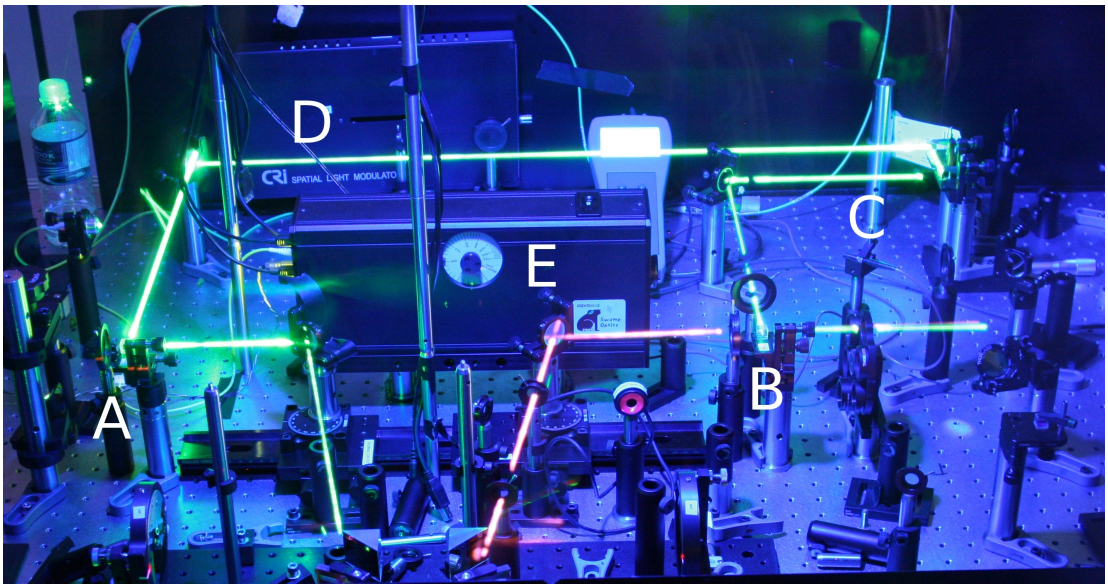

Figure 3.16: Interferometer for Dispersion Alignment.
BS's at A and B separate and recombine the beam. The green path near the top of the photo is the reference arm (C), with the path delay adjustment in the top right corner. The green beam is due to the camera being more sensitive to the mall amount of pump light leaking out of the laser. The SLM (D) and FROG (E) can also be seen. The SLM was removed for this photo but was present during alignment.

3.6 Frog

Ultra-fast laser pulses are so short that most detectors are too slow to measure them [6, pg 457]. Something must gate the detector to improve the time resolution. The pulse itself is a suitable item for this task [27, pg 4]. An auto-correlator is a device that contains an interferometer where the paths recombine at a non-linear crystal [27, pg 65]. The up-converted light is measured as a function of the path difference and the signal is the autocorrelation function for the pulse. The width of the signal is proportional to the width of the pulses electric field so this method can be used to measure the pulse duration [27, pg 75].

An auto-correlator is a very rough tool and really only gives information about the duration of the pulse, to recover more information, a tool know as a Frequency Resolved Optical Gating (FROG) is used [27, pg 4]. The FROG is really an auto-correlator where the signal spectrum is analysed instead of just the power. The information is analysed with an associated algorithm and the phase information for the pulse can also be reconstructed [27, pg 4].

In the lab our FROG is a commercial unit (Swamp Optics model USB 8-9), and a

control program (QuickFrog). The beam is aligned to enter the iris and the control program provides a variety of information including the raw data (an intensity plot for wavelength vs time delay), a second intensity plot for the reconstructed pulse (which should be the same), and graphs of the field and phase vs spectrum and time delay.

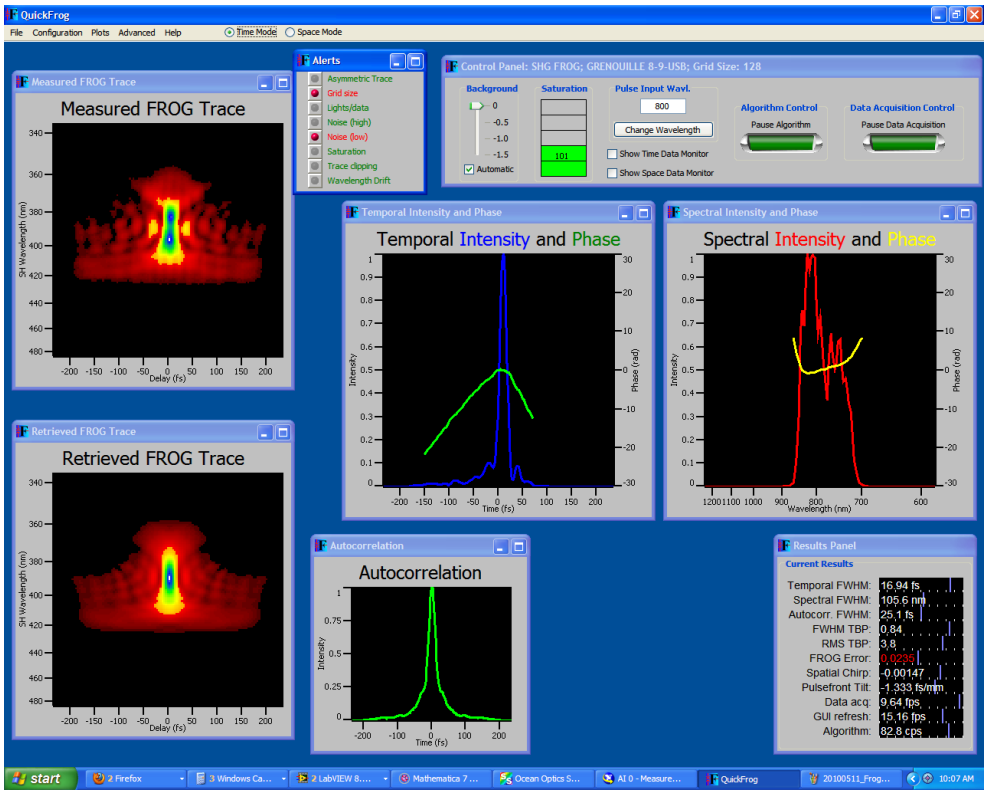

Figure 3.17: Example of the QuickFrog software and a 16.94fs pulse.
The temporal intensity trace (Blue) is usually a good indicator of what the CPI trace will look like. Specifically side lobes in this trace will cause similar lobes in the CPI trace.

Using this information the pulse can be modified and the effects of the modifications can be quickly analysed.

3.7 Pulse Compression

As a final test of the pulse shaper, and as a first step in creating the CPI pulse, the PS is used to compress the pulse as short as possible. The beam is directed from the PS to the FROG, and the QuickFrog software is used for feedback. A LabVIEW program controls the pulse shaper (See Fig 3.18). The program takes an array with four columns as input. The first column is an amplitude in units of fs raised to an appropriate exponent depending on

the type of dispersion to be compensated (fs^2 for second order dispersion etc.). The second column is a function of two variables, ω and $\omega 0$, representing the frequency equivalent of the center pixel wavelength and spectrum center wavelength respectively. The third and fourth column represent the first and last pixel to apply the function over in the pixel array. This is useful for applying small corrections to specific parts of the spectrum.

The FROG pattern is observed and a small positive amount ($200fs^2$) of 2nd order dispersion is added at the center wavelength of the input spectrum, causing the pattern to become narrower in time. More second order dispersion is applied until the pulse is short enough to be properly measured by the FROG, typically less than $100fs$. The temporal and spectral FWHM of the pulse are observed, and more second order dispersion is added as long as the temporal FWHM continues to decrease without significantly affecting the Spectral FWHM. When no further gain is possible, the center wavelength of the dispersion may be adjusted in increments of $0.1nm$, attempting to further compress the pulse. Third order dispersion is added next, starting with approximately 10% of the second order value. The sign may need to be adjusted on the third order term. More third order is added until no further gain is achieved. Next the FROG's temporal and spectral traces are observed. The data in these windows are generated based on the estimate of the electric field by the FROG algorithm. Ideally the spectral trace will be identical to the input spectrum, but typically it is noisier with at least one large negative spike in the middle of the spectrum, which can confuse the fitting routine used to establish the spectral FWHM. The temporal trace should ideally look like a single smooth Gaussian peak for a transform limited Gaussian pulse, but typically has a few side lobes. Both windows also superimpose the phase in radians as a function of time and spectrum respectively. For a transform limited pulse these would both be flat lines at zero. Typically at this point in the compression process the spectral phase graph looks like either a second or third order polynomial curve, with discontinuities or jumps in the curve. By applying small amount of second or third order dispersion over small sections of the pixel array the discontinuities can be reduced, and the temporal FWHM of the pulse will also be reduced. When the pulse length is within 150% of the theoretical value based on the FWHM of the input spectrum, further reduction of the pulse length becomes particularly difficult so it is not pursued.

Using this method the pulse was compressed to under $17fs$ with sufficient bandwidth, but usually it was only compressed to around $21fs - 24fs$ for most experiments. Fig 3.17 shows the pulse compressed from an initial duration of over $100fs$ to $16.94fs$, with an input bandwidth of $106.4nm$, centred near $810nm$. The transform limit for a Gaussian pulse with these parameters is around $12.7fs$ so the pulse is getting very close to this limit with only first and second order compensation.

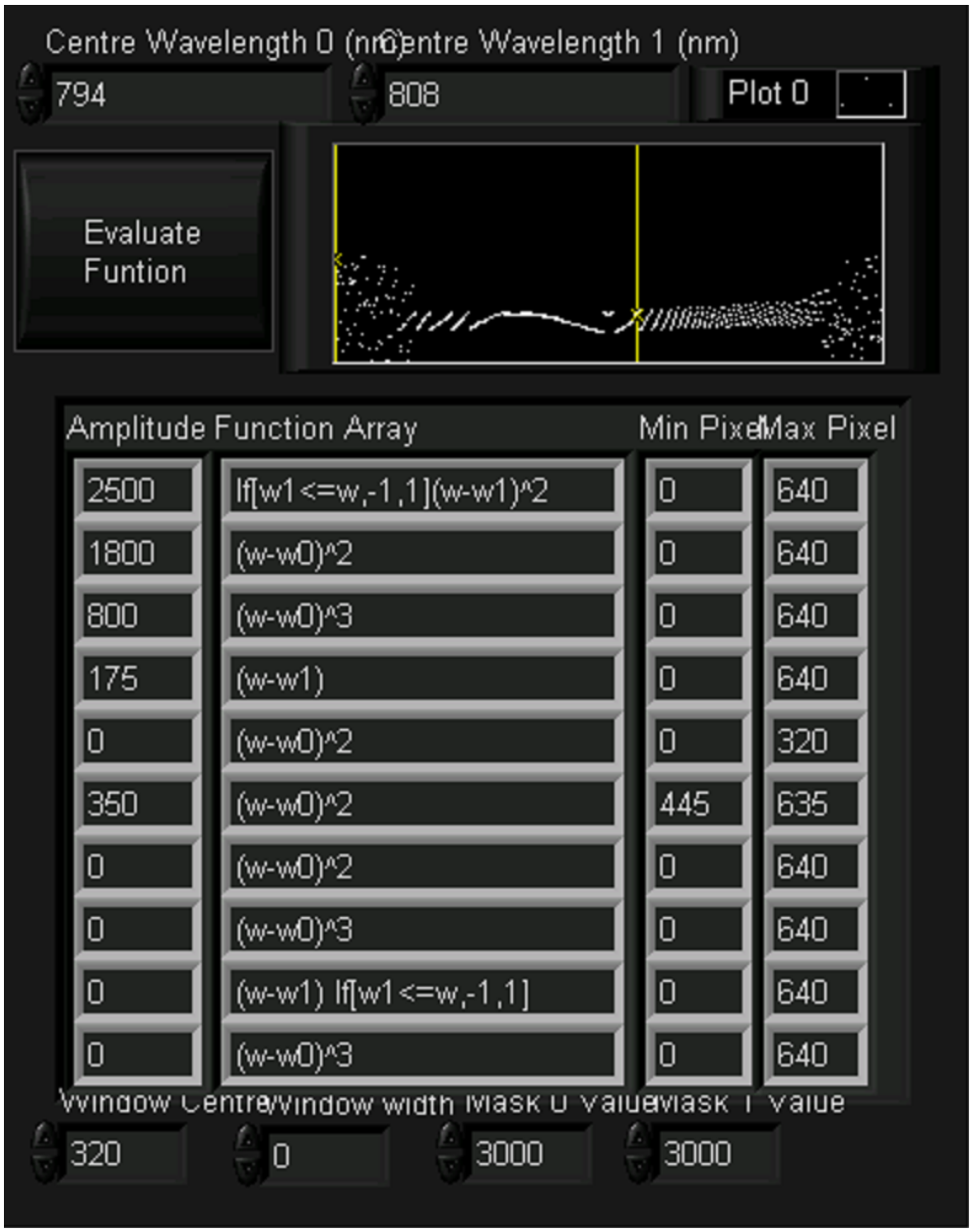

Figure 3.18: SLM Control Interface
The array of strings represent the various forms of dispersion and their amplitudes and ranges. The graph shows the value at each pixel.

3.8 Discussion

The results show that the SLM is capable of attenuating the signal down to zero, and the phase can be modulated over more than 2π radians for all wavelengths present in the

spectrum. This means that it is possible to produce the CPI phase function. The SLM control program allows the chirp function to be directly input into the program making it easy to use to test theoretical chirp models.

Chapter 4

Interferometer Design and Compensating 2nd and 3rd order Dispersion

4.1 Introduction

As the name suggests, Chirped Pulse Interferometry needs an interferometer. The interferometer must be able to resolve small features, but scan quickly and over distances very large relative to the resolution. Another aspect of CPI that needs to be accounted for is the large bandwidth of the pulse, meaning optics must be achromatic whenever possible. The large bandwidth ironically also makes the system more susceptible to dispersion, so dispersive components should be avoided or minimized whenever possible. Unlike an OCT interferometer, a non-linear interferometer uses a non-linear crystal as the interference medium. This means the beams must be focused to a small size to achieve the required intensity, and the system becomes much less tolerant of misalignment.

4.2 Initial Interferometer Design

The initial interferometer 4.2 was based on the system used in the previous CPI experiment [13], with attempts to accommodate the much large bandwidth of the new laser used in this experiment. The interferometer used polarizing beam splitters and achromatic wave-plates to separate the input and output beams at various stages in the system. A half-wave-plate before the interferometer rotated the beam polarization from horizontal to some combination of horizontal and vertical. A polarizing beam splitter directs one polarization to the sample arm, and the other to the reference arm. This setup had the advantage that the power sent to the sample arm was completely adjustable. The sample and reference arms were equipped with identical setups to differentiate the input and output beams.

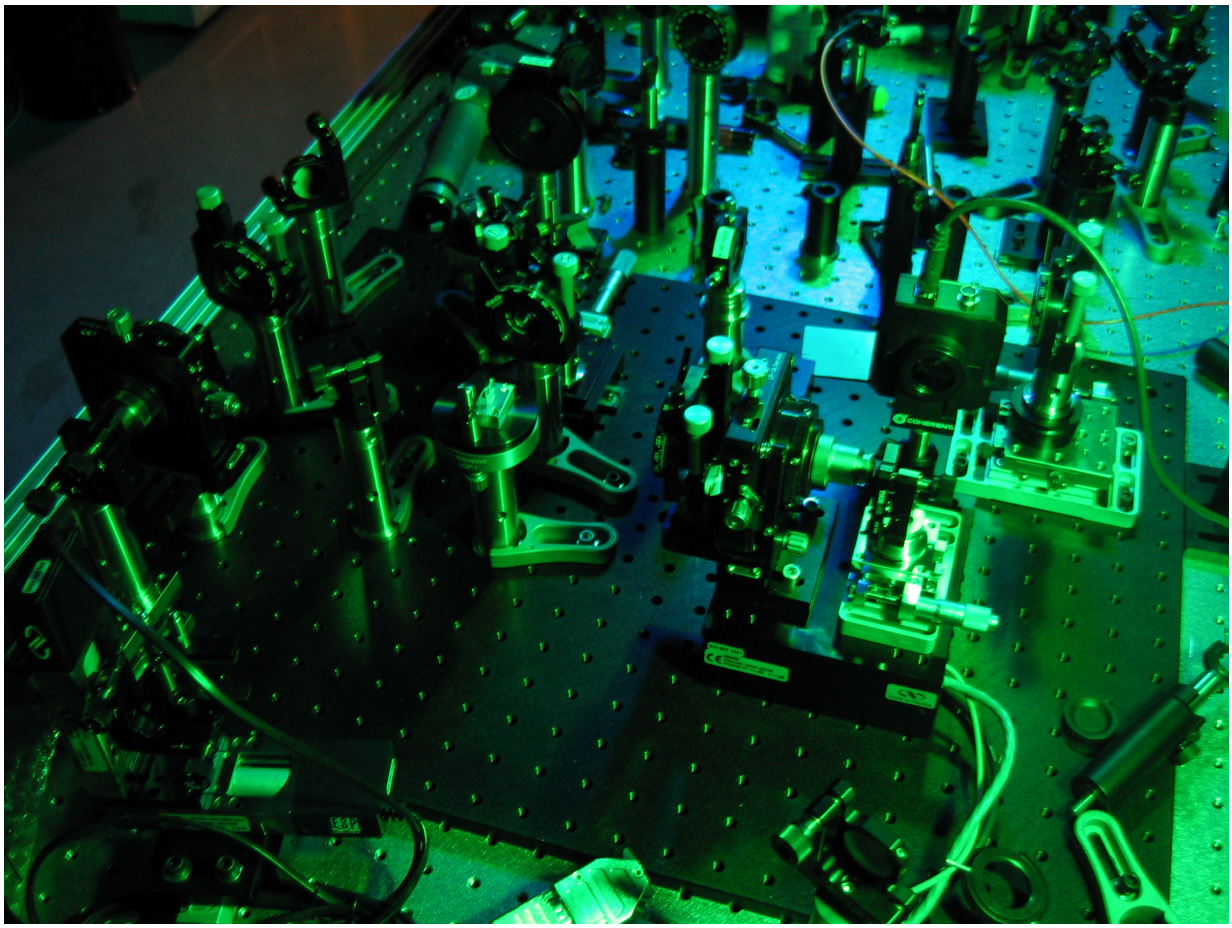

Figure 4.1: Photo of the initial interferometer design with achromatic wave-plates

An achromatic quarter wave-plate was placed before the sample and reference arm mirror, and the effect of double passing through the quarter wave-plate was to rotate the beam's polarization from horizontal to vertical or vice versa, meaning the beam would be reflected (transmitted) back through the PBS that just transmitted (reflected) it, or vice versa. This meant the efficiency should have been very high and this system worked well in the previous CPI experiment. However a problem was encountered due to the larger bandwidth from the new laser. The wave-plates were not perfectly achromatic, which resulted in either the ends or the center of the spectrum polarization left incompletely rotated, changing the shape of the spectrum, reducing the effective bandwidth and causing the CPI signal to broaden. In hindsight this should have simply been accounted for when analyzing the data, but a decision was made to pursue a set-up that did not rely on achromatic wave-plates.

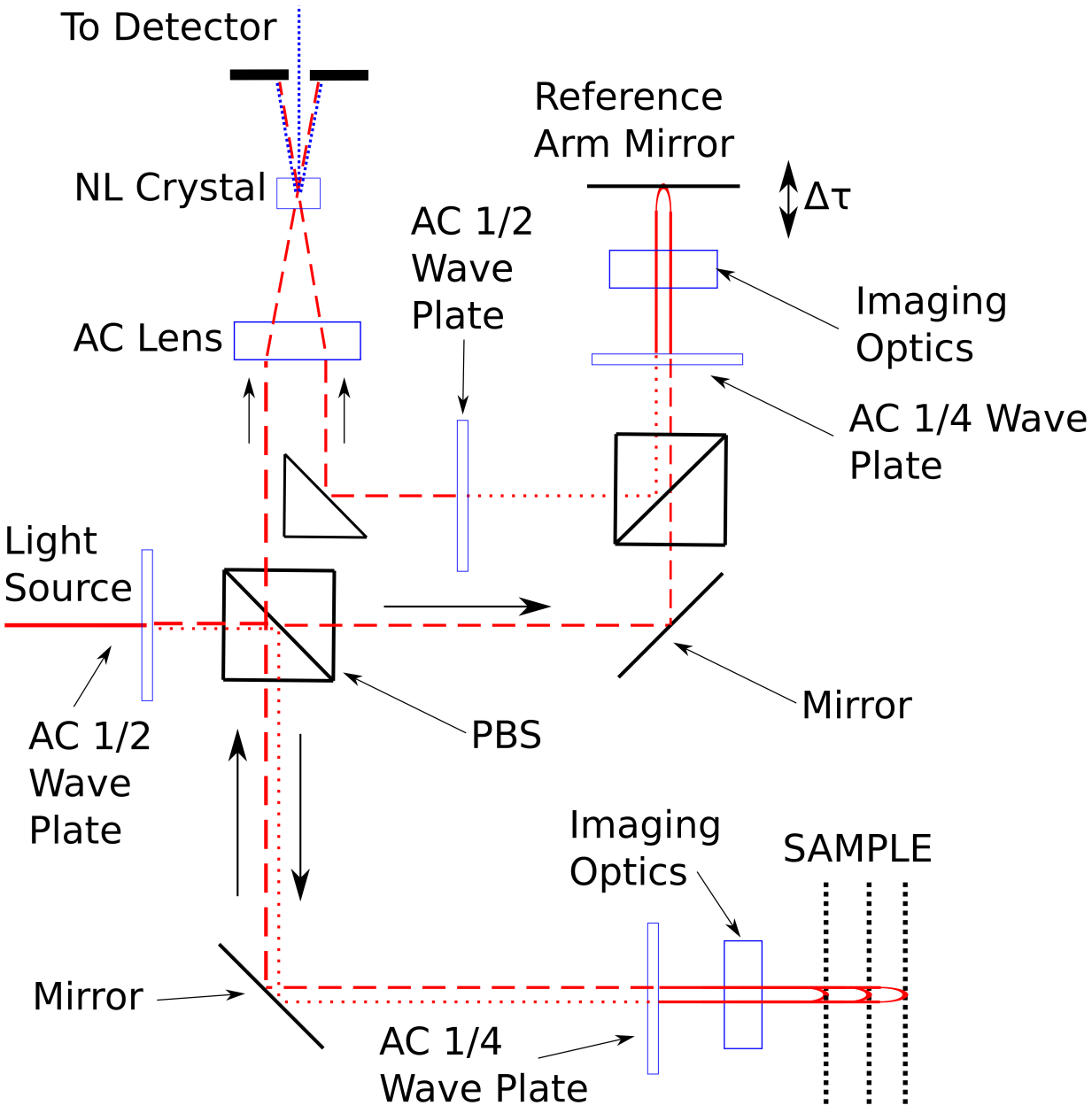

Figure 4.2: Initial Interferometer Design
Using PBS and wave-plates provided better efficiency, but created issues with uneven polarization rotation.

4.3 Final Revision

The interferometer uses a low dispersion beam splitter (Femtolasers 0A89 605-950nm) to reflect up to 37% of the light to the sample arm. The beam splitter (BS) is mounted in a 1" lens mount and may be substituted to achieve different ratios. The BS is mounted on two translation stages and a mirror tilt-mount so that it can be aligned with the incoming beam. The sample arm has a linear motor (Newport LTA-HS) travelling parallel to the beam path. For biological scanning a gimbal lens mount was attached to the motor providing all required degrees of freedom for lens alignment. For the early experiments the lens is removed and a mirror is mounted to the motor, back reflecting the light through the beam splitter. The light travels through the beam splitter to the primary lens, which focuses the light onto the crystal.

The light that is initially transmitted though the BS is sent to a polarization maintaining retro-reflector (Edmund Optics part number H64187). The retro-reflector is mounted to a linear translation stage travelling orthogonal to the beam path and parallel to the table. The translation stage is mounted to a high speed linear motor (Newport XMS50) travelling parallel to the beam path. The retro-reflector sends the beam back toward the beam splitter, but shifts the beam laterally and down. A prism mirror directs the beam parallel to the sample beam, towards the primary lens. The prism mirror is mounted on a translation stage to allow the distance between the reference and sample beams to be adjusted. The primary lens is a 75mm achromatic doublet (Edmund Optics NT65-439) and is mounted on a translation stage travelling horizontally and perpendicular to the beam path. The lens is centred between the sample and reference beams so that each beam travels an equivalent optical path through the lens. This ensures balanced dispersion between the beams. The lens focuses on the non-linear crystal (Newlight Photonics BiBO $5x5x2mm^3$ $\theta = 152.4\,\text{deg}$ $\phi = 90\,\text{deg}$), which is mounted on XYZ translation stages. An adjustable iris and UV lens are mounted to a separate XYZ stage mounted on top of the crystal stages. This allows us to fine tune the focus of the UV lens relative to the crystal. The iris is used to spatially filter the IR light transmitted though the crystal as well as any up-converted light generated independently by the sample or reference beams. A BG37 filter is used to remove even more of the IR. Two steering mirrors direct the beam to a spectrometer (Acton Advanced SP2750A).

The spectrometer is equipped with a camera (PI-Acton model Pixis 2K) and a monochromater output (See fig4.4). A computer controlled mirror switches between camera and monochromater function.The spectrometer is also equipped with 3 gratings on a motorized turret. A six position motorized filter wheel is loaded with 5 neutral density filters (1,2,3,4,0.5 at positions 1-5 respectively) and position 6 is left empty.

A photomultiplier tube(PMT) (Hamamatsu H7827-002) is mounted outside of the spectrometer, after the monochromater slit. The PMT is connected to a dedicated power supply which controls the gain. The PMT is also connected via BNC cable to an analog input card (National Instruments PCI-6281).

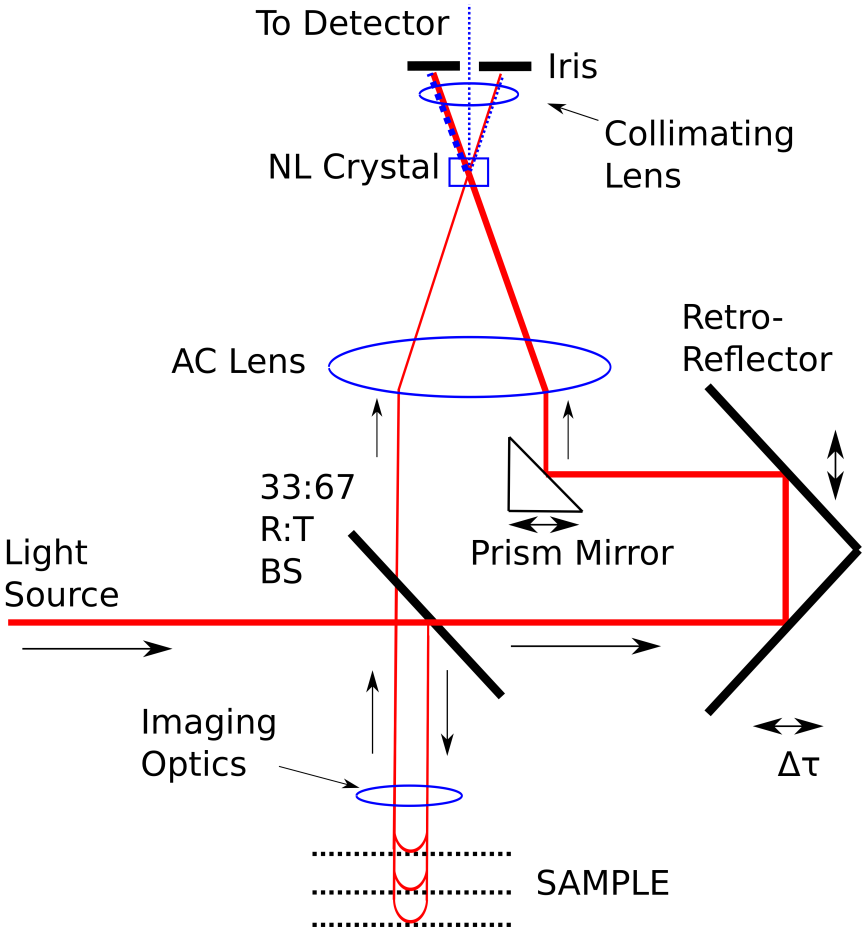

Figure 4.3: Diagram of the Final Interferometer Design.
The beam is separated at a 37:63 beam splitter. The transmitted portion is the reference arm. The sample arm is reflected directly back along the same path, and 67% is transmitted to the non-linear crystal. The beams are combined crossing each other. Only the cross-SFG beam is able to pass through an iris, providing spatial filtering.

Because the PMT has an analog connection the scanning rate is not limited by it, but rather by the maximum speed of the motor ($200mm/s$ for $0.5\mu m$ data spacing). On the other hand the spectrometer-computer interface requires the motor to stop at each scanning position, and this makes the spectrometer much slower than PMT for scanning

4.3.1 Constructing the interferometer

The first step in constructing the interferometer is to mount the retro-reflector and motor to the table, and align the incoming beam to the reference arm motor. Normally a beam is aligned to the table, and components are aligned to the beam, but this does not make

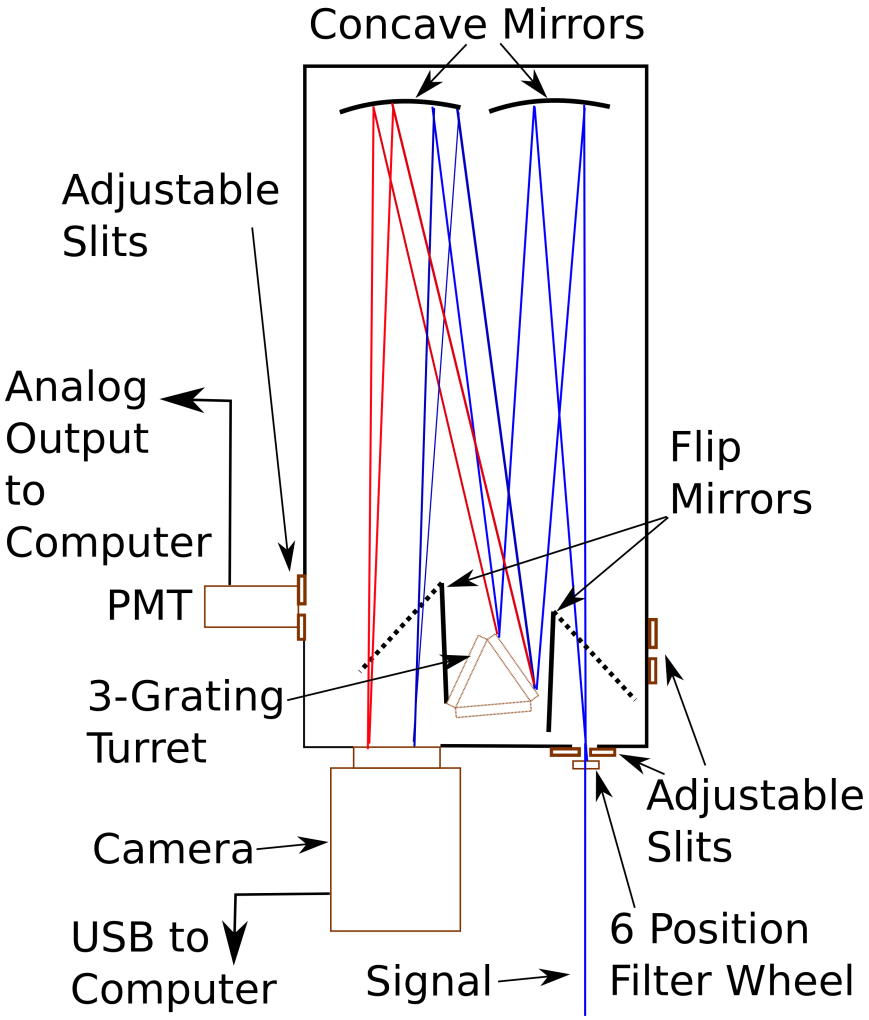

Figure 4.4: Diagram of the Spectrometer and PMT.
The beam enters through an adjustable slit, and a filter wheel provides attenuation if required. A flip mirror directs the diffracted light to either the spectrometer camera, or to a monochromater slit for the PMT. An motorized grating turret is used to tune the wavelength for the monochromater.

sense in this case. The retro-reflector is accurate to less than 0.86arcsec across its entire face, so the output beam will always be parallel to the input. However, if the beam is not aligned to the travel of the motor, the position of the input beam on the face of the retro-reflector will change as the motor travels, and the spacing between the input and output beams will change, causing misalignment further down the beam path.

The beam camera is used to align the beam to the beam path. The motor is set to one end of its travel and the position of the output beam is marked on the camera. The motor

is then moved to the opposite end of its travel and the position of the beam is compared. When the motor moves from near to far, the input beam must be adjusted in the opposite direction it travelled on the camera. When the motor moves from far to near the input beam must be adjusted to move the spot in the same direction it travels on the camera. The process is repeated until the spot does not move when the motor moves.

After the input beam is aligned the BS must be aligned to the sample arm motor. The camera is placed on the sample arm motor and translated back and forth. When the camera moves from near to far, the BS must be adjusted to move the spot in the opposite direction it just travelled and vice versa when the motor moves from far to near. This step is absolutely critical when using an objective lens to make sure the beam and lens stay aligned during scanning.

The camera is removed and a mirror is mounted on the motor. The primary lens and crystal are removed and the camera is placed after the crystal position. The mirror is aligned in a method similar to the previous examples. This ensures that the sample beam will have a constant location and direction at the primary lens.

Next the prism mirror in the reference arm must be aligned to make the reference beam parallel to the sample beam. The camera is set-up to be precisely repositioned between two locations after the crystal. At each position the camera can be translated vertically between two positions with equal spacing at each location. The camera is placed in the near, high location and the position of the sample spot is recorded. The camera is set to the low location and the position of the reference arm is recorded. The camera is the repositioned at the far, high location and the measurements are repeated. the difference between the sample and reference spot positions should be equal both near and far. If not the reference prism mirror is adjusted to compensate and the measurements are repeated.The process is repeated until the two beams are parallel.

The reason the two beams must be parallel is a matter of non-linear efficiency. The CPI signal is strongest when the electric field intensity is at its maximum for both beams at the same location. Ideally both beams will be focused at the same location. If the beams are not parallel they may cross, and a signal may be produced, but the beams will not be focused at the same location so the signal intensity will be reduced. Once the beams are parallel the primary mirror is mounted and the positions of the two beams are checked to be equally spaced from the center of the lens. The lens is adjusted if required.

The non linear crystal must be calibrated to determine the position of the optical axis. The crystal is placed in a tilt and rotation mount between two crossed polarizers and rotated to minimize the signal. The angular location of the minimum is recorded as zero degrees. The crystal and mount are moved to the XYZ stage and mounted in the interferometer. The crystal is initially tilted to cross-reflect the beams off of the crystal face. The crystal is translated near but not all the way to the focal point of the primary lens. A LabVIEW program continuously translated the reference motor back and forth and the CPI signal after the BG37 filter is observed on a white card. If the signal is difficult to

detect, a few hundred fs^2 of dispersion may be added to the SLM to broaden the pulse. Because the crystal is not at the focal point, the electric field will be less intense but each beam's area will be larger, increasing the chance that the beams will overlap in the crystal and create the CPI signal. Once the CPI signal is detected, the distance the motors travel can be reduced, but not to zero. The crystal adjustment process will introduce slight variations in the path lengths,and the signal may be lost if the motor does not oscillate. The added dispersion is removed and the crystal is tilted in the phase matching direction to maximize the signal intensity. The crystal is translated closer to the focal point and if the signal is reduced, slight adjustment of the reference arm prism mirror may be made to maximize the signal. The phase matching angle may then be adjusted again to maximize the signal. The process of translating the crystal, aligning the beams, and aligning the crystal is continued as required. When the process provides no further gain, the motor is stopped and moved to the peak signal location. The card is removed from the beam path and the signal is steered into the spectrometer to maximize the signal. Typically the 1600 lines/mm grating is used because it provides the finest resolution of wavelength. The slit is closed to approximately $10\mu m$ and the filter will typically be set to the highest attenuation due to the strong signal from the mirror. A LabVIEW program continuously reads the spectrum and outputs the data in a graph of intensity vs wavelength. The program fits a Gaussian function to each peak in the spectrum in real time and provides the amplitude, FWHM and central wavelength for each peak. This data can be used to further align the system.

4.4 Compensating 2nd and 3rd order dispersion in the interferometer

At this point the SLM control should contain only the compensation terms required to compress the pulse before entering the interferometer. Both arms of the interferometer travel through the primary lens which is very thick because it is a short focus achromatic doublet.This mean the pulses will experience significant dispersion which must be compensated. As a further test of the pulse shaper calibration, the required compensation can be estimated based on the path through the lens and the two lens materials.

As an approximation we assume the beams pass straight through the center of the lens. Thus the 2nd order dispersion is simply calculated as the sum of the dispersion for each lens' material multiplied by the thickness of each material at the lens center

$$D_2 = \frac{d^2k_1(\lambda_0)}{2d\omega^2}L_1 + \frac{d^2k_2(\lambda_0)}{2d\omega^2}L_2. \tag{4.1}$$

The primary achromatic doublet has a focal length of 75mm (Edmun Optics NT65-439). Based on the manufacturer's specification material one is N-Lak14 with a center

thickness of 16mm and material 2 is N-SF66 with a center thickness of 6mm. Using the Sellemier coefficients the dispersion terms were calculated to be

$$D_2 = 0.096478\frac{fs^2}{\mu m} \times 16000\mu m + 0.0341759\frac{fs^2}{\mu m} \times 5000\mu m \tag{4.2}$$

giving a final answer of

$$D_2 = 1362.45fs^2 \tag{4.3}$$

.

The 3rd order term can be calculated similarly using the same Sellemier coefficients. Following the same method the 3rd order dispersion is

$$D_3 = \frac{d^3k_1(\lambda_0)}{2d\omega^3}L_1 + \frac{d^3k_2(\lambda_0)}{2d\omega^3}L_2 \tag{4.4}$$

which becomes:

$$D_3 = 0.0307651\frac{fs^3}{\mu m} \times 6000\mu m + 0.0118434\frac{fs^3}{\mu m} \times 16000\mu m \tag{4.5}$$

giving a final answer of :

$$D_3 = 374.085fs^3 \tag{4.6}$$

.

So the total estimate for 2nd order dispersion is $D_2 = +1362.45fs^2$ and for 3rd order dispersion is $D_3 = +374.085fs^3$. The value entered into the SLM to properly compensate the pulse in the SLM control is $+1328fs^2$ for second order, so this confirms the pulse shaper is working as expected (See Fig 5.7). On the other hand the value entered for third order is only $+263fs^3$ (30% less than expected), however third order chirp has a smaller effect on pulse broadening so it may be that the difference was too small to notice. A note on sign, the SLM control program automatically flips the sign of the dispersion coefficient. This way to compensate a dispersion amount A, the operator enters the value A, not -A.

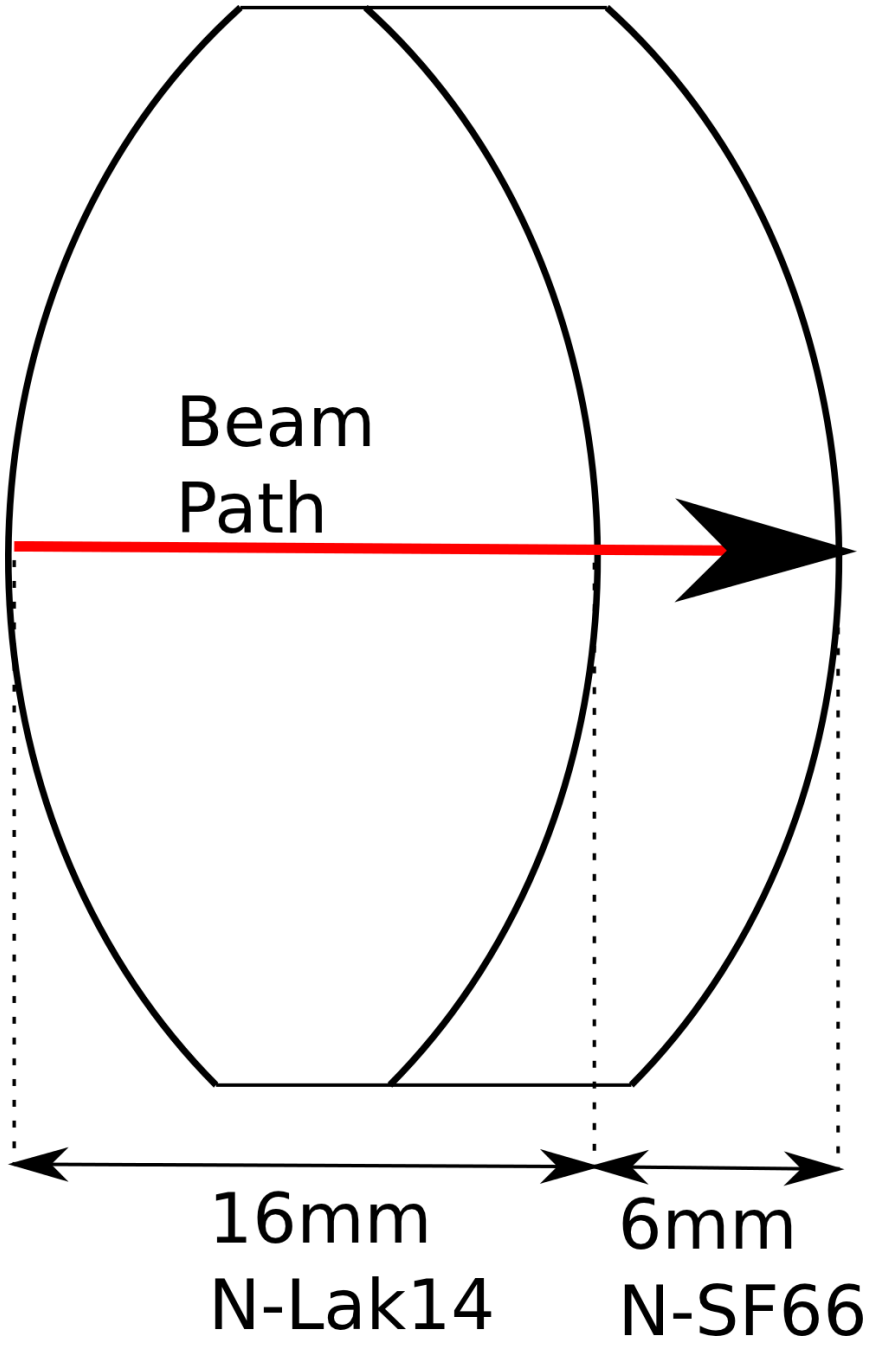

Figure 4.5: Diagram of the Primary Achromatic Doublet.
The bi-convex lens is made of N-Lak14, while the concave lens is made of N-SF66. The central path through the doublet travels 16mm through N-Lak14 and 6mm through N-SF66.

Chapter 5

Experimental Non-Linear Chirped Pulse Interferometry

5.1 Motivation

Chirped pulse interferometry has been shown to be less effected by 'unbalanced dispersion', meaning 2nd order dispersion in one arm of the interferometer[11]. The experiments previously performed with CPI were limited to small bandwidth lasers, so the effect of dispersion was small, and it was difficult to apply enough dispersion to test the limits of CPI. We show significant dispersion cancellation when the chirp is only 10 times the dispersion. As well it was not shown what effect CPI has in the presence of dispersion common to both arms of the interferometer, which will be referred to as 'balance dispersion'. We will experimentally demonstrate the difference between these sources of dispersion.

5.2 Common Experimental Details

5.2.1 Theoretical Model Based on Spectrum Fit

The spectrum was recorded before the interferometer and used along with the relevant chirp and dispersion parameters in the theoretical model when applicable. The theoretical model predictions shown for comparison to the experimental data.

5.2.2 Numerical Simulation using Spectrum

The spectrum data was analysed using the numerical simulation co-written with Mike Mazurek and Dr. Robert Prevedel in gnu-OCTAVE, and the numerical predictions for

each combination of chirp and dispersion are shown along with the experimental results. The simulated CPI trace featured significant side lobes which confuse a simple Gaussian least squares fit algorithm (See Fig 5.1). Instead the same LabVIEW fitting routine used in the experiment was applied to the simulated data and the FWHM was calculated based only on the largest peak (See Fig 5.2). For a pure Gaussian spectrum the results closely follow the theoretical values based on the same spectral values, suggesting this is the correct method for measuring the FWHM in both the simulation and the experiment. The spectrometer data was filtered to approximately 0.05nm bandwidth while the simulation using the exact spectrum from the Ocean Optics spectrometer resulted in a simulated minimum filter bandwidth of 0.5nm. It was thought that this may have been the cause of the side lobes. A few runs of the simulation were performed with the spectrum interpolated to 10 times higher resolution, giving an effective minimum bandwidth of 0.05nm, and the side lobes remained, so it was unlikely the cause (See Fig 5.3). It should also be noted that side lobes were present but not as prominent in the experimental data. The numerical predictions are listed with the experimental values for comparison.

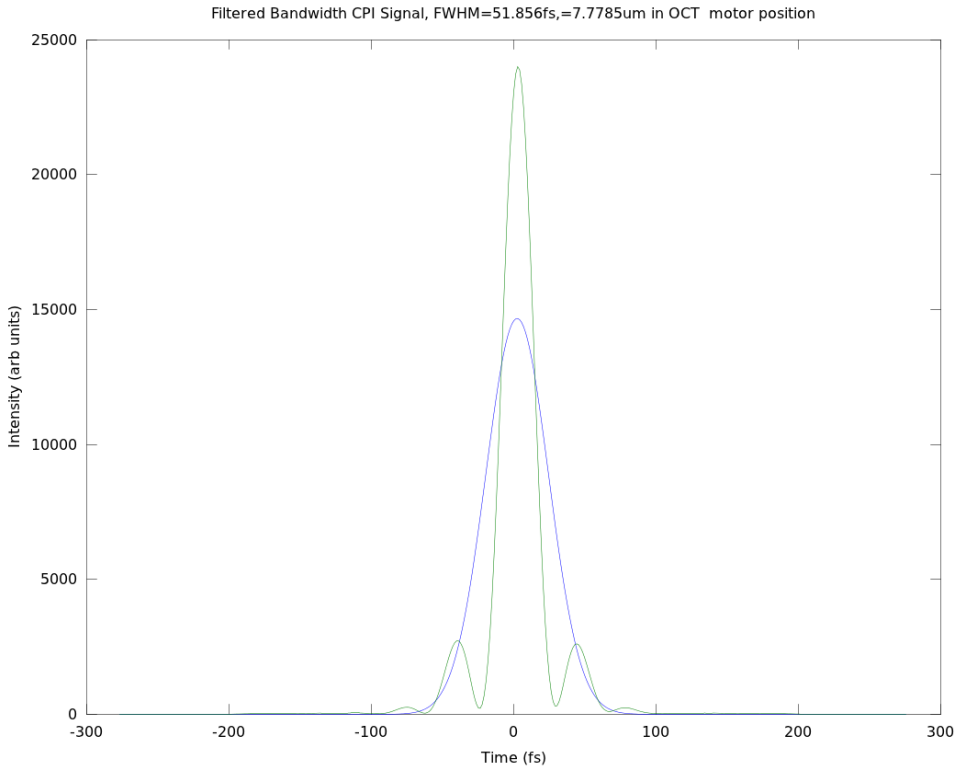

Figure 5.1: Simulated Filtered Spectrum Scan For $-2500fs^2$ IF Chirp
The simulated CPI signal (Green) featured significant side lobes, which confused a simple fitting routine(Blue).

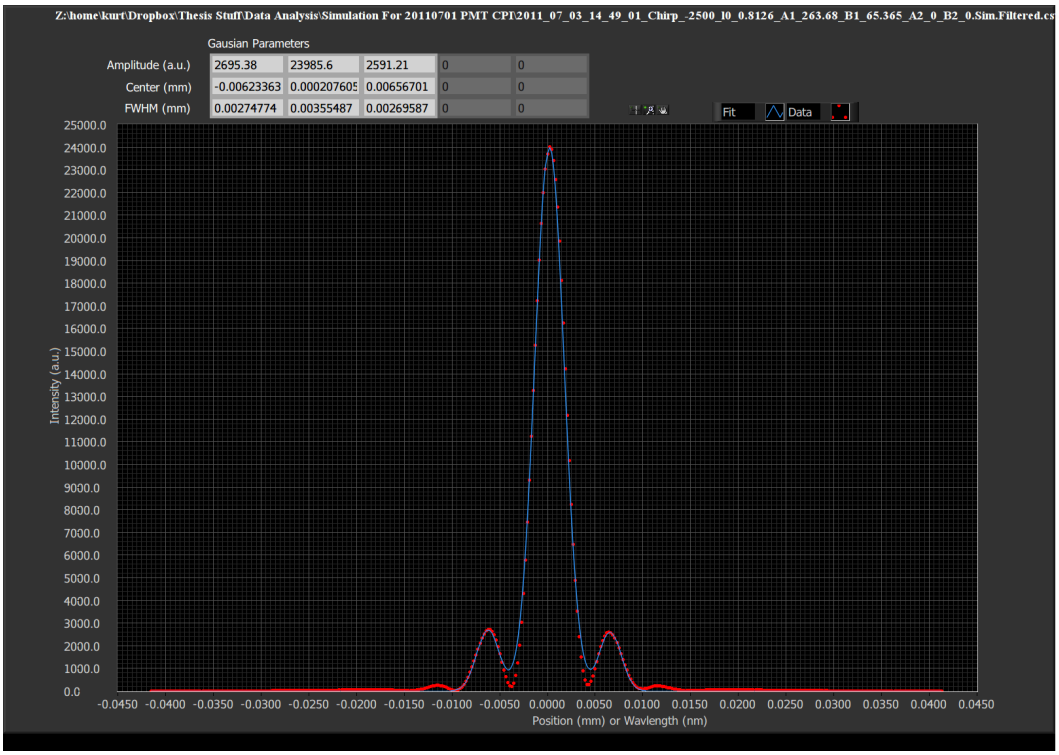

Figure 5.2: Simulated Filtered Spectrum Scan For $-2500fs^2$ IF Chirp
The simulated CPI signal (Red) featured significant side lobes but this was handled with ease by the multi-peak fitting subroutine (Blue).

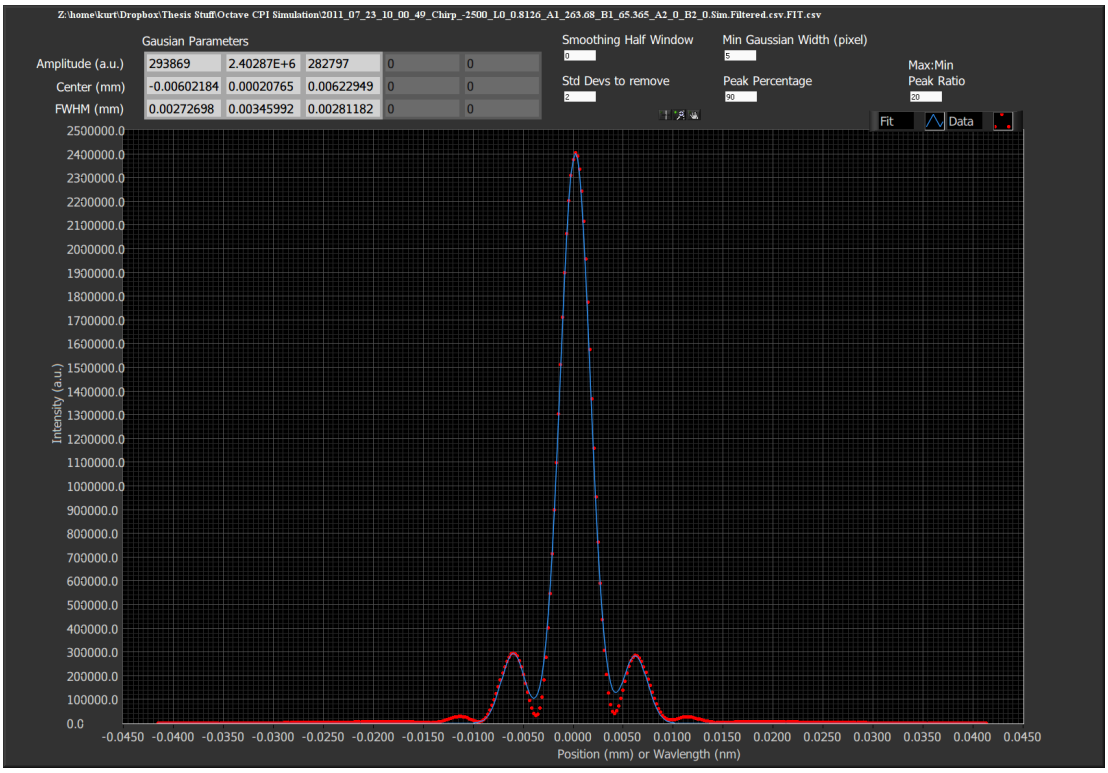

Figure 5.3: Simulated Filtered Spectrum Scan For $-2500fs^2$ IF Chirp with 0.05nm Filter bandwidth

The simulated CPI signal (Red) still features significant side lobes so the data resolution was not the main cause of the lobes.

5.3 Experiment 1 - Mirror, No lens, with and without 6mm BK7 double pass in reference arm

5.3.1 Experiment Specific Details

For this experiment the imaging optics were removed and the sample was a simple mirror. The dispersive element was a 6mm thick BK7 glass window that was threaded onto the mirror, to keep the mirror and glass parallel. In addition to measuring the CPI peak width (comparable to the OCT signal) a variety of other measurements were performed. The spectrum and FROG data were recorded, to provided estimates of how well the system *should* perform. The CPI signal center frequency is dependant on the dispersion, so filtering of the signal must take this into account. The efficiency of the system is also important, so the input and output power was recorded for each combination of parameters. Lastly the signal to noise ratio (SNR) was also measured, because a direct comparison can be made to OCT, and the SNR is an indicator of how well the system will perform when scanning

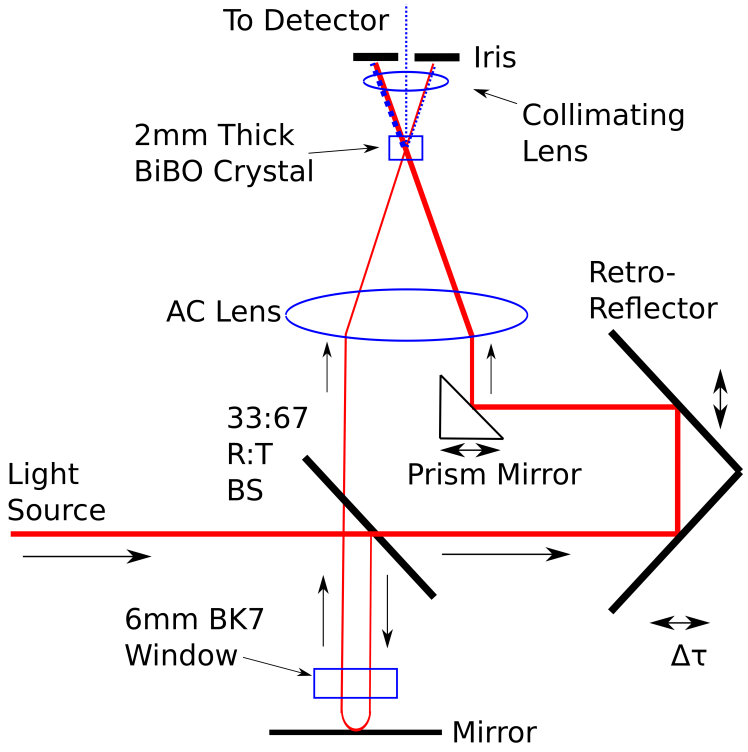

Figure 5.4: Experiment Layout
The glass window was placed in front of the sample mirror, so the dispersion was double pass.

things other than a mirror.

FROG Analysis

The laser was configured to produce a pulse with a wavelength bandwidth of 80nm FWHM (based on the spectrometer data). The pulse was sent to the FROG and minimized to 24.6fs which corresponds to a 3.69μm peak width in the presence of no extra dispersion. The Frog recorded the spectral FWHM of the pulse as 65.6nm. However the spectrum recorded by the frog had a significant negative spike, which may have confused the estimation algorithm (See fig 5.5).

Spectrum Analysis

The spectrum was recorded by the laser's internal spectrometer and after the 4-f with an Ocean Optics model USB4000 spectrometer. The spectrum are shown superimposed after

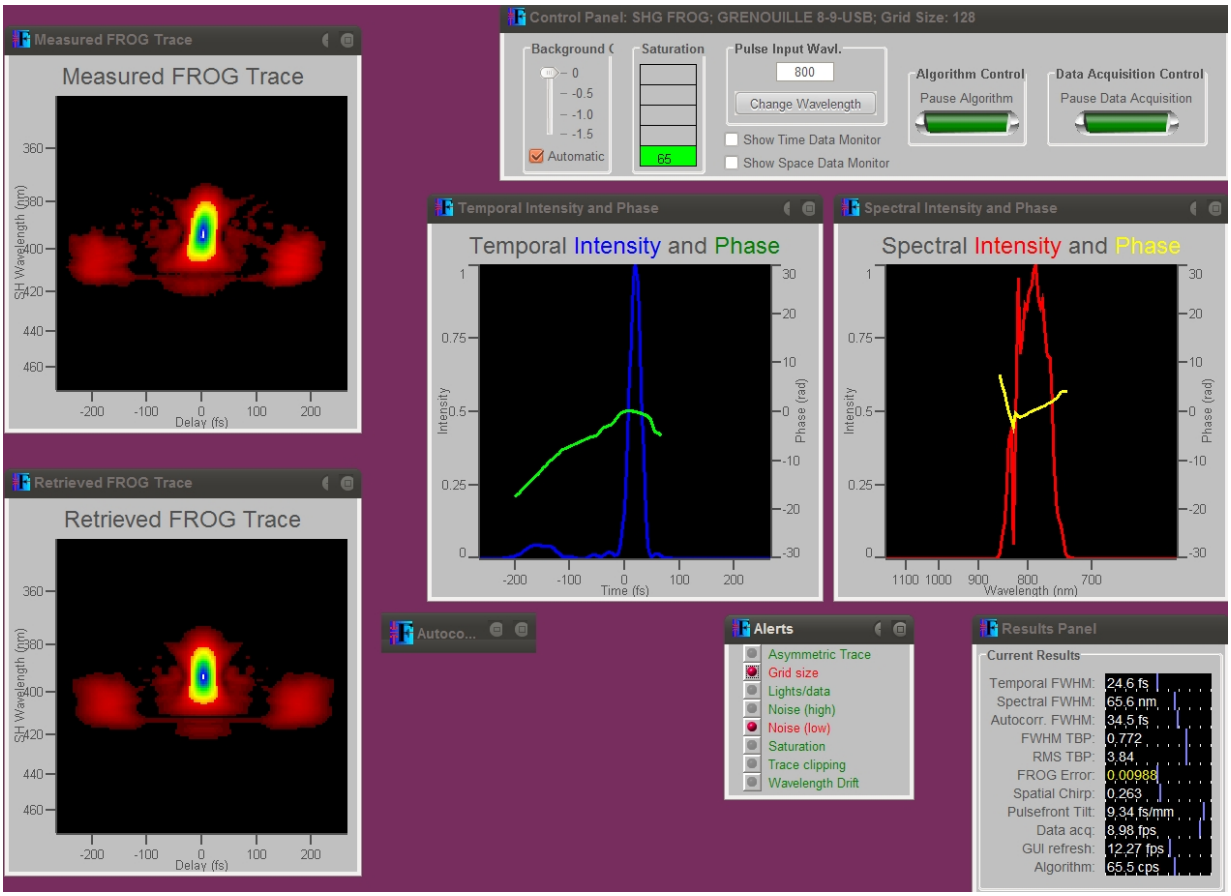

Figure 5.5: QuickFrog program readout for the time minimized pulse. The Temporal Intensity (Blue) shows a secondary lobe. Attempts to minimize this were unsuccessful. The Spectral Intensity (Red) shows a significant negative spike near the middle of the spectrum. This may explain the significantly lower spectral FWHM compared to the Ocean Optics spectrometer.

normalizing to a maximum amplitude of 1 (See Fig 5.6):

The pulse spectrum after the 4-f was fit with a Gaussian and the FWHM was determined to be 80nm, which is significantly larger than the FROG. This may be due to the large negative spike in the FROG spectrum confusing the QuickFROG fitting routine. Based on this spectrum the Fourier transform limited pulse length was 19.5fs (2.9um in motor position) so the pulse was near the transform limit.

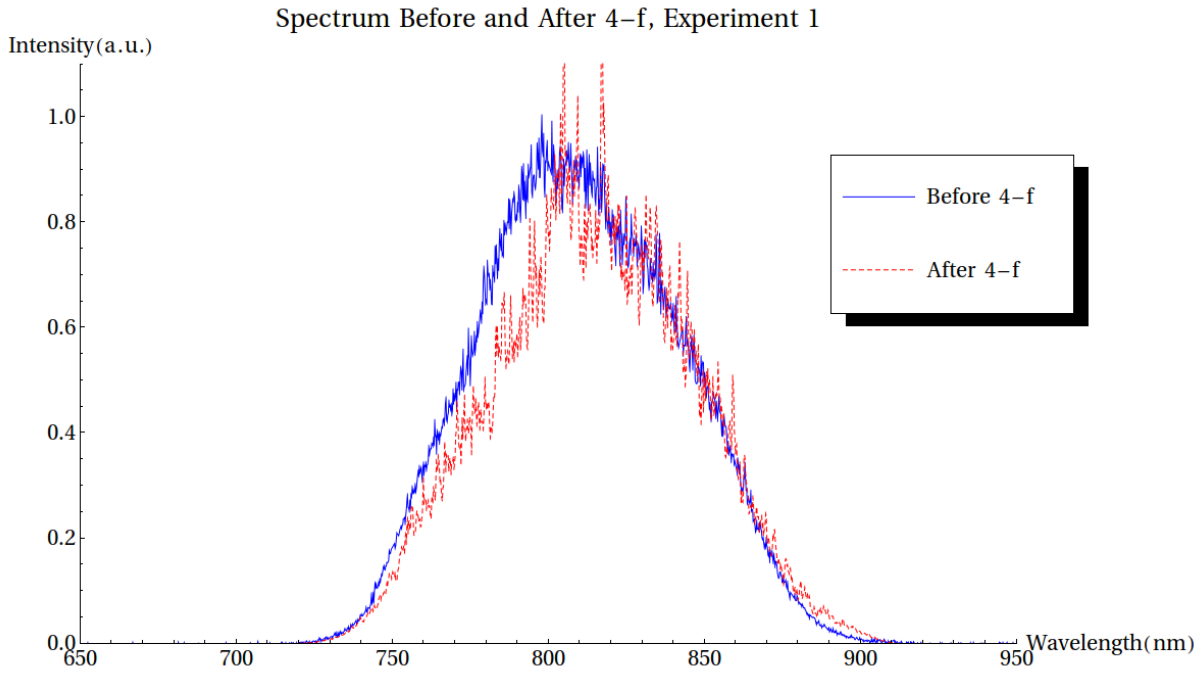

Figure 5.6: Spectrum before and after the pulse shaper.
The bandwidth after the 4-f (red, dashed) is clipped at the low end of the spectrum due to the wavelength dependant efficiency of the gratings. The spectrum before the PS (blue,solid) was centred at 809.8nm while the spectrum after the 4-f was centred at 814nm. The bandwidth before the 4-f was 82.8nm FWHM and after the 4-f was 80.5nm FWHM

Compensating Dispersion Due to the Large Achromatic Primary Lens

The 2nd and 3rd order dispersion values for the 75mm achromatic doublet primary lens were calculated to be $1362.45 fs^2$ and $374 fs^2$. The values added to the SLM to minimize the peak width were $1328 fs^2$ and $263 fs^3$ to minimize the pulse, and the CPI peak was recorded with the Spectrometer, and the PMT with 100x (200 scan) averaging. The spectrometer data was filtered to $.05nm$ acceptance bandwidth and the peak was found to be $4.1\mu m$ (equivalent to 27.3fs) which is larger than the Fourier limited value but near the FROG calculated value (111.0%). The PMT slit was set to $10\mu m$ (0.02nm filter bandwidth [1]). The peak was found to be $3.79\mu m$ (25.3fs), much closer to the FROG value (102.8%). Moving away significantly from these dispersion values increased the peak width, suggesting the calculated values were near optimum and therefore the pulse shaper was well calibrated. It is not clear why the PMT data more closely matched the predictions, but it may be due

[1]Personal communication with J. Lavoie, University of Waterloo

to the slightly narrower filter bandwidth. A false colour plot of the spectrum vs. reference arm position is shown in Fig 5.7. The simulated filtered signal for the same plot is shown in Fig 5.8.

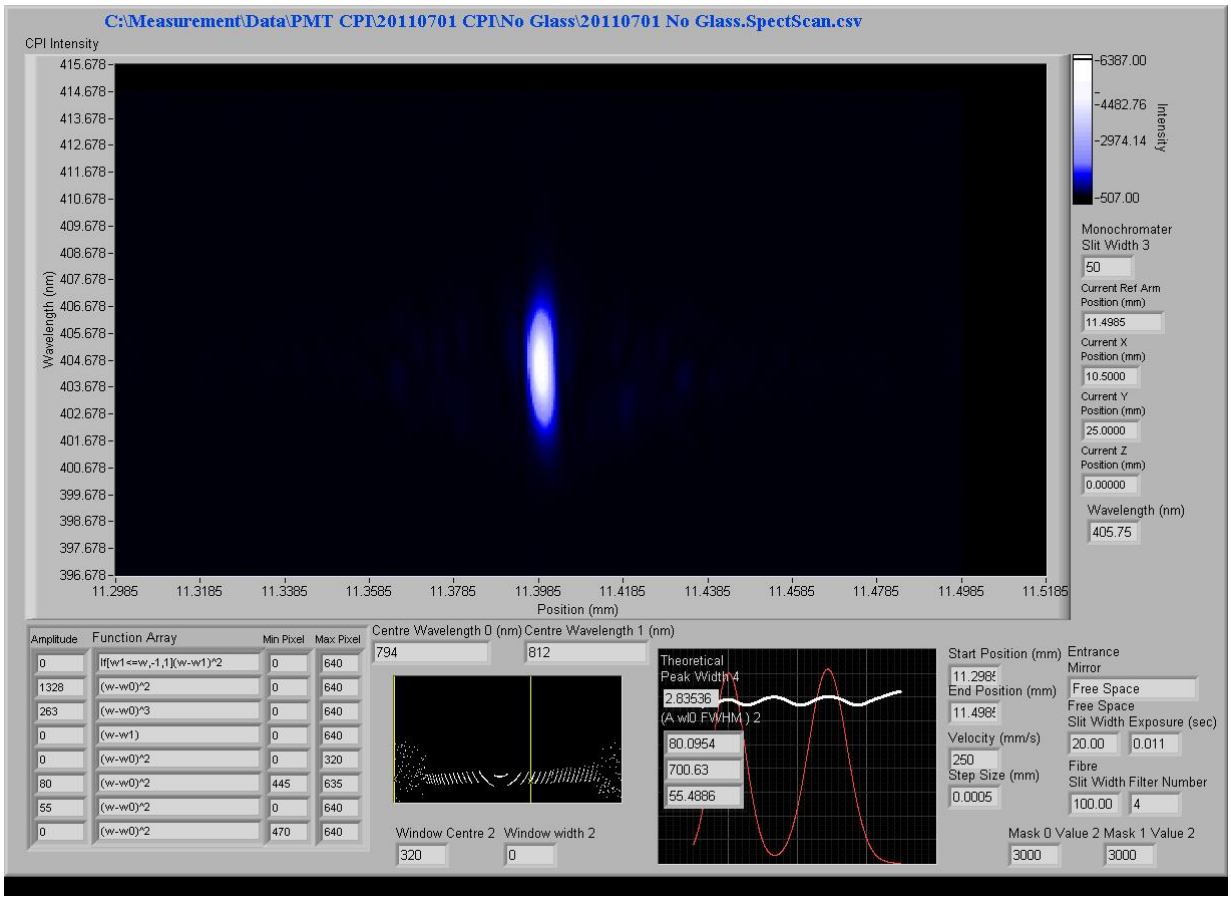

Figure 5.7: Spectrum Scan Readout For The compressed Pulse with Compensation for the Primary AC Lens.

The shape is slightly asymmetric indicating some dispersion is still present, however attempts at modifying the compensation parameters only resulted in broadening of the peak.

5.3.2 Dispersion Cancellation for Various Dispersion and Chirp Values

The non-linear chirp centred at 812nm with amplitude $-2500fs^2$ was added and the measurements were repeated. The method of flipping the amplitude sign at the central frequency was to use Mathematica's "If" function, so the chirp is referred to as the "IF chirp".

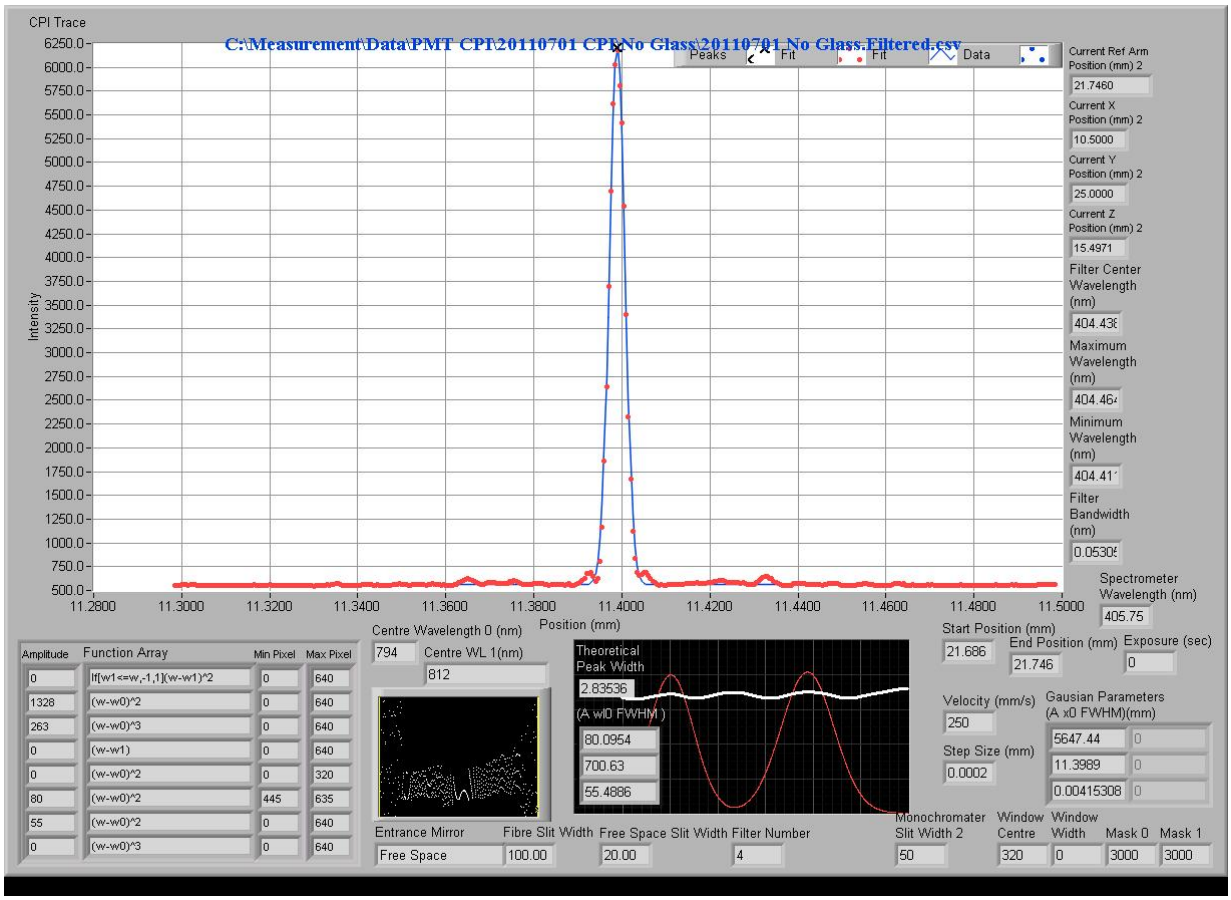

Figure 5.8: Filtered CPI Trace for the Compressed Pulse with Compensation for the Primary AC Lens.

A LabVIEW program integrates the CPI traces for a 0.05nm section of the spectrum.

The IF chirp was then increased to $-5000fs^2$, and then $-7500fs^2$, each time repeating the measurements. A 6mm window of BK7 glass was attached in front of the sample mirror and measurements were repeated. This means the total dispersion was equivalent to 12mm of glass. The sample mirror was adjusted slightly to maximize the signal intensity. A subroutine in the LabVIEW program fit the data in real time, displaying the FWHM in mm.The calculated value for the dispersion were $+263.676fs^2$ and $65.3645fs^2$. The subroutine was later adapted into a stand-alone program and used to to fit the data generated by the numerical simulation for consistency and to verify the fitting routine. The data for 0mm of glass is displayed in Fig 5.9 and for 6mm BK7 is displayed in Fig 5.10. The data is also given in Table 5.1

The data without glass in Fig 5.9 shows a slight reduction in the peak width from $0fs^2$ to $-2500fs^2$. This could be due unbalanced dispersion present in the interferometer due to the slightly different beam paths through the lens. The peak width increases slightly

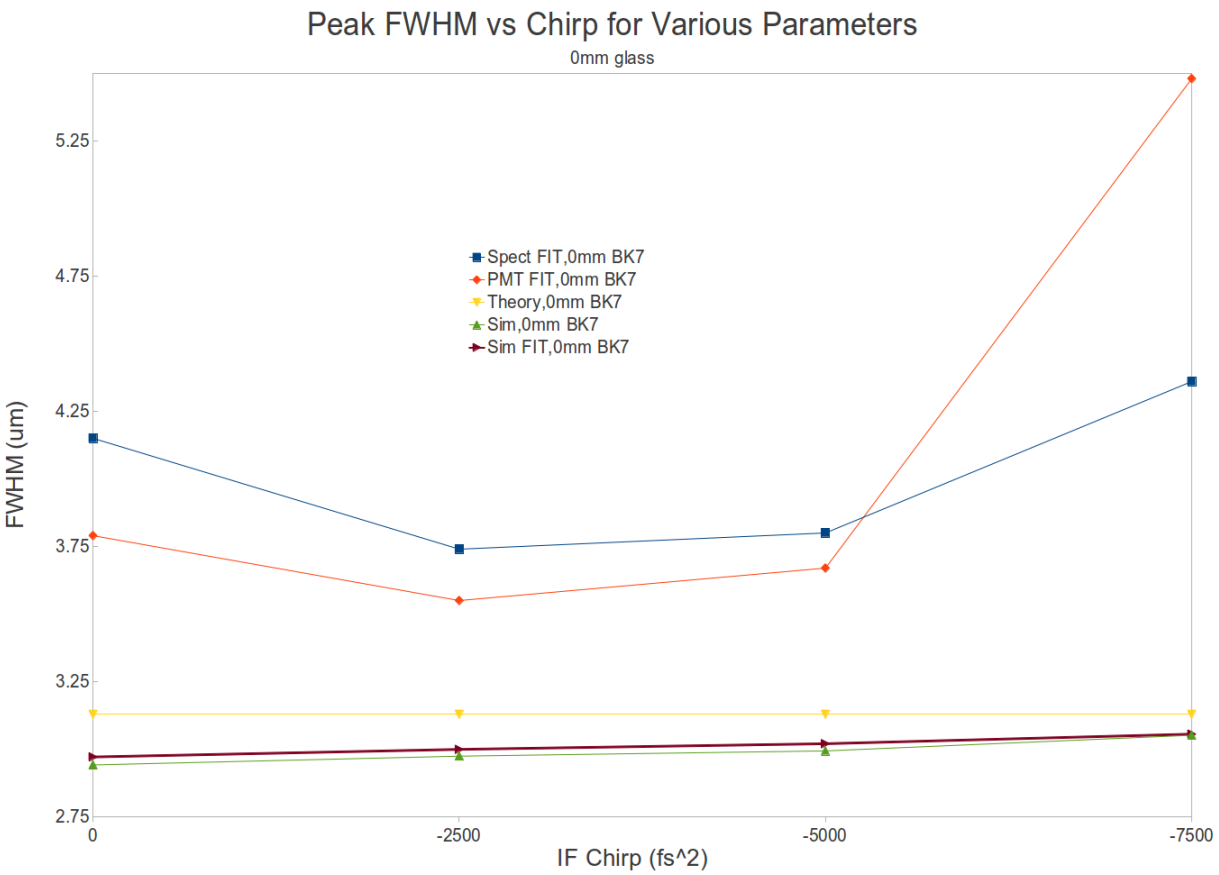

Figure 5.9: Peak FWHM vs Chirp for 0mm Glass
The data for non-zero IF chirps closely follows the theory and simulation. 'Spect' means spectrometer, 'Sim' means numerical simulation. FIT means the data was fit using the multi-peak program, otherwise a simple least-squares fit to a single Gaussian function was used. 'Theory' is the theoretical prediction based on the spectral FWHM assuming a perfect Gaussian.

when the chirp is increased to $-5000fs^2$ and dramatically when the chirp is increase to $-7500fs^2$. These effect were not predicted by theory, but one could be led to believe this is due to the non-Gaussian spectrum. The numerical simulation also does not predict this however, and it is based on the direct spectral data. This suggests that the IF chirp is only approximately generated by the SLM, and larger chirps are worse approximations.

The data for the case with glass, in Fig 5.10, shows that the chirp significantly reduces the broadening caused by the dispersion, although it does not completely cancel it out. The data closely follows the theory and multi-peak fitted simulation values except in the case of 0 chirp, which is discussed later in the section. The simple fit values are significantly larger

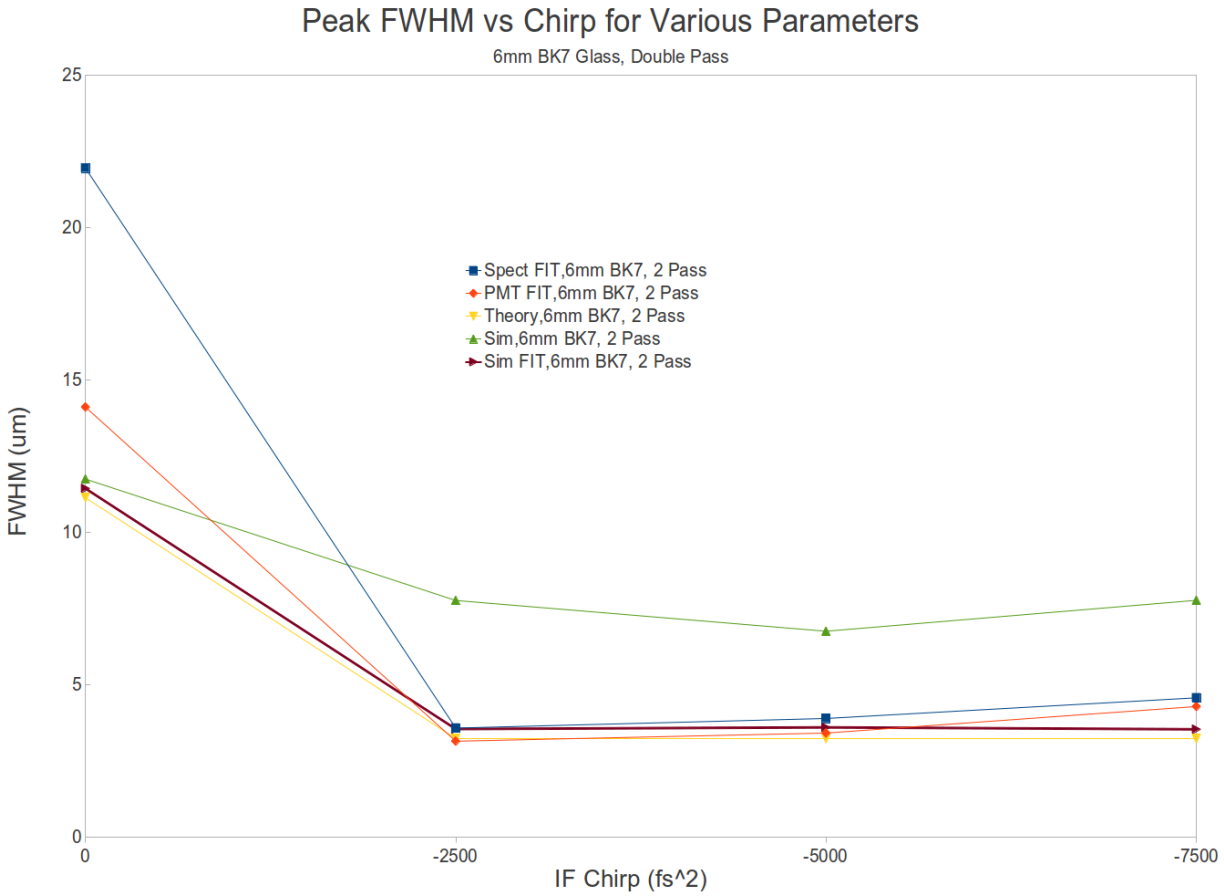

Figure 5.10: Peak FWHM vsChirp for 6mm Glass
The data for non-zero chirps closely follows the theory and simulation. 'Spect' means spectrometer, 'Sim' means numerical simulation. FIT means the data was fit using the multi-peak program, otherwise a simple least-squares fit to a single Gaussian function was used. 'Theory' is the theoretical prediction based on the spectral FWHM assuming a perfect Gaussian.

for all values except 0 chirp, suggesting this method is not useful, and also that the side lobes are not part of the CPI signal predicted by the theory. The peak width grows slightly as the chirp is increased, contrary to the theory or simulation. This is likely due to the SLM having increasing difficulty producing larger chirps. Because the SLM has only 640 pixels, the phase modulation is only correct for the center frequency of each pixel. Also, because the SLM can only produce 2π of phase modulation, the phase function has more and more jumps from $-\pi$ to $+\pi$ as the chirp amplitude increases. These creates pairs of pixels with significantly different voltage values. It is unclear exactly effect this has on the phase modulation. The result is that large chirps comparable to the previous linear-CPI experiments are not possible without degradation in dispersion cancellation. However, the

theory is also shown to be accurate at a much smaller ratio of chirp to dispersion. In the previous experiments the ratio was approximately $|A/\epsilon| \approx 200$ [13][2] where as is in this experiment for $-2500fs^2$ the ratio is $|A/\epsilon| \approx 10$. This means that significant dispersion cancellation can be accomplished with much smaller chirps than previously demonstrated.

In the case of 0 chirp with the glass added, the signal shows significant interference or distortion from the roughly Gaussian shape observed in the other cases. The multi-peak fitting interpreted the signal as two separate peaks. As an estimate then, the center to center distance of the peaks, plus half the FWHM of each peak was used. These numbers are the values recorded in the figures and table, but marked with an asterisk "*" in the table. A manual fit was also performed, where it was assumed the center of the Gaussian peak was noisy, so a only the "Gaussian Looking" portion of the signal was fit. This gave a result of $11\mu m$, which was much closer to the theory and simulation value. This could mean that the signal should have been a Gaussian, and the distortion was due to something other than 2nd order dispersion.

Peak FWHM (μm) For Various Chirps And Methods					
		IF Amount (fs^2)			
Glass	Method	0	-2500	-5000	-7500
0mm BK7	Spect FIT	4.15	3.74	3.80	4.36
0mm BK7	PMT FIT	3.79	3.55	3.67	5.48
0mm BK7	Theory	3.13	3.13	3.13	3.13
0mm BK7	Sim	2.94	2.97	3.00	3.05
0mm BK7	Sim FIT	2.97	3.00	3.02	3.05
6mm BK7, 2 Pass	Spect FIT	21.96*	3.59	3.90	4.58
6mm BK7, 2 Pass	PMT FIT	14.12*	3.16	3.422	4.29
6mm BK7, 2 Pass	Theory	11.15	3.24	3.24	3.24
6mm BK7, 2 Pass	Sim	11.76	7.77	6.76	7.79
6mm BK7, 2 Pass	Sim FIT	11.45	3.55	3.61	3.55

Table 5.1: Table of FWHM values for various NL chirp values. 'Spect' means spectrometer, 'Sim' means numerical simulation. FIT means the data was fit using the multi-peak program, otherwise a simple least-squares fit to a single Gaussian function was used. 'Theory' is the theoretical prediction based on the spectral FWHM assuming a perfect Gaussian.

5.3.3 Peak Central Wavelength

The monochrometer wavelength setting for the PMT required adjustment each time the chirp was changed, and is recorded along with the numerical predictions for the same settings in table 5.2. The spectrometer filtering is automatically adjusted based on the peak wavelength, and is also given for comparison.

[2]Personal communication with J. Lavoie, University of Waterloo

	Peak Central Wavelength (nm)					
	0mm BK7			6mm BK7, 2 Pass		
IF Chirp (fs^2)	Spect	PMT	Sim	Spect	PMT	Sim
0	404.44	404.00	403.08	404.46	404.50	407.13
-2500	404.70	404.50	403.88	404.06	403.90	403.26
-5000	404.71	404.50	403.88	404.41	404.30	403.50
-7500	404.75	404.50	403.88	404.58	404.50	403.73

Table 5.2: Table of Peak Central Wavelength with and without dispersion for various chirps. In the 0mm glass case, the slight wavelength shift is due to an imperfect choice of chirp center wavelength. The Spectrometer and PMT data follow the same trend as the simulation, the chirp causes a slight increase in the central wavelength. In the 6mm glass case, the dispersion changes the center wavelength, while the chirp partially corrects this, but increasing the chirp reduces this effect. The difference between Spect and PMT values is due to slightly different calibrations for the spectrometer and monochrometer.

The Spectrometer and PMT data follow the same trend as the simulation, the chirp causes a slight increase in the central wavelength. In the 6mm glass case, the dispersion changes the center wavelength, while the chirp partially corrects this, but increasing the chirp reduces this effect. The difference between Spect and PMT values is due to slightly different calibrations for the spectrometer and monochromater.

5.3.4 Input and Output Power

Input and Sample Arm Power Measurements

The input power at the interferometer was 238mW, and the 37% BS reflected 90mW to the sample, for an effective Reflectance of 37.8%. This means that 148W was sent through the reference arm, and 54.8mW would be transmitted through the BS from the sample arm after reflection from the mirror based on the formula:

$$P_{sample} = R_{BS} \times R_{Mirror} \times (1 - R_{BS}) \times P_{Input} \tag{5.1}$$

Where R_{Mirror} is the Reflectance of the mirror, previously measured to be 97.9%.

$$P_{sample} = .378 \times .979 \times (1 - .378) \times 238mW = 54.8mW \tag{5.2}$$

Output Signal Power

Using a mirror as the sample provides significant signal, and allowed us to measure the peak power of the unfiltered CPI signal with a standard power-meter (Thorlabs PM-100 with

S121B head). After the peak position was determine by the LabVIEW Fitting Routine, the reference motor was moved to the peak location and the power was recorded. The background signal was determine by moving the reference arm minus 10mm from the peak and recording the power. This method was preferable to simply blocking the sample arm because it also takes into account any IR or UV Self-SFG light leaking in from the sample arm.

Table 5.3: Power Readings For Various Chirps

	Power (μW)	
IF Chirp (fs^2)	0mm BK7	6mm BK7, 2 pass
0	1855	775
-2500	795	700
-5000	493	435
-7500	350	313

The results are listed in table 5.3. It is clear that increasing the chirp causes a decrease in signal power. The reduction in signal power is not predicted by the simulation. The problems with increasing chirps could cause this. The simulation does not take into account the effects of phase matching and this could also contribute. It is interesting that adding the glass with zero chirp causes a similar reduction in power as no glass with $-2500fs^2$ chirp. Adding the glass will slightly reduce the reflected beam power due to reflection losses but not enough to account for the total signal reduction. More research in this area is advisable.

5.3.5 Signal to Noise Ratio

For the measurement of background variance for signal-to-noise ratio (SNR) the sample mirror was blocked because this is the standard method in OCT. Because of the method of attaching the dispersive glass, it was also blocked, which may reduce the background slightly (and increase the SNR slightly) for those the values. A scan of of $20\mu m$ centred on the peak location provided 100 samples for computing the variance, repeating the measurement for each chirp setting. The amplitude was calculated by subtracting the maximum value from the minimum value for the previously recorded CPI traces at each chirp value. The PMT data was also recorded with 1x averaging (forward scan plus retract scan) for comparison.

The results are given in table 5.4. It is interesting that the SNR improves when the chirp is applied compared to no chirp, for both the spectrometer and the PMT. However, similar to the other measurements, the SNR decreases slightly with increasing chirp in the case of the spectrometer. In the case of the PMT it is not clear if the SNR is affected by the increasing chirp. Either way, the SNR is much lower for the PMT than for the spectrometer.

Table 5.4: Signal-to-Noise Ratio

	SNR For Various Chirps, Glass,					
	0mm BK7			6mm BK7		
IF Chirp (fs^2)	PMT 1x	PMT 100x	Spectrometer	PMT 1x	PMT 100x	Spectrometer
0	51.95	70.42	66.39	43.2	59.98	67.18
-2500	56.93	74.57	80.01	55.5	73.424	80.80
-5000	58.37	72.70	79.59	57.07	71.78	79.27
-7500	55.60	71.01	77.90	58.40	73.69	77.65

5.3.6 Discussion

The experiment has shown that the pulse shaper can produce the non-linear chirp (IF chirp).It has also shown that the IF chirp provides significant dispersion cancellation with relatively small chirp amplitude. Unfortunately the pulse shaper appears to be incapable of making larger chirps, reflected in the larger peak width and lower signal power. This limits the amount of dispersion cancellation that can be generated. It also has implications to biological sampling, because the reflected power from a biological sample is expected to be much lower than from a mirror, which will further reduce the CPI signal.

For scanning biological samples a minimum SNR of 85dBa is required [3]. The spectrometer approaches this value, but is far too slow to be used as the sole sensor. However a dedicated, cooled sensor with a high speed interface may be useful. The system was designed with the intention of biological scanning. The PMT is not sufficient for biological scanning with the current set-up and power levels. The PMT currently operates at room temperature and a cooled unit may be significantly better. Some things of note: The input power was about half what can be expected of the system. In the best case, this would add 6dBa to the values in the table. In the worst case this would also increase the background noise by 6dBa although it is likely that the SFG/SHG only contributes a fraction of the background, with thermal noise the other source of noise. Also, the sample power is far too high for use in scanning a living sample[4], and caused burning if the beam was left too long in one position. Reducing the sample power will reduce the SNR. Lastly the relatively low ratio of the beam splitter (1:2) has a negative effect on the SNR, since approximately 1/3 of the after-sample signal is reflected away. Assuming a 1:99 beam splitter ratio could improve the SNR by 3.5dBa.

[3]Personal Communication with Dr. K. Bizheva, University of Waterloo

[4]Personal communication with Dr. K Bizheva, University of Waterloo

5.4 Experiment 2 - Effect of Balanced Dispersion

The CPI effect is primarily intended to compensate the case of dispersion present in one arm only. But what about the case where dispersion is present in both arms/pulses, such as the case of fibre based OCT [22]? Unlike the WLI used in OCT, SFG is affected by global phases. So dispersion present before the interferometer will affect the cross-correlation signal width. By adding a 10mm section of glass to the system before the interferometer, the dispersion affects both arms.

5.4.1 Experiment Specific Details

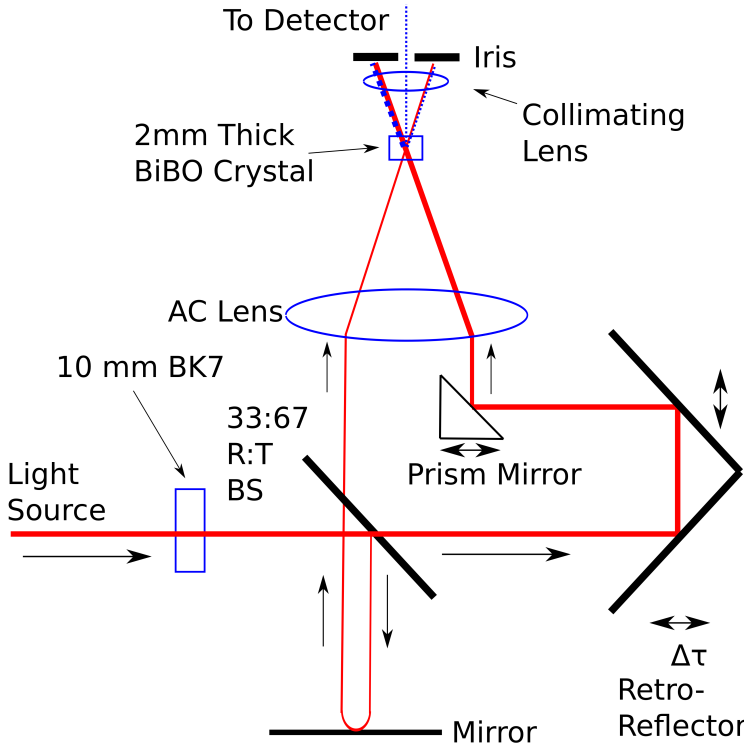

Figure 5.11: Experiment 2 Layout
The glass window was placed in front of the interferometer, so the dispersion was single pass.

For this experiment the imaging optics were removed and the sample was a simple mirror. The dispersive element was a 10mm thick BK7 glass window that was placed in the beam path before the BS. In addition to measuring the CPI peak width (comparable to the OCT signal), the spectrum and FROG data were recorded, to provided estimates

of how well the system *should* perform. The FROG data was also recorded with the glass block in the frog beam path, with and without compensation.

FROG Analysis

The laser was configured to produce a pulse with a wavelength bandwidth of 80nm FWHM (based on the spectrometer data). The pulse was sent to the FROG and minimized to 21.4fs which corresponds to a $3.21\mu m$ peak width in the presence of no extra dispersion. The Frog recorded the spectral FWHM of the pulse as 63.7nm. However the spectrum recorded by the frog had a significant negative spike, which may have confused the estimation algorithm (See fig 5.12). The glass was placed in the beam path and the FROG data was recorded without compensation(See fig 5.13). The temporal FWHM grows to $109fs$, which corresponds to $16.28\mu m$ in motor position if it were measured by the interferometer. The value for the 2^{nd} and 3^{rd} order dispersion caused by the glass was calculated to be $224fs^2$ and $54fs^3$ respectively. These values were add into the SLM control program and the FROG data was recorded(See fig 5.14). The Temporal FWHM was recovered to $21.9fs$.

Spectrum Analysis

The spectrum was recorded by the laser's internal spectrometer and after the 4-f with an Ocean Optics model USB4000 spectrometer. The spectrum are shown superimposed after normalizing to a maximum amplitude of 1 (See Fig 5.15).

The pulse spectrum after the 4-f was fit with a Gaussian and the FWHM was determined to be 82nm, which is significantly larger than the FROG. This may be due to the large negative spike in the FROG spectrum confusing the QuickFROG fitting routine. Based on this spectrum the Fourier transform limited pulse length was 19.4fs (2.9um in motor position) so the pulse was near the transform limit.

5.4.2 Dispersion Cancellation of Balanced Dispersion

The system was measured with and without the glass, and with and without chirp and/or compensation. The results are shown along with simulation results in Fig 5.16 and Table 5.5. The amplitude of the chirp in this case was $+2500fs^2$ centered at $810.5nm$. Again the results for 10mm glass and no compensation showed distortion from the Gaussian shape predicted by the simulation. The same method for fitting was used as in experiment 1, and are noted by an asterisk "*". For the theoretical model the balanced dispersion was simply multiplied by 2 to account for it being present in both arms of the interferomter. This worked fairly well as an estimate with the prediction based on 10mm of glass with no compensation or chirp coming in right between the values for the two fitting methods used in the simulation.

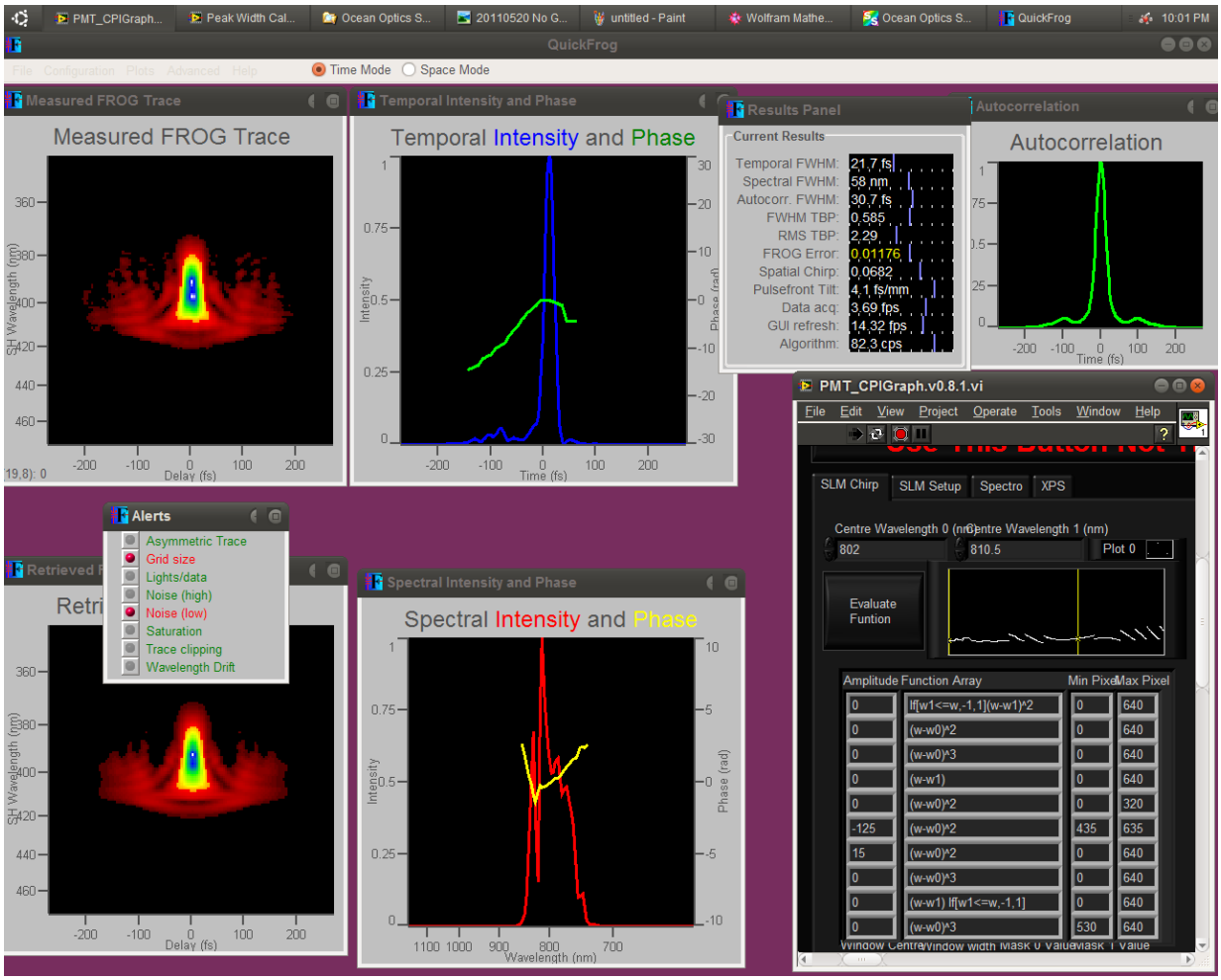

Figure 5.12: QuickFrog program readout for the time minimized pulse. The Temporal Intensity (Blue) Shows a secondary lobe. Attempts to minimize this were unsuccessful. The Spectral Intensity (Red) shows a significant negative spike near the middle of the spectrum. This may explain the significantly lower spectral FWHM compared to the Ocean Optics spectrometer.

The balanced dispersion causes the signal to broaden as expected when there is no chirp (See Fig. 5.18). The signal appears to degrade into multiple peaks rather than a single central peak, making fitting to a Gaussian difficult. The same method was used to fit this case as in experiment 1. When the second and third order compensation is added the central peak shape, and width are recovered, with only a small difference (See Fig. 5.19).

When the compensation is removed, and a chirp of $-2500 fs^2$ is added (See Fig. 5.21) the signal is significantly better than with no compensation (See Fig. 5.20), showing side

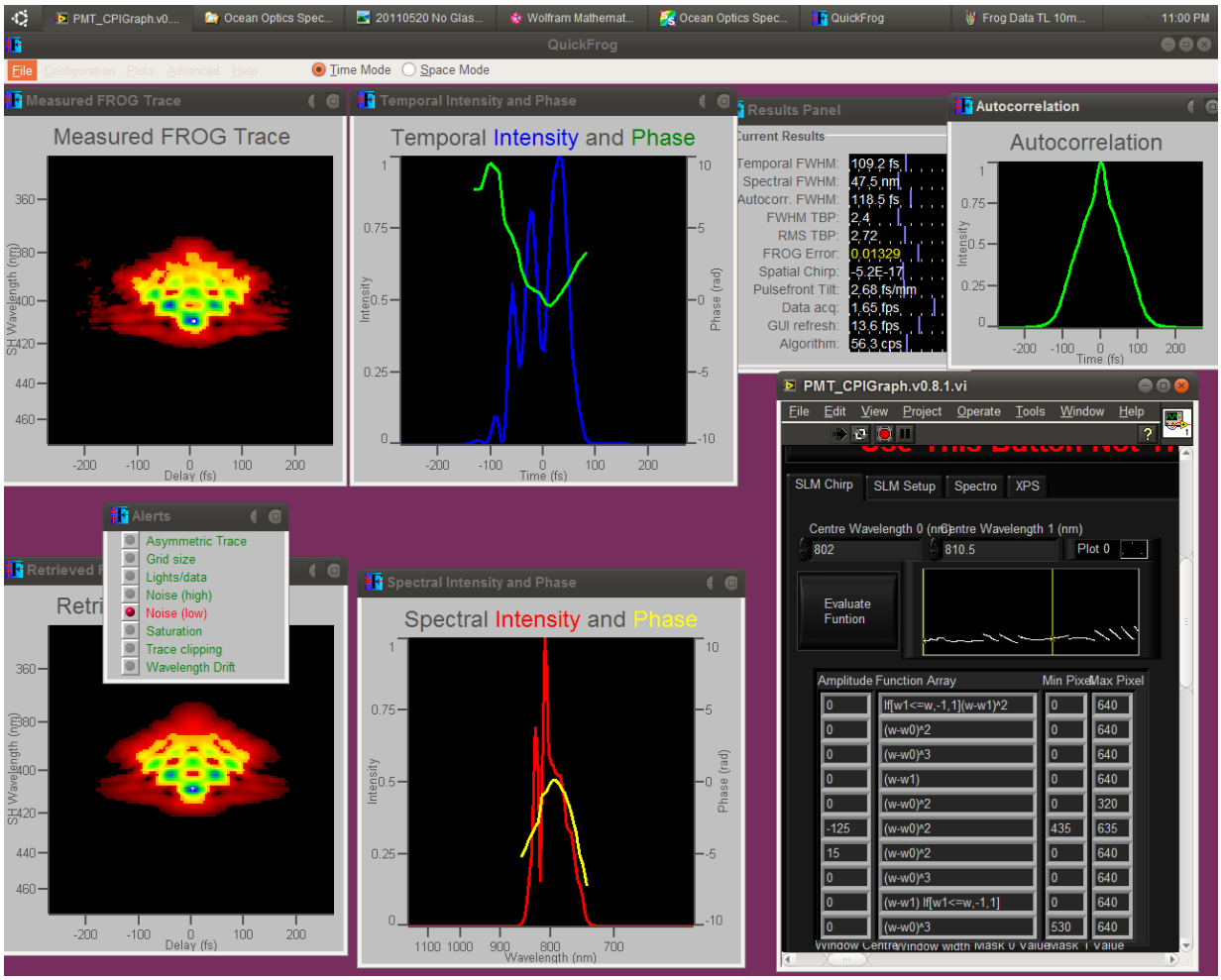

Figure 5.13: QuickFrog program readout for the pulse with 10mm of uncompensated BK7. The temporal FWHM grows to $109fs$ when $224fs^2$ of second order dispersion is added due to the glass block.

lobes, but a clear central peak, with minimal broadening. The broadening of the IF chirped peak width is 30% compared to no-glass no-chirp case , but only 3.6% of the broadening due to the glass without IF chirp. This is somewhat surprising because balanced dispersion is not what the theoretical model was based on, but is confirmed by numerical simulation with the same parameters . When the chirp and compensation are added the signal is fully recovered (See Fig 5.22) as expected.

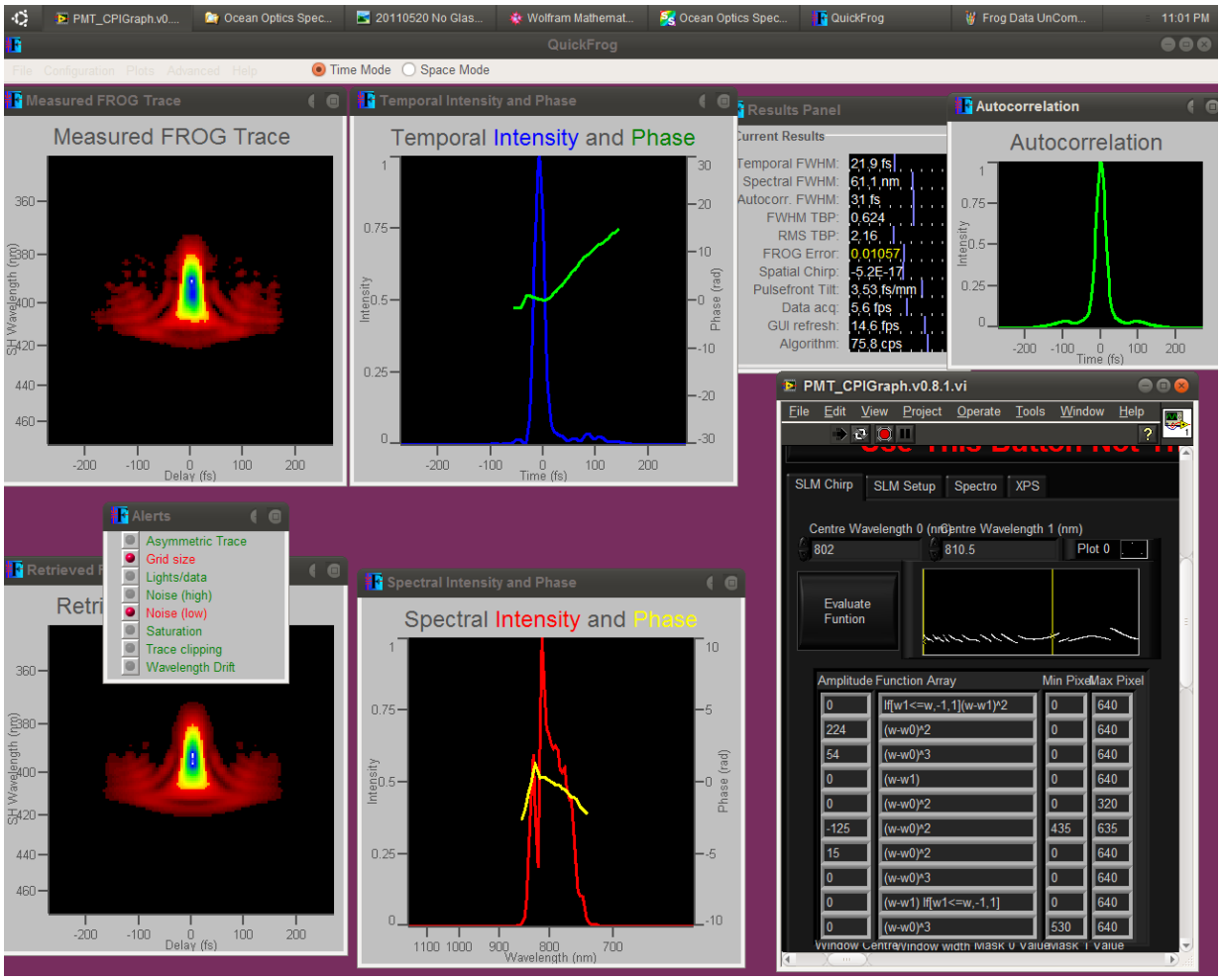

Figure 5.14: QuickFrog program readout for the pulse with 10mm of BK7 and compensation.

The temporal FWHM returns to $21.9fs$ when $224fs^2$ and $54fs^3$ of compensation is added as well as the glass.

5.5 Discussion

NL-CPI has been shown to significantly reduce the effects of balanced 2^{nd} order dispersion. This has practical applications if this method is to be retrofit in existing fiber based OCT systems, where potentially large amounts of balanced dispersion are present.

These results make sense when we remember that the filtered CPI trace is not a measure of the time duration of the pulses but a measure of the strength of frequency correlations in the pulses. Adding balanced dispersion to the pulse means that the frequency pairs at different group delays will never simultaneously add up to a single value, but the difference

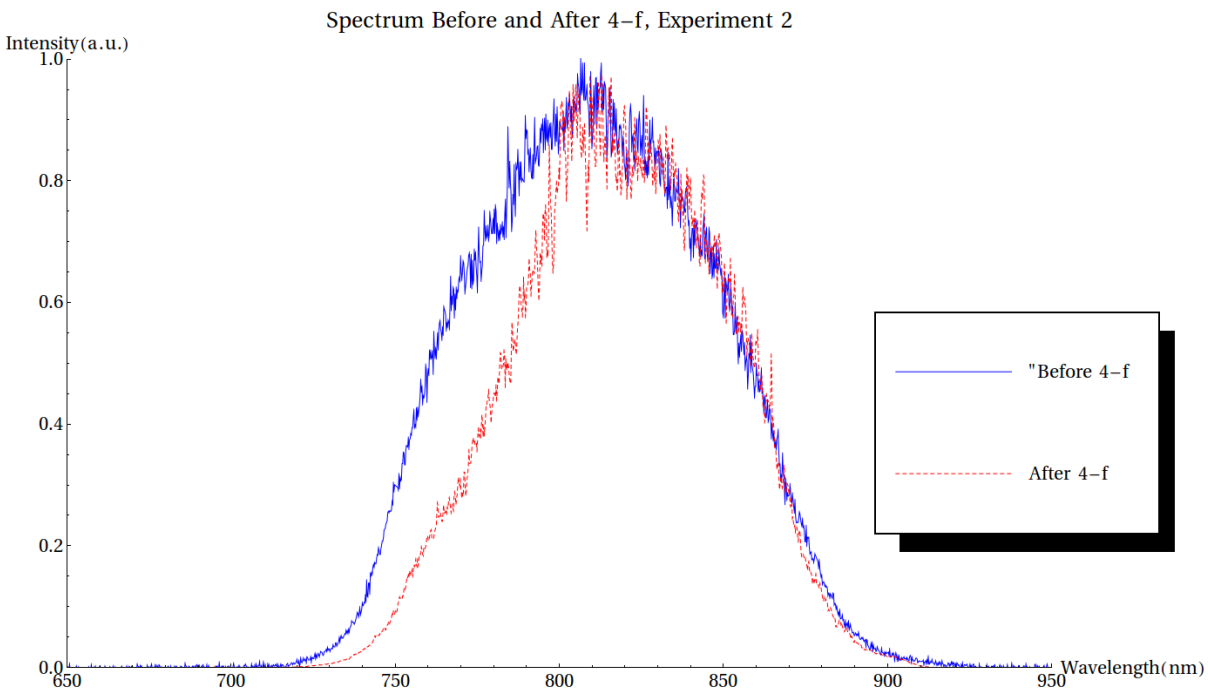

Figure 5.15: Spectrum before and after the pulse shaper.
The bandwidth after the 4-f (dashed) is clipped at the low end of the spectrum due to the wavelength dependant efficiency of the gratings. The spectrum before the PS (solid) was centred at 809nm while the spectrum after the 4-f was centred at 812nm. The bandwidth before the 4-f was 89.8nm FWHM and after the 4-f was 81.56nm FWHM

remains small as long as the dispersion is small relative to the chirp.

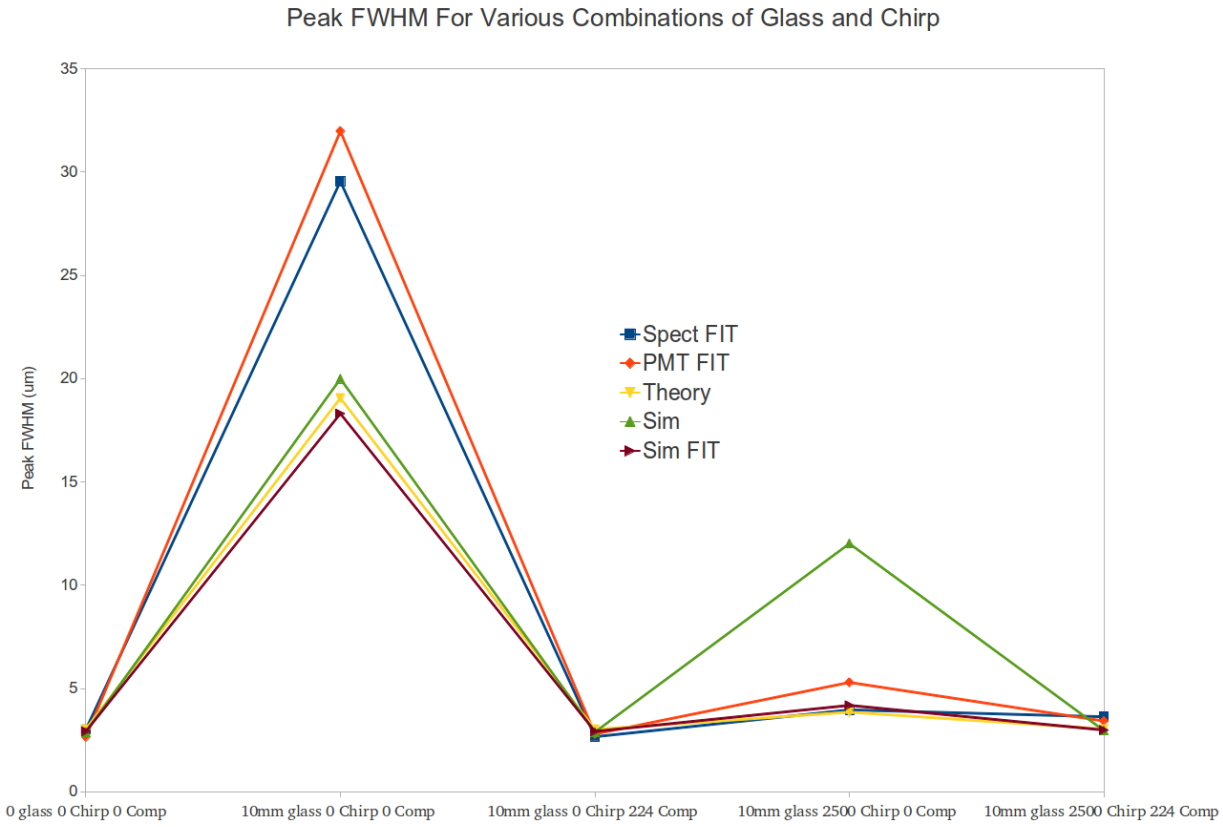

Figure 5.16: Peak FWHM For Various Combinations
The data for non-zero IF chirps closely follows the simulation. 'Spect' means spectrometer, 'Sim' means numerical simulation. FIT means the data was fit using the multi-peak program, otherwise a simple least-squares fit to a single Gaussian function was used.

Peak FWHM (um)								
10mm Before	40mm Ref	Chirp	2nd Order Comp	Spect FIT	PMT FIT	Theory	Sim direct FIT	Sim Multi FIT
0	0	0	0	3.02	2.66	3.03	2.90	2.93
10	0	0	0	29.55*	31.98*	19.06	20.00	18.31
10	0	0	224	2.67	2.8	3.03	2.90	2.927
10	0	+2500	0	3.97	5.3	3.86	12.02	4.19
10	0	+2500	224	3.64	3.43	3.03	2.97	2.99

Table 5.5: Table of Peak FWHM with and without chirp and glass for 10mm BK7 before interferomter.
'Spect' means spectrometer, 'Sim' means numerical simulation. FIT means the data was fit using the multi-peak program, otherwise a simple least-squares fit to a single Gaussian function was used. 'Theory' is the theoretical prediction based on the spectral FWHM assuming a perfect Gaussian.

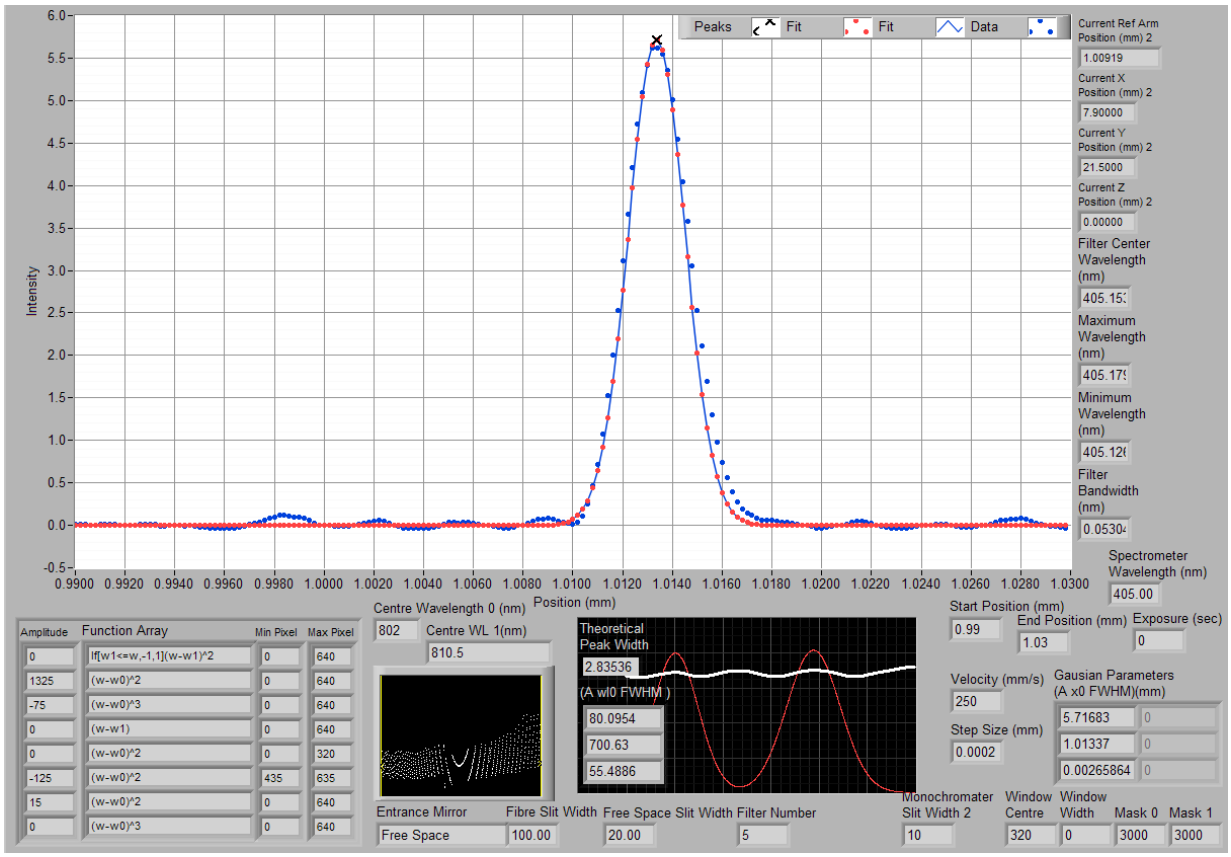

Figure 5.17: PMT CPI Trace without 10mm glass before the interferometer.

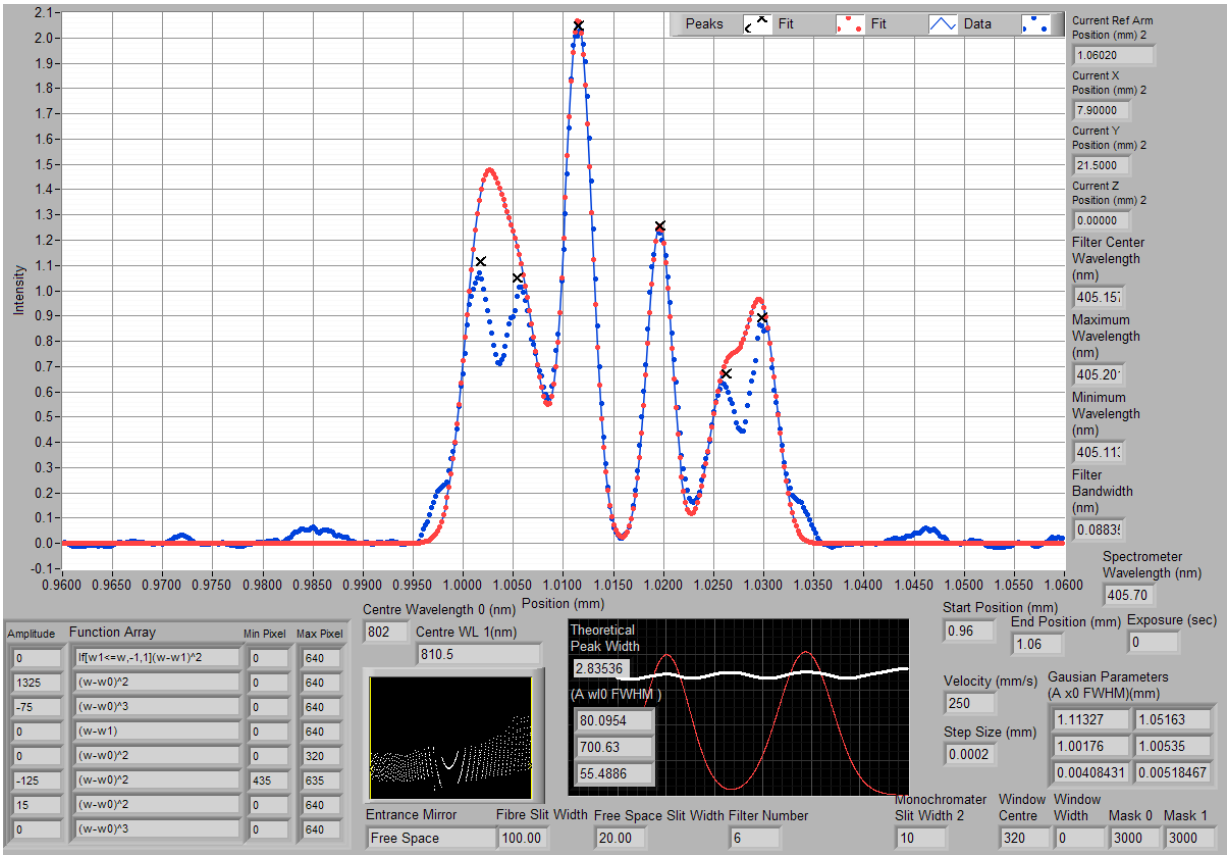

Figure 5.18: PMT CPI Trace with 10mm glass before the interferometer with no compensation.

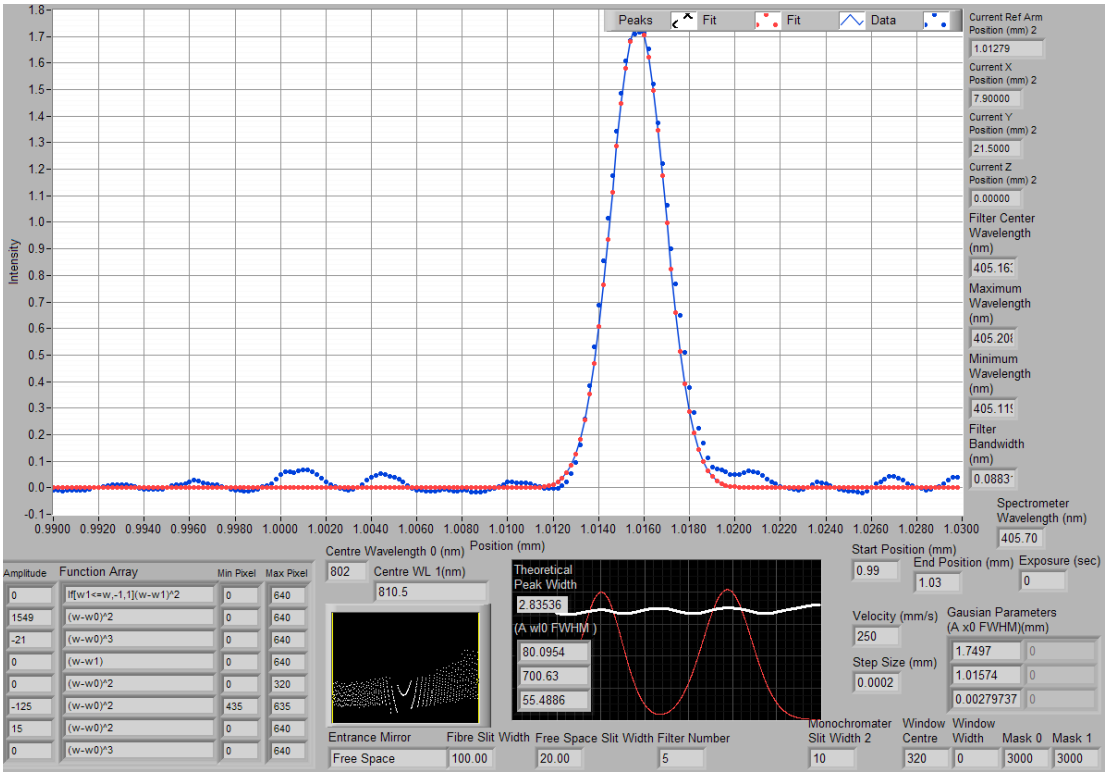

Figure 5.19: PMT CPI Trace with 10mm glass before the interferometer with $224fs^2$ and $54fs^3$ compensation.

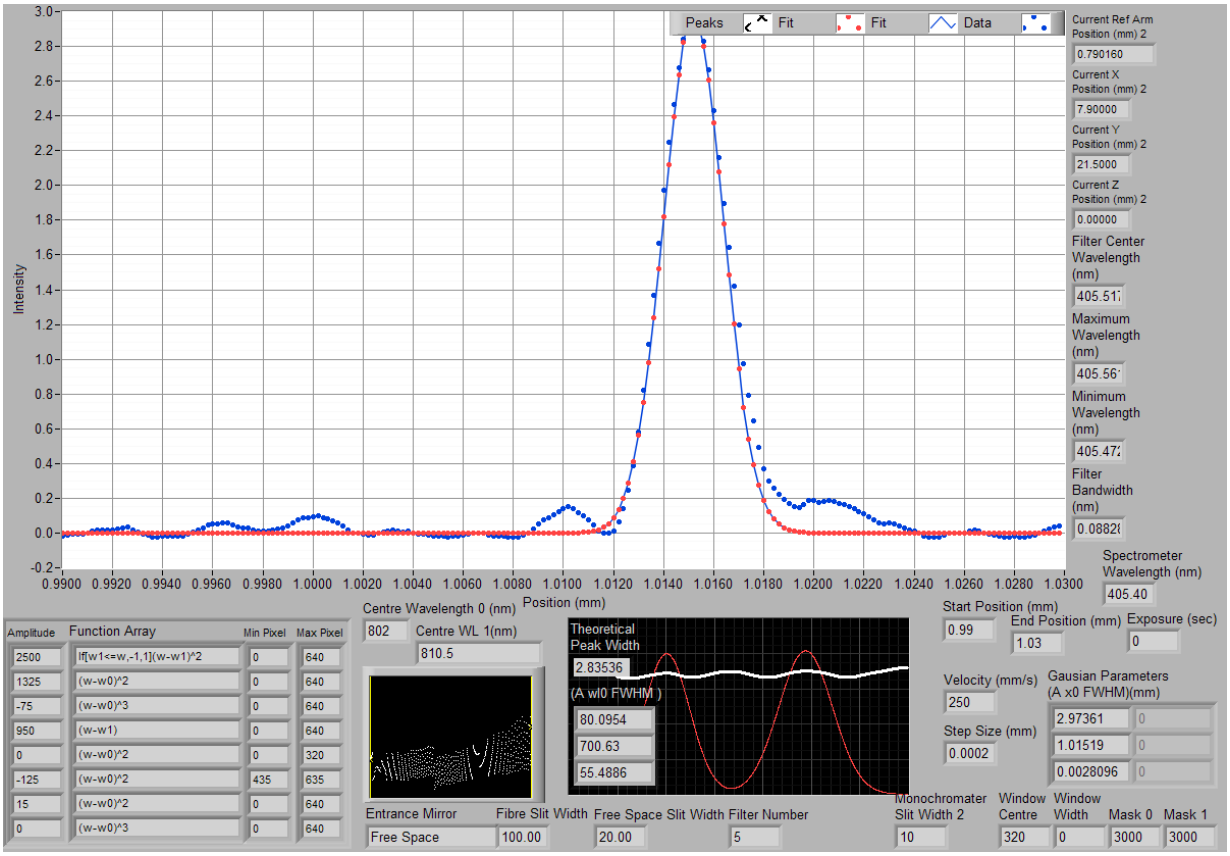

Figure 5.20: PMT CPI Trace with $2500fs^2$ IF Chirp without 10mm glass before the interferometer.

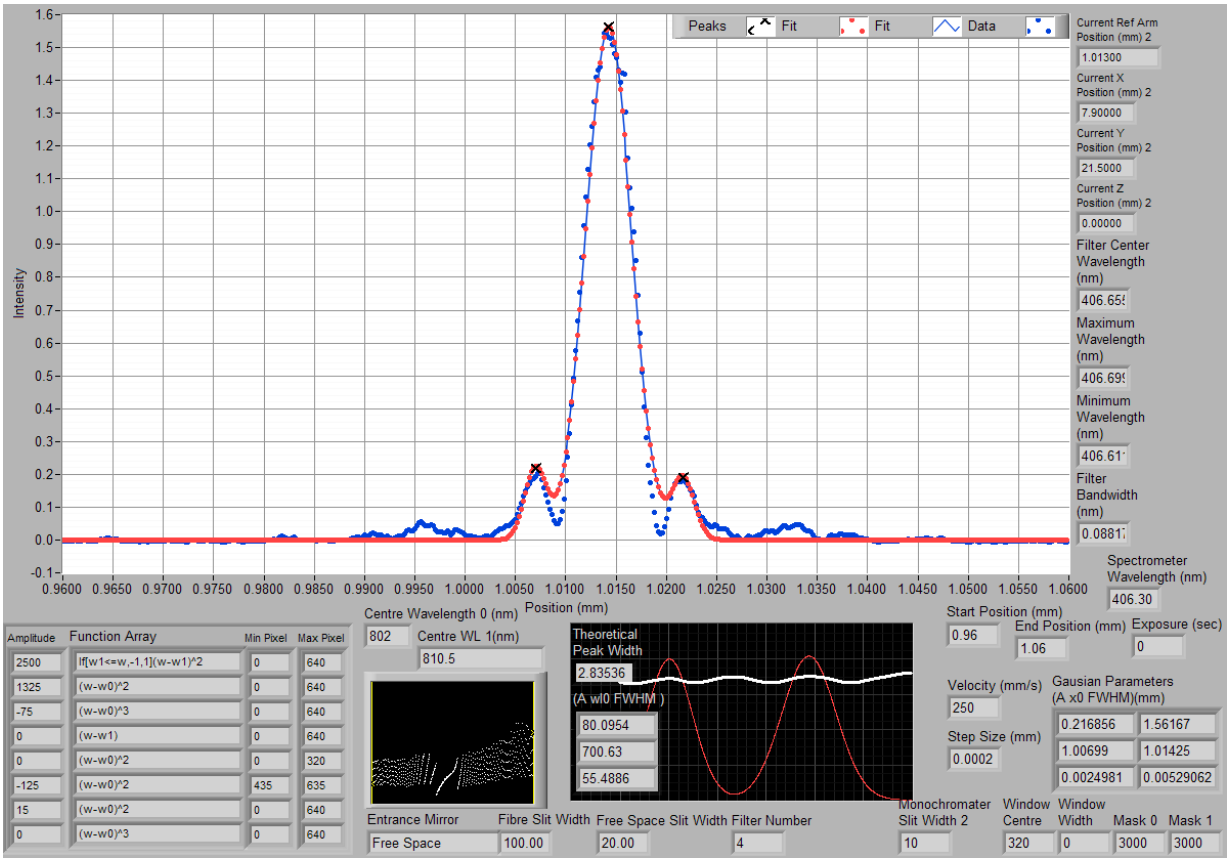

Figure 5.21: PMT CPI Trace with $2500fs^2$ IF Chirp with 10mm glass before the interferometer with no compensation.

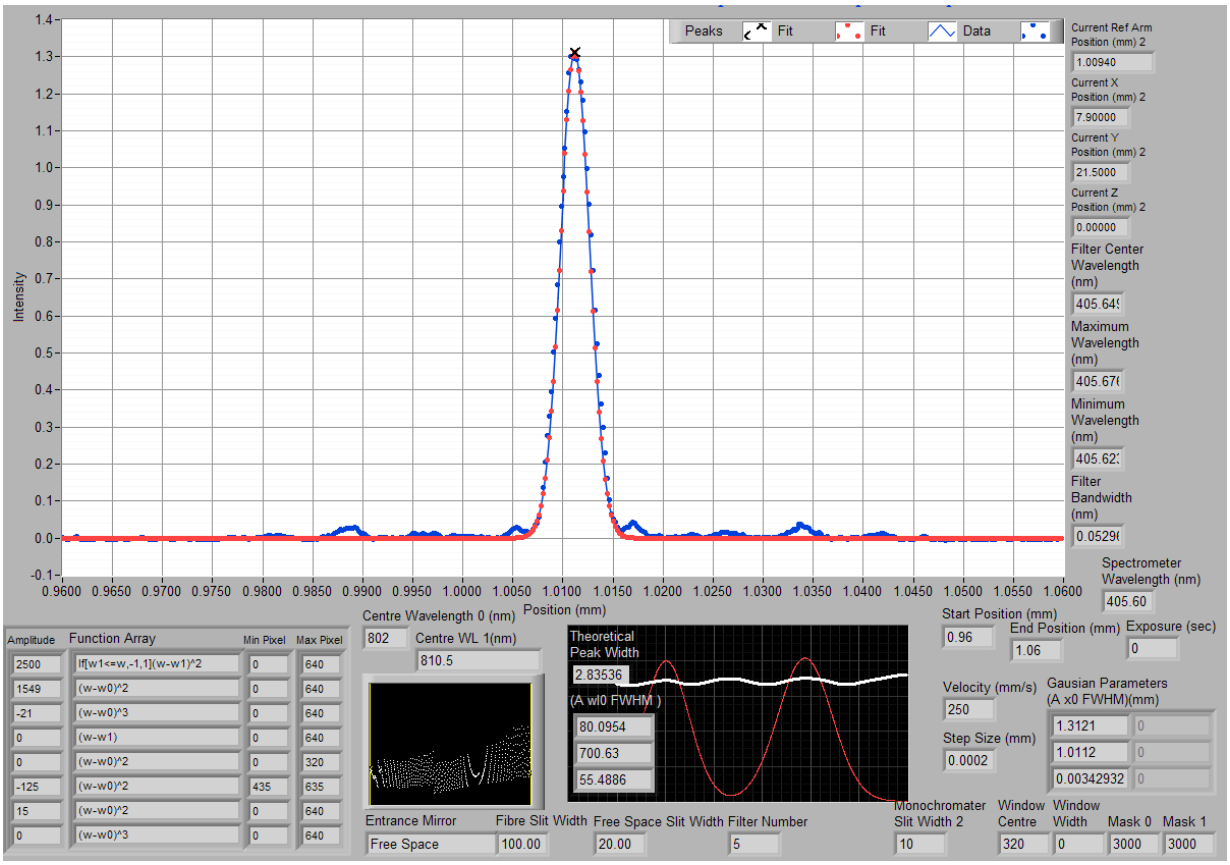

Figure 5.22: PMT CPI Trace with $2500fs^2$ IF Chirp with 10mm glass before the interferometer with $224fs^2$ and $54fs^3$ compensation.

Chapter 6

NL-CPI Bio-Imaging

6.1 Introduction

The demonstrated capabilities of non-linear CPI could be very useful in scanning biological samples. Removing the need to manually balance dispersion in each arm for each sample would make the setup process quicker and easier. It is therefore useful to attempt to scan a biological sample with the current experimental set-up.

6.1.1 Sample

Onion was chosen as the sample because it has been used previously in OCT experiments [1][3]. To gauge the size of the onion cells, a hair was placed on the surface of the onion and observed under a microscope. The diameter of the hair was measured previously to be around $50\mu m$. The cell size of the onion was compared to the hair and determined to be around $100\mu m \times 50\mu m$ to $800\mu m \times 100\mu m$.

6.1.2 Experimental Set-Up

The experiment uses the same set-up described in the previous chapter. The only additions were a sample holder in place of the mirror and some added software functions to handle recording the data for "scans" in the X or Y direction. The sample holder was designed to allow mounting a sample either in open air, or fully enclosed in water, or with only the back of the sample exposed to water. This was an attempt to keep the sample viable long enough to complete the scan. The sample holder is simply composed of a set of 1 inch lens tubes with glass windows at the ends held in with lock rings. Thorlabs SM1L05 lens tubes provide a great unadvertised feature that they are water tight when screwed together with a bit of strength. A small amount of vacuum grease on the threads can help prevent them

from seizing. Care should be taken when tightening the lock rings on the glass windows, to avoid cracking them.

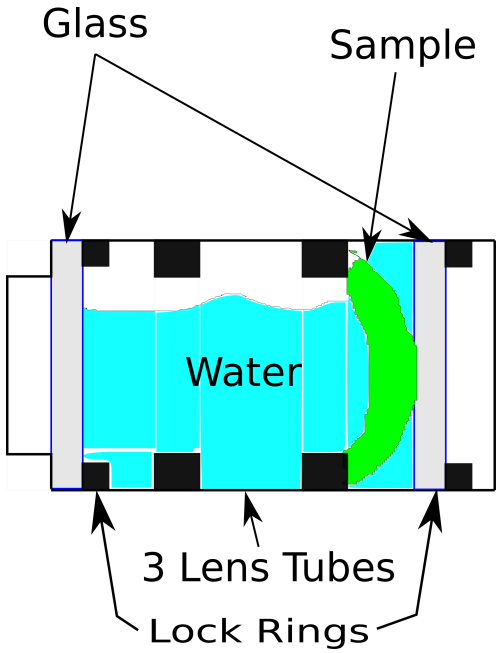

Figure 6.1: Diagram of Sample Holder
The sample holder is made by threading lens tubes together. A glass window behind the sample creates a water reservoir. A window in front of the sample can be used or the sample can be scanned without a cover.

The sample holder in Fig 6.1 is connected to a set of motorized linear stages providing X and Y positioning of the sample. A LabVIEW program takes a recipe file as input containing the X Y and Z or Reference arm positions, and the start, end and step length for the other of the sample or reference arm. The recipe also includes all other experimental parameters that can be set by the program such as filter wheel position, motors velocities, central wavelength, spectrometer gain etc.

When the program is run in spectrometer mode, each line of the recipe results in a separate 2-D spectscan file that must be later filtered and combined to form the image. In PMT mode the data is only 1-Dimensional for each position so it is automatically compiled into a single image on the fly.

6.2 Attempts At Imaging An Onion Using The Spectrometer As Sensor

The spectrometer was first used as the main sensor because of its better signal to noise ratio and absolute sensitivity. A piece of onion was mounted and scanned in the X directions. Unfortunately the method is extremely slow and only a few scans could be performed before the onion was damaged either by drying out or burning.

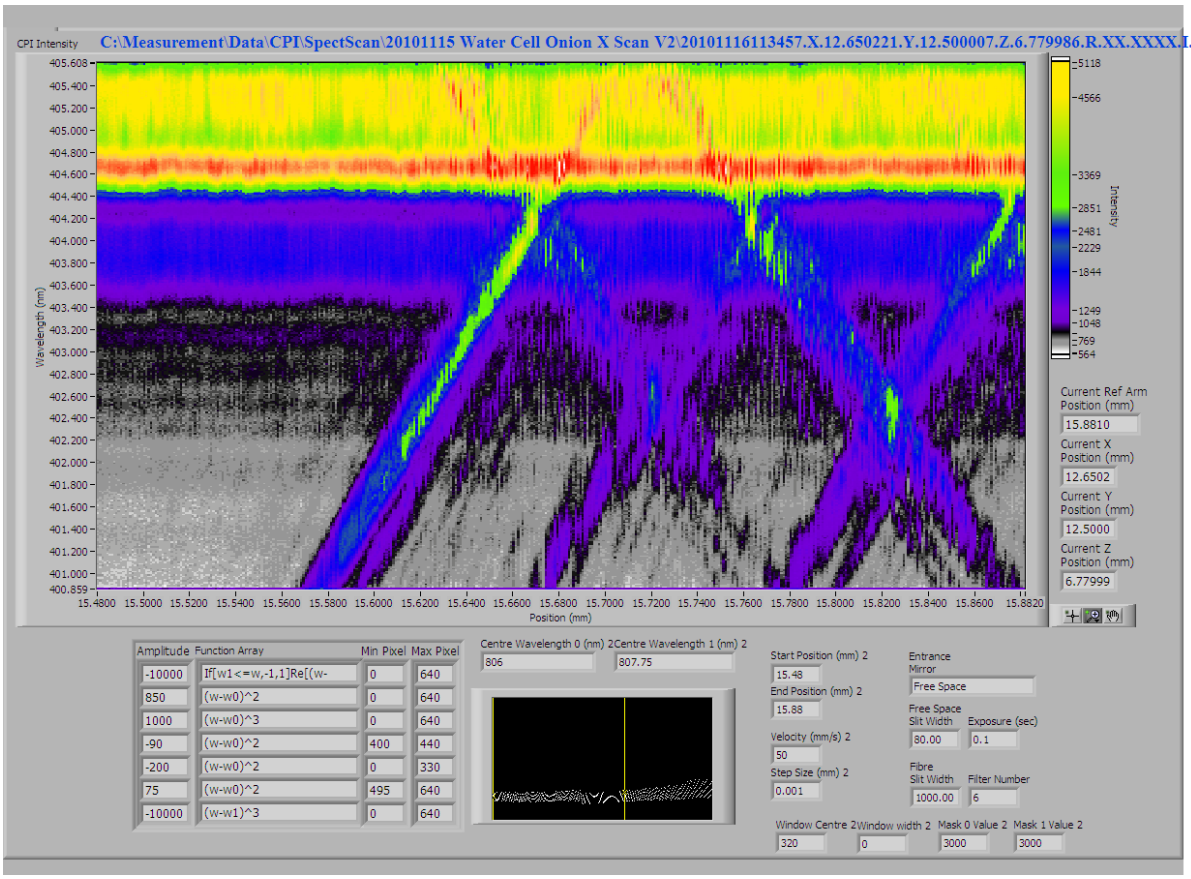

Figure 6.2: ExampleSpectScanData
The yellow band near the top of the image is background noise. The background noise causes interference when it overlaps in wavelength with the CPI signal.

The example image of a spectscan for one line of the recipe (one X and Y position) shows a broad stripe of background noise at the top (See Fig 6.2). If the CPI signal overlapped this noise interference resulted. Methods to decrease this noise included (with varying success) increasing the separation of the beams before the Primary Achromatic Doublet to increase the angle between the beams, as well as filtering out the IR.

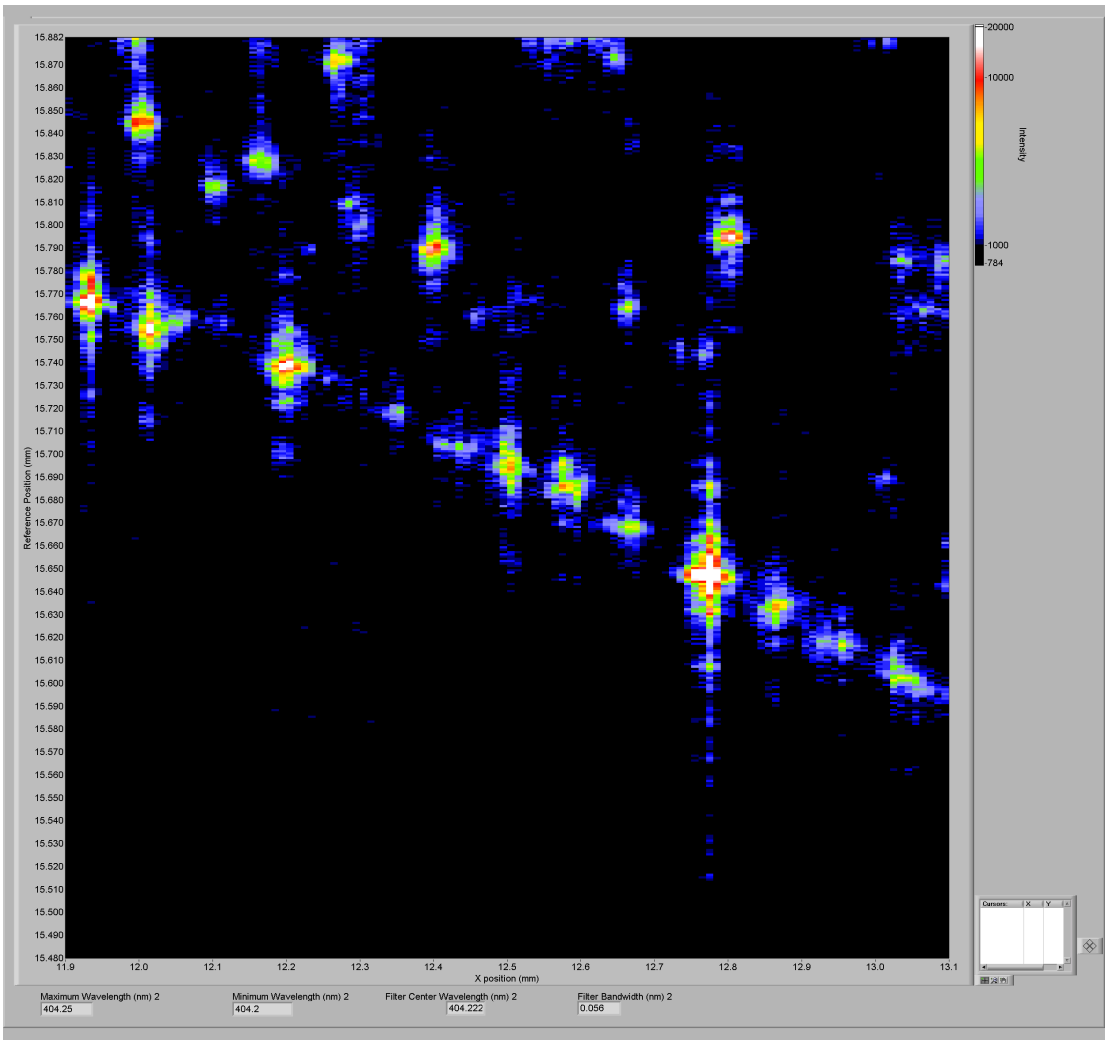

Figure 6.3: 2-D X-Scan Raw
Very little structure is present other than at the front surface of the onion.

A few of these spectscan images were examined and a suitable set of filter parameters were input into the LabVIEW program that compiled the 2-D images. The 2-D X-Scan Image in Fig 6.3 shows some structure, but other than the front surface of the onion, and possibly the back surfaces of the first row of cells, nothing that can be easily identified. It should be noted that the intensity is plotted with a linear scale, while most OCT images are plotted with logarithmic intensity scales. The data was processed using LabVIEW to take the natural log of the intensity, the result is shown in Fig 6.4. This shows only slightly more detail.

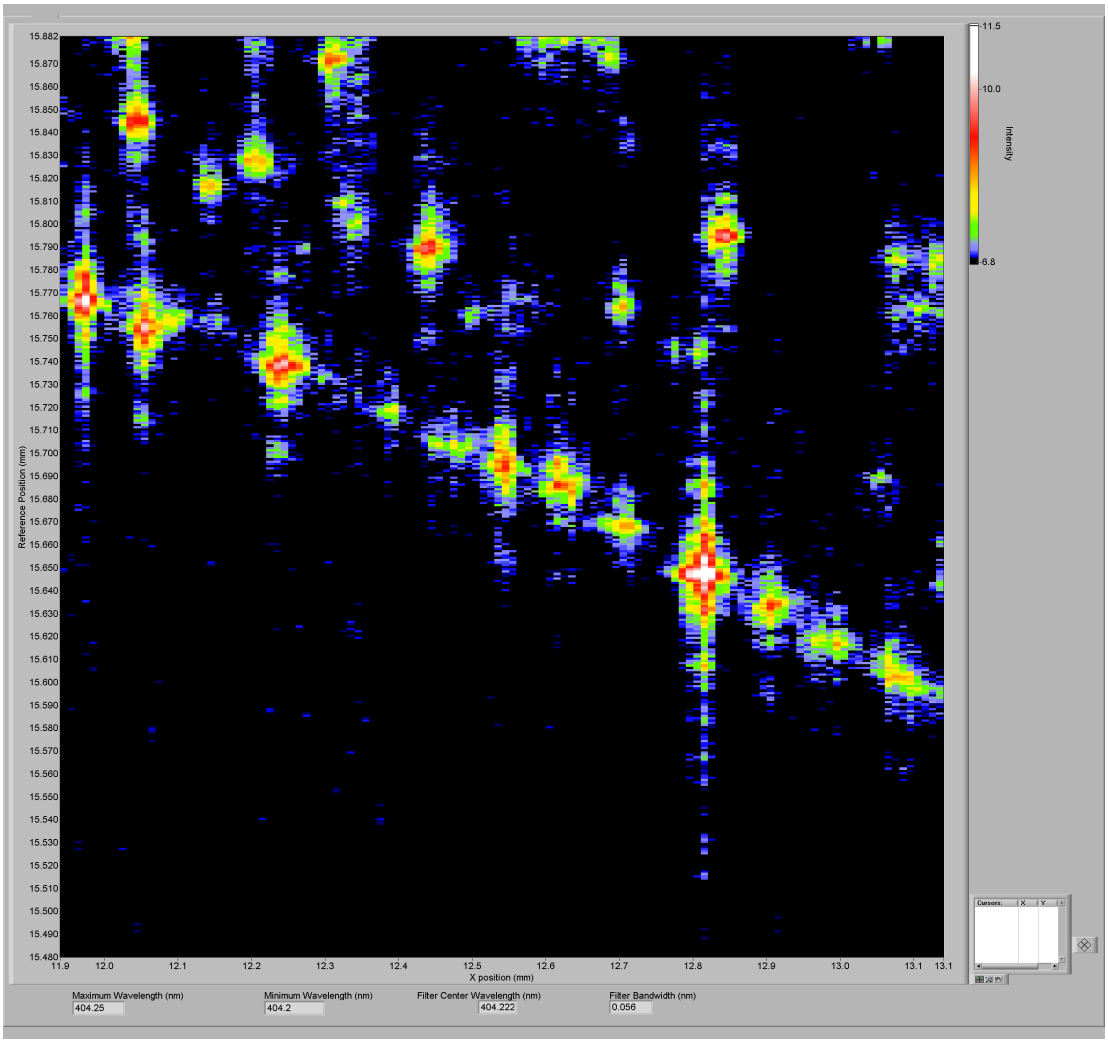

Figure 6.4: 2-D X-Scan Log

The Log of the intensity was also plotted. The lower diagonal line of peaks starting at reference 15.79mm and ending at reference 15.6mm is the front surface of the onion. A second line appears to start at reference 15.86mm. This could be the front and back of the first row of cells with a separation of 70μm. Compensating for index of refraction of water (1.33) this would be 52.5μm, within the gauged width of the onion cells.

6.3 Attempts At Imaging An Onion Using The PMT As Sensor

Attempts at scanning a separate biological sample were made using the PMT as a sensor. The sample was the membrane between layers of an onion, which is easily removed with

fingers or by tweezers.

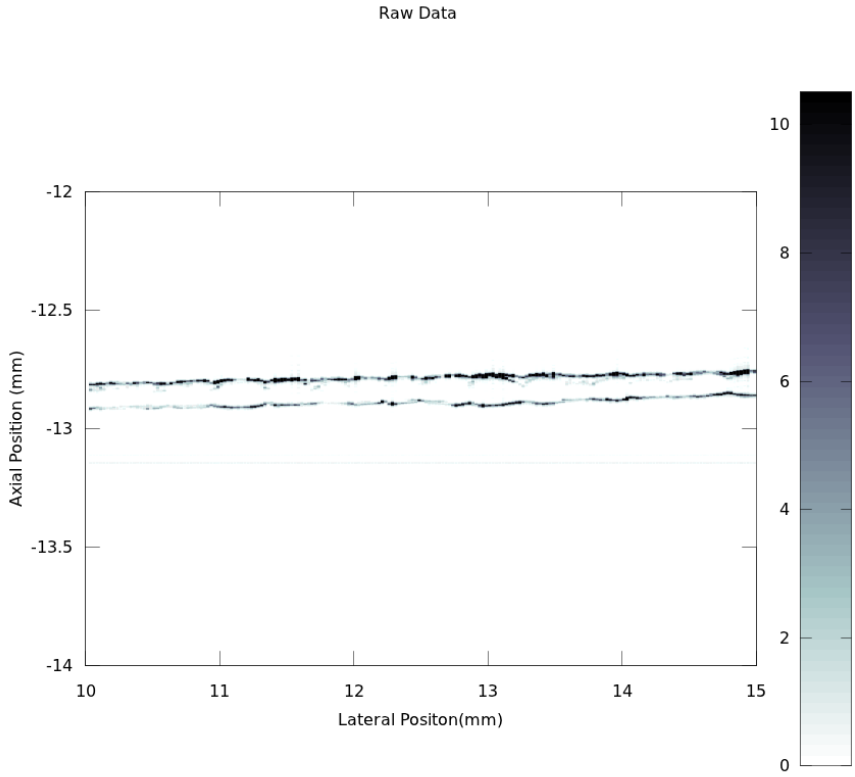

Figure 6.5: Example Raw PMT 2D Scan Data for Onion membrane using 8mm Ball Lens The Front and rear surfaces of the membrane are visible

6.4 Discussion

The images appear to show a biological structure, which is an important first step in competing with conventional OCT systems. The spectrometer scans were really just a way of testing the interferometer setup. The spectrometer is too slow to be used with the current methods. Because the PMT outputs an analogue signal it can be read much quicker than the spectrometer, so the overall scanning speed increases greatly (upto 200mm/s). The number of runs averaged over was not recorded, but even assuming 100x averaging, the overall maximum scanning speed is still at least 10,000 times faster than the previous biological Q-OCT experiment [16]. As well the biological Q-OCT experiment required the

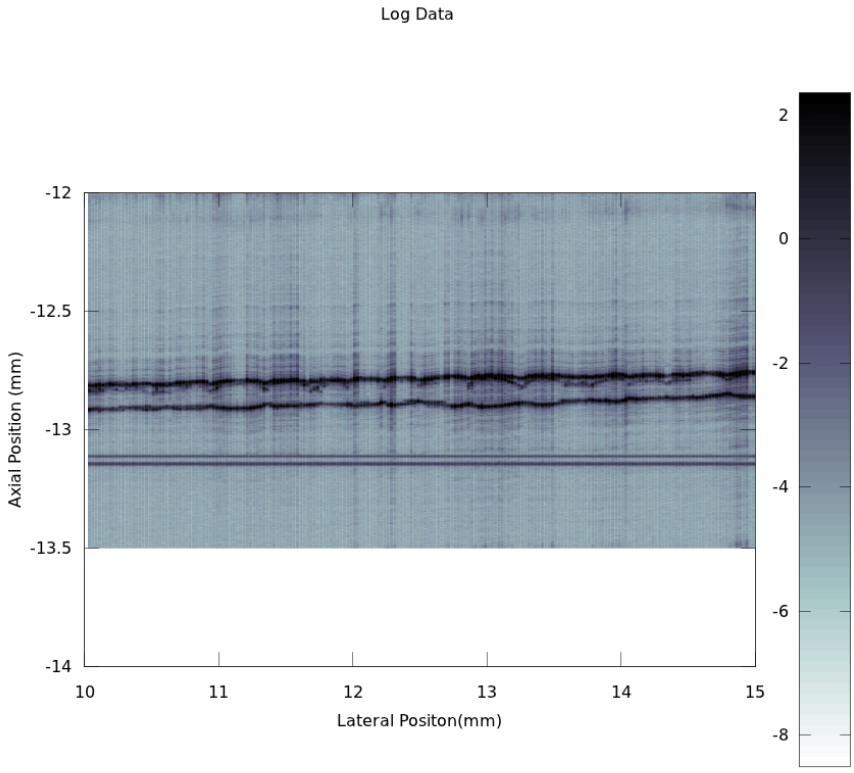

Figure 6.6: Example Log PMT 2D Scan Data for Onion membrane using 8mm Ball Lens Once the log of the intensity is taken, more detail is visible, but echoes due to sidel lobes become very visible.

samples to be coated in gold nano-particles to increase the signal[16]. Our experiments were performed on raw onion so just getting a signal is a great achievement.

Chapter 7

Conclusion

This thesis has demonstrated a new method of chirped pulse interferometry (CPI) using a programmable pulse shaper (PS). We detailed the construction of the PS, including the calibration of its core component, the spatial light modulator. We then demonstrated the PS's dispersion compensating capabilities by compressing an optical pulse to near its transform limit.

We used the PS to generate a non-linear (NL) chirp containing the frequency correlations required for CPI, in a single pulse. This was an improvement over the previous method, which required two pulses passing though separate devices. We demonstrated the dispersion cancellation capabilities of this method by imaging a mirror with and without a glass window in front of it, using both un-chirped and NL-chirped pulses. The broadening effect due to the glass was significantly reduced by adding the NL-chirp. We also demonstrated that NL-chirped pulses can be used to cancel broadening due to second order dispersion common to both arms of the interferometer. This is important because the interferometers used in OCT and Q-OCT are naturally immune to this type of dispersion.

We demonstrated the use of NL-CPI to image an untreated onion. This is an achievement because the demonstration of Q-OCT used an onion treated to increase its reflectivity, and our method was still at least 10,000 times faster.

Future directions for this work should focus on reducing the signal-to-noise ratio of the system until it is comparable to conventional OCT systems currently in use. Next we should focus on reducing the power sent to the sample without affecting system performance. Ideally the power level should be safe for use on human subjects. Investigating alternate detectors may provide a route to these goals. Optimizing the non-linear material choice would also be useful. A separate area to investigate would be methods of creating larger NL-chirps without negatively affecting system performance. A larger SLM with more pixels may help. An SLM that is capable of larger phase shifts would also help. Being able to produce larger chirps would permit larger amounts of dispersion to be cancelled. The goal would be to have a large enough chirp to cancel the even-order dispersion caused by a fibre

interferometer. This would greatly simplify the transition from current OCT systems to NL-CPI.

Appendices

Appendix A

The Gaussian Function

A.1 The Gaussian Function

It is sometimes said that the only things physicist really know how to do are solve the harmonic oscillator and the Gaussian function. Thus all physical phenomena must be one of those two. The Gaussian function is integral to the theory developed later in this thesis so it is worth reviewing some of it's properties.

The Gaussian function is simply an exponential dependant on the square of the independent variable. The more familiar version is the standard distribution used in statistics i.e. the Bell Curve:

$$e^{-\frac{(x-x_0)^2}{2\sigma^2}} \tag{A.1}$$

This is simply a Gaussian with standard variables to describe the width of the curve σ, and it's offset from center x_0.

Since the tails of the bell curve approach zero asymptotically some confusion can arise regarding what the actual width of the curve describes. In statistics the width σ refers to the root mean square (RMS) width of the function [27, pg. 31]. This measure is useful for describing the function because it simplifies the equation. RMS can be awkward to use when dealing with graphs because it is not immediately obvious by looking what the amplitude associated with the RMS width of a graph is.

A much easier value can be used when dealing with Gaussian functions because they are symmetric and have only one peak. Simply connecting the two points with half the maximum amplitude is an easy measure of the width of the the curve.

$$0.5 = e^{-\frac{x^2}{2\sigma^2}} \tag{A.2}$$

$$x_{0.5} = \sqrt{2Ln(2)}\sigma \tag{A.3}$$

$$FWHM = 2x_{0.5} = 2\sqrt{2Ln(2)}\sigma \tag{A.4}$$

This is called the full width at half maximum (FWHM)[27, pg. 31]. Interestingly the FWHM and RMS are independent of the amplitude, so changing the amplitude of the Gaussian will not change it's FWHM or RMS. This means that we can always compare signals with Gaussian profiles regardless of the strength of the signal.

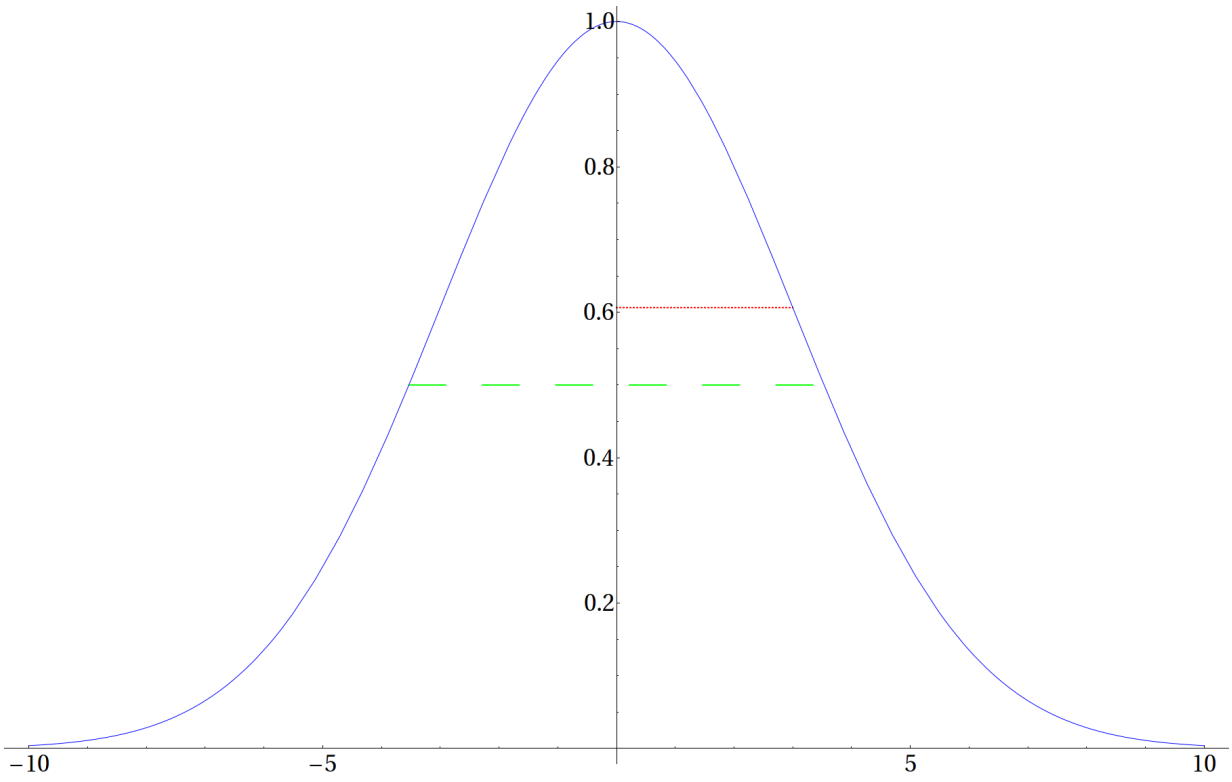

Figure A.1: Graph comparing RMS width and FWHM width
The RMS width (Red Dotted Line) occurs at approximately 0.6065 times the maximum amplitude which is not intuitive to use. The FWHM (Green Dashed Line) is much easier and can be fairly accurately measured by sight alone.

An incredibly handy feature of Gaussian functions is that their integral is analytic and itself a Gaussian[2].

$$\int ae^{-\frac{(x-b)^2}{2\sigma_x^2}} = a\sigma\sqrt{2\pi} \tag{A.5}$$

The Fourier transform of a Gaussian is again a Gaussian [23, pg 1124]

$$\mathcal{F}\{k\} = \int e^{-\frac{(x)^2}{2\sigma_x^2}} e^{-2\pi ikx} = \sqrt{2\pi}\sigma_x e^{-2\sigma_x^2\pi^2k^2} \tag{A.6}$$

where the RMS in units of k becomes:

$$\sigma_k = \frac{1}{2\pi\sigma_x} \tag{A.7}$$

The convolution of two Gaussian's is also a Gaussian, which can be shown using the convolution theorem[19, pg 492] and Eq A.6:

$$\mathcal{F}\{f * g\} = \mathcal{F}\{f\} \cdot \mathcal{F}\{g\} \tag{A.8}$$

Beginning with:

$$\int_\infty^\infty e^{-\frac{(x-\tau)^2}{2\sigma_1^2}} e^{-\frac{(x)^2}{2\sigma_2^2}} d\tau = \mathcal{F}^{-1}(\mathcal{F}\{e^{-\frac{(x)^2}{2\sigma_1^2}}\}\mathcal{F}\{e^{-\frac{(x)^2}{2\sigma_2^2}}\}) \tag{A.9}$$

and neglecting the amplitudes:

$$\mathcal{F}^{-1}(e^{-2\pi^2(\sigma_1^2+\sigma_2^2)(x)^2}) = e^{-\frac{(x)^2}{2(\sigma_1^2+\sigma_2^2)}} \tag{A.10}$$

we see that the new width is simply the Euclidean norm of the widths of the two convoluted functions.

$$\sigma = \sqrt{\sigma_1^2 + \sigma_2^2} \tag{A.11}$$

This explains why the auto-correlation of two Gaussian pulses is $\sqrt{2}$ larger than the pulse duration.

These properties make the Gaussian function especially appealing in developing the theory of chirped pulse interferometry, the challenge then becomes making the experimental implementation of the theory conform to this.

Appendix B

Diffraction Gratings

B.1 Diffraction Gratings

An essential part of the pulse shaping system is the ability to apply frequency dependant phase modulation. In order to accomplish this the different frequencies must first be separated from each other. This is can be accomplished through refraction or diffraction. Refraction typically uses glass prisms to create frequency dependant angular displacement of the light passing though them. However this method is not ideal for a pulse shaper because the glass would introduce even more dispersion, which we are building the pulse shaper to compensate away.

The second method, diffraction, involves the interaction of light with finely spaced grooves on an optical surface. This is known as a grating. The light may be either transmitted through the grating or reflected from it. The key element of the diffraction grating is the distance between the grooves [9, pg. 478].

$$d(sin\theta_m + sin\theta_i) = m\lambda \tag{B.1}$$

Where θ_i is the angle of incidence measured from the normal of the grating plane (which may not be the same as the reflecting surface of an individual groove). The integer m is know as the order of refraction and θ_M is the angle for that order of the diffracted beam relative to the normal of the grating plane. m can be positive or negative, and when m = 0 the reflection angle is equal to the angle of incidence, and the grating acts like a regular mirror. Gratings can be configured to concentrate a large portion of the signal power into a single order. This is know as blazing[9, pg. 479].

Under certain conditions the light will be refracted directly back along the incoming beam path, so $\theta_i = \theta_m$. This is known as the Littrow condition[9, pg. 480]. The gratings used for the experiments in this thesis were made by Spectrogon (Model#715.701.120 PC 1200 30x30x6 NIR) 1200lines/mm reflective grating. The gratings are blazed to provide

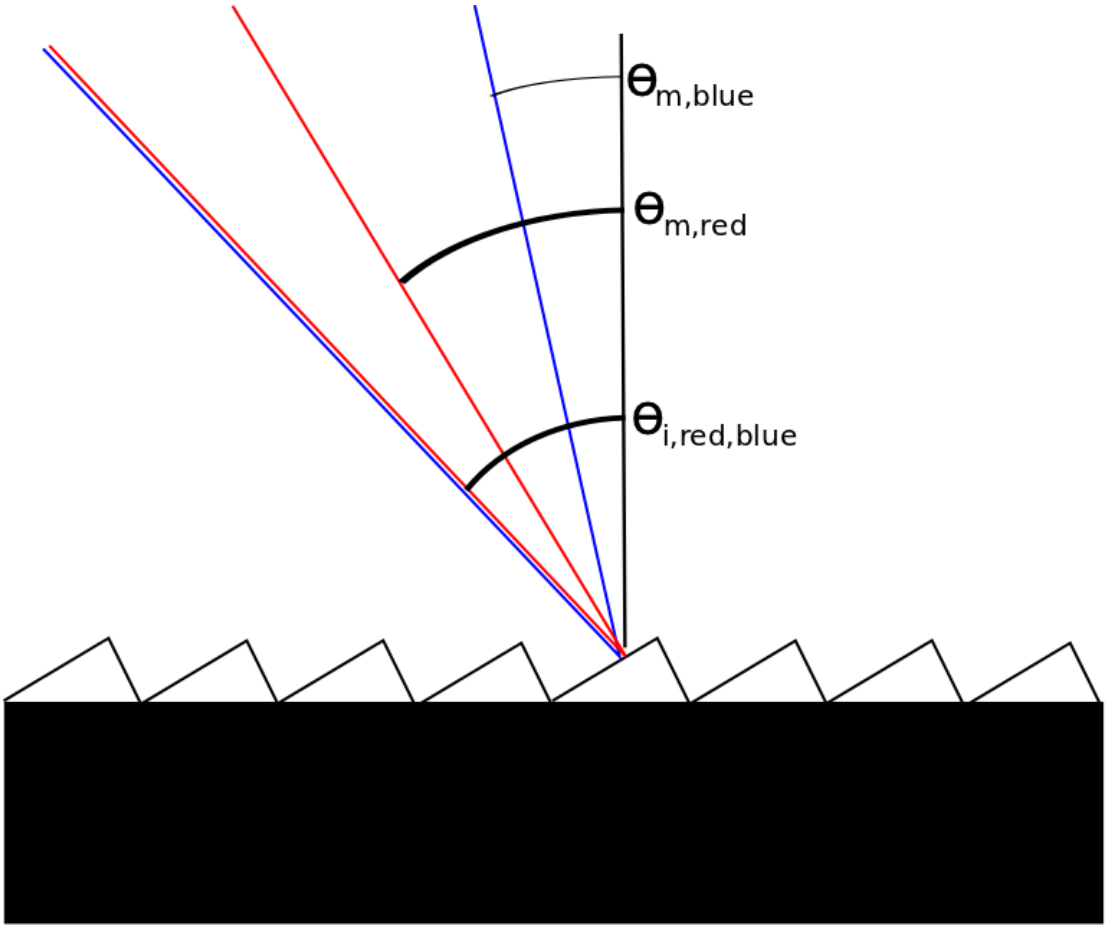

Figure B.1: Diffraction Of a Multicoloured Beam.
The red end of the spectrum has a smaller angle of deflection from Littrow, and so will be closer to the maximum efficiency condition.

maximum efficiency at the Littrow condition for a specific wavelength (800nm). The Littrow angle was 28 deg.On the other hand, the gratings become less efficient away from the blaze wavelength and or the Littrow angle.

References

[1] Ayman F. Abouraddy, Magued B. Nasr, Bahaa E. A. Saleh, Alexander V. Sergienko, and Malvin C. Teich. Quantum-optical coherence tomography with dispersion cancellation. *Phys. Rev. A*, 65(5):053817, May 2002. iii, 1, 15, 93

[2] Asmar. *Partial differential equations with Fourier series and boundary value problems*. Pearson Prentice Hall, Upper Saddle River, N. j, 2005. 104

[3] B Bouma, G J Tearney, S a Boppart, M R Hee, M E Brezinski, and J G Fujimoto. High-resolution optical coherence tomographic imaging using a mode-locked Ti:Al(2)O(3) laser source. *Optics letters*, 20(13):1486–8, July 1995. 14, 93

[4] Robert Boyd. *Nonlinear optics*. Academic Press, Burlington, MA, 2008. 7, 8, 10

[5] Mark Brezinski. *Optical Coherence Tomography*. Academic Press, Boston, 2006. 12, 13, 15

[6] J Diels and W Rudolph. *Ultrashort laser pulse phenomena fundamentals, techniques, and applications on a femtosecond time scale*. Academic Press, Burlington, MA, 2006. 4, 6, 50

[7] A F Fercher, W Drexler, C K Hitzenberger, and T Lasser. Optical coherence tomography - principles and applications. *Reports on Progress in Physics*, 66(2):239–303, 2003. 1

[8] John Garrison. *Quantum Optics*. Oxford University Press, Oxford Oxfordshire, 2008. 17

[9] Eugene Hecht. *Optics*. Addison-Wesley, Reading, Mass, 2002. 10, 106

[10] C K Hong, Z Y Ou, and L Mandel. Measurement of subpicosecond time intervals between two photons by interference. *Physical Review Letters*, 59(18):2044–2046, 1987. 16, 17, 18

[11] R Kaltenbaek, J Lavoie, D N Biggerstaff, and K J Resch. Quantum-inspired interferometry with chirped laser pulses. *Nature Physics*, 4(11):864–868, Oct 2008. 2, 20, 22, 65

[12] J. Lavoie. Chirped-Pulse Interferometry: Classical dispersion cancellation and analogues of two-photon quantum interference. Master's thesis, Univerity of Waterloo, 2009. 12, 15, 17, 20

[13] J. Lavoie, R. Kaltenbaek, and K. J. Resch. Quantum-optical coherence tomography with classical light. *Optics Express*, 17(5):3818–3825, Feb 2009. iii, 2, 15, 55, 76

[14] Peter Milonni. *Laser physics*. John Wiley and Sons, Hoboken, N.J, 2010. 6

[15] multiple. Wikipedia - discrete fourier transform. `http://en.wikipedia.org/wiki/Discrete_Fourier_transform`, July 28 2011. 27

[16] Magued B. Nasr, Darryl P. Goode, Nam Nguyen, Guoxin Rong, Linglu Yang, Bjrn M. Reinhard, Bahaa E.A. Saleh, and Malvin C. Teich. Quantum optical coherence tomography of a biological sample. *Optics Communications*, 282(6):1154 – 1159, 2009. iii, 2, 15, 19, 20, 98, 99

[17] Z Y Ou, C K Hong, and L Mandel. Relation between input and output states for a beam splitter. *Optics Communications*, 63(2):118–122, 1987. 16

[18] R Paschotta. Encylopedia of laser physics - chromatic dispersion. `http://www.rp-photonics.com/chromatic_dispersion.html`, July 27 2011. 6

[19] William Press. *Numerical Recipes in Fortran*. Cambridge University Press, Cambridge, 1992. 26, 27, 105

[20] F Raoult, a C Boscheron, D Husson, C Sauteret, a Modena, V Malka, F Dorchies, and a Migus. Efficient generation of narrow-bandwidth picosecond pulses by frequency doubling of femtosecond chirped pulses. *Optics letters*, 23(14):1117–9, July 1998. 21

[21] K. J. Resch, R. Kaltenbaek, J. Lavoie, and D. N. Biggerstaff. Chirped-pulse interferometry with finite frequency correlations. *Proceedings of SPIE*, 7465(May 2010):74650N–74650N–8, 2009. 15, 18, 19, 20, 21, 24, 26

[22] K J Resch, P Puvanathasan, J S Lundeen, M W Mitchell, and K Bizheva. Classical dispersion-cancellation interferometry. volume 15, pages 8797–8804. OSA, 2007. 1, 80

[23] Saleh. *Fundamentals of photonics*. Wiley-Interscience, Hoboken, N.J, 2007. 1, 7, 9, 13, 104

[24] A Siegman. *Lasers*. University Science Books, Mill Valley, Calif, 1986. 5, 15

[25] Julius Smith. *Mathematics of the discrete Fourier transform (DFT) : with audio applicaitons*. BookSurge Publishing (http//www.booksurge.com, Seattle. WA, 2007. 27

[26] Aephraim M Steinberg, Paul G Kwiat, and Raymond Y Chiao. Dispersion cancellation and high-resolution time measurements in a fourth-order optical interferometer. *Physical Review A*, 45(9):6659–6665, 1992. 17, 18, 19

[27] R Trebino. *Frequency-resolved optical gating : the measurement of ultrashort laser pulses*. Kluwer Academic, Boston, 2000. 4, 5, 6, 9, 10, 11, 20, 50, 103, 104

[28] H. Wang, Z. Zheng, D.E. Leaird, a.M. Weiner, T.a. Dorschner, J.J. Fijol, L.J. Friedman, H.Q. Nguyen, and L.a. Palmaccio. 20-Fs Pulse Shaping With a 512-Element Phase-Only Liquid Crystal Modulator. *IEEE Journal of Selected Topics in Quantum Electronics*, 7(4):718–727, 2001. 29, 45